ANALYSIS AND FEEDBACK CONTROL OF MAGNETIC BEARINGS

with reference to

FLYWHEEL ENERGY STORAGE

by

GORDON LESLIE BREDENKAMP

THESIS

submitted in fulfilment of the requirements for the degree

of

DOCTOR of PHILOSOPHY

to the

UNIVERSITY OF CAPE TOWN

FEBRUARY 1984

AKNOWLEDGEMENTS: I Hereby wish to express my sincerest gratitude towards

my supervisor, **Professor NC de V Enslin**, for his interest and encouragement which I received during this investigation,

my wife, **Sofia**, for her support and assistance in typing the text and preparing the drawings,

The Rand Afrikaans University in whose laboratories the experimental work was done,

Cooperative Scientific Programs (CSP) of the Council for Scientific and Industrial Researh (CSIR) for providing part of the funding in the form of a research grant for initiating this project,

Mr Jan Harm Pretorius who completed a masters degree, under my supervision, on the same topic, whose assistance with the experimental work and in verifying the mathematical derivations was invaluable,

Mrs Ina Liebenberg for reading through the text and correcting many errors and finally to

numerous undergraduate students who also made many positive contributions to this investigation.

Author.

ABSTRACT: In high speed applications magnetic bearings offer many potential advantages over mechanical bearings. The type of magnetic bearing most suitable for *energy storage flywheels* is selected and analysed for the purpose of designing feedback control loops. A nonlinear as well as a small signal linear model of the *"current driven"* magnetic bearing with *unlaminated magnetic components* is derived. Subsequently *describing functions*, characterising the small- as well as large signal behaviour of the same bearing in the *"voltage driven"* mode, are obtained. It is shown that workable results are obtained for most practical situations by using linear systems theory, although the magnetic bearing is a nonlinear device. The describing function model enables the designer to identify the mechanisms leading to limit cycles under adverse operating conditions. Feedback control loops designed around the small signal characteristics produce practical results in the case of the "voltage driven" mode which are superior to that of the "current driven" case. An essential refinement, where *energy losses* and vibrations arising from rotor imbalance are *eliminated*, is described. A *discrete time filtering technique* is used. Two experimental models where built and fully tested in order to verify the above theoretical approaches.

SAMEVATTING: Vir hoëspoed toespassings besit die magnetiese laer heelwat eienskappe wat dit potensiëel meer aantreklik as die meganiese laer maak. Die mees geskikte magnetiese laer, vir toepassing in *vliegwiele vir energiestoring*, word geselekteer en met die oog op terugvoerbeheer geanaliseer. 'n Lineêre kleinseinmodel word van die nie-lineêre model van 'n *stroomgevoerde* magnetiese laer, met *soliede staal* (dws ongelamineerde) *poolstukke*, afgelei. Hierop word die *beskrywende funksies* wat die gedrag van dieselfde laer in die *spanningsgevoerde* modus voorspel, verkry. Daar word aangetoon dat lineêre analise en sintese van die stelsel, vir die meerderheid van praktiese situasies, geldige resultate lewer. Die beskrywendefunksie model stel nogtans die ontwerper in staat om die meganismes, wat aanleiding gee tot die ontstaan van limietsiklusse onder swak bedryfstoestande, te kan identifiseer. Beheerlusse waarvan die ontwerp gebaseer word op die spanningsgevoerde kleinseinmodel lewer resultate wat beter is as dié wat met die stroomgevoerde model verkry word. 'n Verbetering, noodsaaklik vir langtermyn energiestoring, waarby *drywingsverliese en vibrasies*, wat onstaan as gevolg van wanbalans van die rotor, *uitgeskakel word*, word beskryf. 'n *Diskrete-tyd filtertegniek* word gebruik. Twee eksperimentele laers is gebou en volledig getoets teneinde die bogenoemde teoretiese beskouinge te bevestig.

C O N T E N T S

page

LIST of ILLUSTRATIONS

page

CHAPTER 1

I N T R O D U C T I O N

1.1 Background

Since the oil crisis of November, 1973, a great deal of work has been done on alternative energy sources and it has become apparent that the potential of many of these sources could be exploited economically only if suitable energy storage systems are available to serve as "load levelling" devices to the source. This is due to the disparity in the energy supply and demand time profiles that is usually encountered in any practical situation. Arguments supporting this statement are dealt with more fully in reference [1]. (throughout this text numbers appearing in squared brackets will refer to literature listed at the end of this text).

Initially the technique of storing energy in so-called "superflywheels" seemed to hold greater promise than the more conventional batteries. This was mainly due to the higher expected energy storage capacity per unit mass of the flywheel, usually refered to as specific energy [2], [3], [4], [5], [6] and [7]. Practical results achieved with superflywheels [8] indicate an improvement in specific energy relative to lead acid batteries by a factor of 2 to 5 which makes it doubtful whether, despite several major advantages, they will find widespread preference to batteries, due to the higher expected cost and more sophisticated technology involved.

The three major problem areas that could be identified with superflywheel systems were:
(a) The construction of the flywheel rotor
(b) The suspension of the rotor (bearings) and
(c) The drive motor/generator required for exchanging energy between the flywheel and the energy system to which it is coupled.

In view of the fact that extensive development work on superflywheel rotors was in progress, mainly in the United States of America in the past decade, the author became involved in research related to the suspension and drive motor/generator for such flywheels. Initially a high speed (40000 r/min) 1kW reluctance machine with electronic commutation was developed for the purpose of testing rotors at high speed in a vacuum tank. An outflow of this was an investigation into the profiling of reluctance machine rotors, in an attempt to make them more suitable for square wave (as opposed to sinusoidal wave) operation. This leads to greater compatibility with electronic commutators. At the same time a higher specific power is achieved. Under supervision of the author, the abovementioned investigation into reluctance machine rotors is in its final stages of completion at the Rand Afrikaans University [9].

This thesis will concentrate mainly on the feedback control of a 5-axis magnetic bearing system of the type suitable for superflywheels.

All flywheels known to date suffer from the fundamental restriction that the maximum specific energy is determined by the ratio of material strength (σ_{max}) to density (ρ) [2]. This is mainly due to the fact that the strength of the material is utilised to confine the "energy storage mass" of the flywheel to a circular orbit. This problem will be returned to later on in the next section.

1.2 Why Investigate Magnetic Bearings?

Although conventional high speed mechanical bearings are available which are capable of supporting the mass of the flywheel at the required rotational velocities (eg. 200kg at 25 000 r/min), they seem to be mostly suited to flywheels which are primarily intended for load levelling in applications such as hybrid internal combustion - flywheel vehicles (Frank, 1977, [10]) and hybrid battery - flywheel vehicles (Towgood & Satchwell, 1977, [11], Cornell et al, 1979, [12]).

The mechanical losses in such bearings are generally so high at these speeds that the storage efficiency of the system (ie the ratio of stored energy at the end of a charging cycle to the available energy at some later stage) is severely degraded for storage times in eccess of say 30 minutes (Sabnis, Dendy and Schmitt, 1975, [14]). More recently, however, two different configurations of mechanical bearings have been tested at The Johns Hopkins Applied Physics Laboratory (APL) where the high speed drag losses measured under laboratory conditions were so low as to be comparable to those of magnetic bearings (Rabenhorst, Small and Wilkinson, 1980, [15]). The techniques used here were very novel and at this stage it is difficult to judge their practical usefulness.

In applications where storage times are relatively short, say at most a few minutes, relatively high bearing losses can be tolerated since these losses will then only represent a small fraction of the total energy exchange.

The author conducted an experiment where a 10kg disc was suspended on two 25mm (inner diameter) deepgroove ball bearings and spun in a vacuum chamber at a pressure of 144Pa. This rotor was carefully balanced dynamically and rundown time constants of typically 3 hours were measured.

In this type of application mechanical bearings require sophisticated lubrication systems and special mounting techniques have to be resorted to in order to accommodate the imbalance of the flywheel which is constantly shifting with changing speed. This problem may be overcome by providing resilient mountings for the stator of the bearing. This technique is applied in certain turbomolecular pumps (Usselmann, 1977, [16]), and was also applied by the author for the testing of high speed turbine rotors at 35000 r/min.. See fig. 1.1.

Alternately the flywheel may be suspended on a flexible quill as shown in fig 1.2. This method would normally only be applicable to stationary flywheel systems and has many

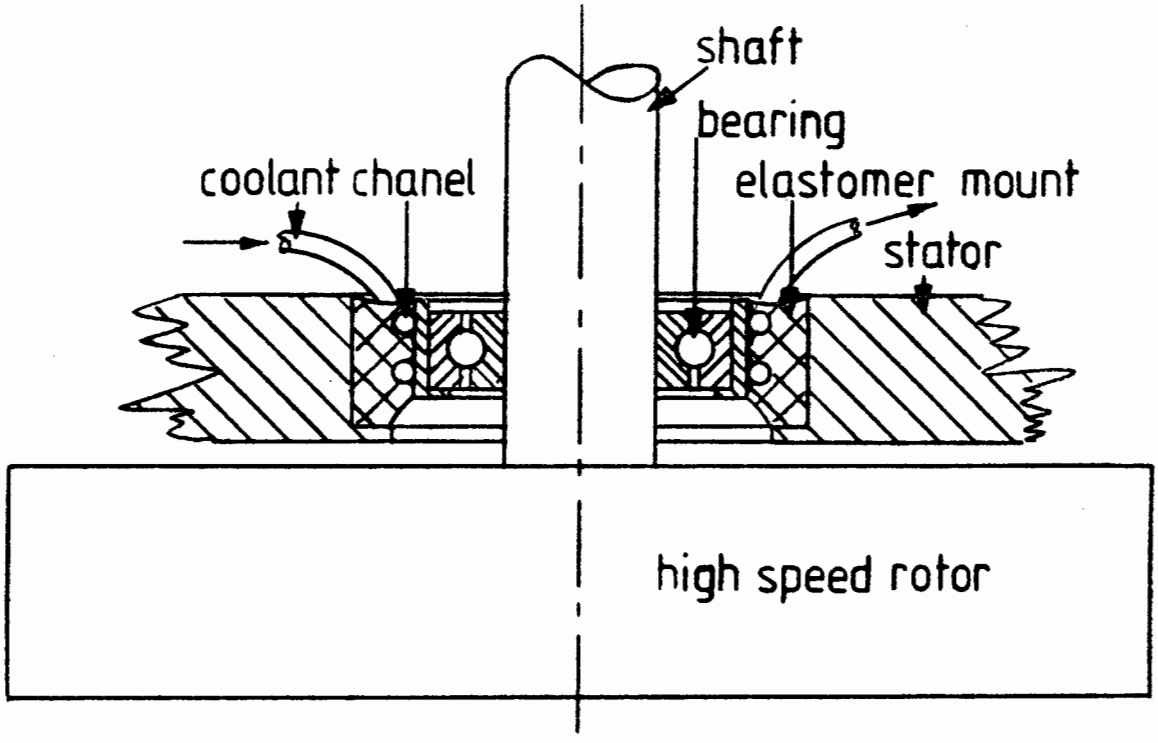

FIG.1.1 RESILIENTLY MOUNTED BALL BEARING

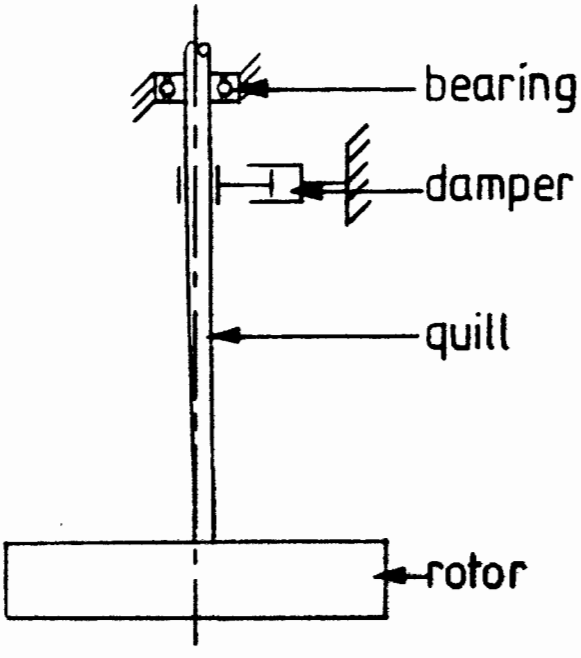

FIG.1.2 FLEXIBLE QUILL MOUNTING OF HIGH SPEED ROTOR

unique stability problems which have been analysed by Younger [17]. Special mechanical dampers are required for the stabilisation of such a system.

The fundamental reason why mechanical bearings are problematic is because of their tendency to display a high degree of stiffness at the rotational frequencies of the flywheel. As a consequence the slightest degree of imbalance cannot be tolerated. A technique will be described later in this text (chapter 6) whereby the stiffness of a magnetic bearing could be reduced to zero at the rotational frequency, thus eliminating effectively all the losses associated with imbalance.

Although an unlimited life may be expected from a magnetic bearing due to the absence of mechanical friction, it must be stated in favour of mechanical bearings that a long life may also be expected in the relatively clean vacuum environment of the flywheel. Experience with turbomolecular pumps has indicated that mechanical bearings may be operated at high speed without interruption for 40 000 hours and longer [16].

The idea of suspending a rotor without contact between magnetic poles is very attractive since problems encountered with mechanical and gas bearings such as lubrication, fine tolerance specifications and limited lifetime may be totally eliminated. With respect to (a) energy losses due to drag, resistance and magnetic losses, (b) reliability and (c) stiffness presented to high frequency vibrations, considerable improvements may be obtained relative to mechanical bearings provided the correct configuration is chosen for the application in mind. Low frequency stiffness and steady state errors can also be tailored to suit the application within very wide limits. Magnetic bearings could in fact be designed to be stiffer than mechanical bearings. With integral feedback infinite low frequency stiffness may be achieved and under certain conditions such bearings could even be designed to possess a negative stiffness [14].

During this investigation into magnetic bearings and after much reflection on the restriction on superflywheels mentioned at the end of section 1.1 it became apparent that should magnetic forces, instead of material stresses, be employed to confine an energy storage mass to its required orbit, much greater specific energies may be achieved in large installations (> 1 MWh) than with superflywheels. Such a magnetically restrained kinetic energy system (MARKES), as described in references [1] and [18], relies totally on magnetic suspension and a thorough understanding of the latter is therefore essential. It is estimated that such a system, with an energy storage capacity of 2000 MWh, would cost between one sixth and one third of the price of a comparable pumped storage scheme.

Thus, in spite the pessimism expressed earlier regarding superflywheels, an investigation into magnetic bearings is nevertheless relevant to the field of inertial energy storage and in addition to this many other applications of magnetic bearings are envisaged particularly where high speeds are involved and where lubricants are often incompatible with the operating environment such as gyroscopes, centrifuges, turbo molecular pumps, compressors for corrosive fluids etc.

It is well known that magnetic bearings have already been employed to a certain degree in most of the abovementioned applications (see, for instance, references [19]&[20]). A great deal of work has been published to date on linear motion magnetic bearings which are being investigated for the levitation and suspension of trains by workers in the field such as Laithwaite [21], Jayawant [22], Nasar and Boldea [23] and many others (see references). Many of the theoretical developments in these publications are obviously also applicable to rotary magnetic bearings. Specific in depth literature on the latter, however, does not appear to be available, probably since this is a hitherto largely unexploited technology and the relevant information is being withheld due to military as well as commercial considerations. Much of the work presented here could thus, in all probability, be a repetition of work

done elsewhere which is not generally accessible and thus also unknown.

1.3 The Objectives of this Investigation

The objective of this investigation is primarily to gain a deeper insight into the dynamic behaviour of magnetic bearings in order to obtain the simplest, yet reliable, techniques for designing feedback loops for these bearings which have been adapted for the specific application in mind. The basic premise is that the system should be stable over the the widest possible range of operating conditions, it should preferably display no resonances (thus critically or overcritically damped), the settling times should be as short as possible and the positional errors during static operating conditions should preferably be zero (thus implying some form of integral feedback). If at all practical, the procedure followed in designing the feedback loops should be based on well known linear systems theory similar to that which has been published in the literature. However, the conditions under which the bearing will become unstable, ie where the linear model used is no longer a good enough approximation, should be clearly identified. The latter has not been done by previous workers and, based on the author's own experience with experimental bearings, is very important.

Any aspects or problems which can be identified which are peculiar or more pronounced to this application are to be dealt with, particularly if this has not been done previously. For instance, due to the high rotational velocities involved, it is impractical to use laminations or ferrites for the magnetic components. It is to be expected that eddy currents in these components will have a marked influence on the dynamic behaviour of the bearing. Since no previous treatment taking the latter into account can be found such an analysis will be done here in order to gain the necessary insight.

1.4 Chronological Development of this Investigation and Outline of this Thesis

In chapter 2 a superficial review of various types of magnetic bearing will be given. Qualitative arguments will be presented in favour of the so-called "5 active axis magnetic bearing" for application to flywheel energy storage systems.

Chapter 3 will be devoted to the derivation of a mathematical model of a magnetic bearing, where the current through the driving- or control coils is taken as the independent or externally controlled variable. This produces a set of nonlinear equations from which a new set of linear state equations are derived for "small displacements about the nominal point".

At the beginning of this investigation the above linear model was used in an attempt to design a feedback loop. Asymptotic stability of the bearing could be achieved ultimately after much trial and error adjustment of the feedback parameters which were initially calculated analytically. The dynamic behaviour of the system after such an exercise always left much to be desired. Similar problems have been reported by Jayawant [22] when controlling a suspension system in a similar fashion.

Finally a Bode diagram was drawn from the experimentally measured relationships between rotor displacement and driving coil voltage. A feedback loop, based on this Bode diagram was designed. This approach immediately produced significantly better results. Under certain conditions, however, the system would develop either stable or unstable limit cycles which obviously arose from the nonlinearities in the system but were not fully understood at this stage. A deeper investigation into this *voltage driven* system was thus essential. This is done in chapter 4 where it will be seen that by making the bearing *voltage driven*, some of the abovementioned nonlinearities are eliminated, making the mathematical analysis much more straightforward. A large signal model is then derived by making use of describing function techniques.

The dynamic behaviour problem of the current driven bearing was largely overcome by Jayawant [24] using a somewhat different approach. The driving coil current was still used as the system input, while, in addition to the position sensor, a Hall element was installed in the gap ("airgap" would be a misnomer since flywheels are operated in a vacuum) to measure the magnetic flux, effectively providing an additional feedback path for one of the system state variables. If the loop gain associated with this latter feedback path is sufficiently high, the inverse relationship between the flux and the gap length is effectively eliminated (see chapter 3). An approximately linear relationship will then exist between magnetic flux and the control signal derived from the position sensors. The system thus becomes more stable and more linear. The major disadvantage of this technique is the added complexity of the Hall sensor which has to be installed in the gap.

The rest of chapter 4 is devoted to a further refinement of the model of the mechanical system in order to obtain a transfer function for the total system that agrees more closely to the experimentally measured transfer function, which is also presented here.

The main objective of chapter 5 is to obtain a straightforward technique for designing a satisfactory feedback network for a magnetic bearing. After considering state variable feedback, by means of a state observer, it was concluded that a straightforward approach, making use of the Bode diagram of the transfer function, works just as well. After obtaining asymptotic stability by means of a feedback loop which has been designed around the analytically determined Bode diagram, this Bode diagram is then verified experimentally and any neccessary readjustments can be made to the feedback parameters. Due to the greater simplicity of the latter procedure, it is to be preferred.

An idea of using the driving coil voltage-current relationships as a measure for the rotor displacement, and

thus obviating the need of a position transducer, is also investigated in chapter 5. When put into practice this idea unfortunately did not work.

During this investigation, after the experimental bearings were operating successfully, it became apparent that rotor imbalance was problematic, particularly at high speeds, since this led to unacceptably high energy losses. A simple technique of discrete time filtering is presented in chapter 6 which effectively eliminates these losses in the magnetic bearing.

Chapter 7 is the final chapter where the results of this investigation are discussed and evaluated, magnetic bearings are evaluated in general and recommendations for follow-up work are made.

1.5 Originality and Novelty of this Thesis

Unless an explicit statement is made to the contrary in the text of this thesis , all the ideas, theories, mathematical derivations and techniques presented here are the author's own original work except for the occasional inclusion of such work which is obviously well known, but has been included for the sake of clarity and continuity in the development of certain arguments.

1.6 Description of experimental systems

The work presented in this thesis is based on experimental results obtained mainly from two magnetic bearings that were designed, built and tested for the purpose. The first (bearing no. 1) was a 30 Newton single radial bearing (2 active axes), driven by a router motor which could be spun up to 25000 r/min. and the second (bearing no. 2) a fully suspended (5 active axes) system where the radial displacement along two orthogonal axes at each shaft extremity as well as the axial displacement was controlled, in each case, by a set of diagonally opposed electromagnets. The latter had its own built in drive motor

and could be spun up to 13000 r/min., the material strength of the rotor being the limiting factor.

1.6.1 Single radial magnetic bearing (bearing no. 1)

Please refer to figures 1.3 and 1.5.

Magnetic circuit:

Due to the shape of the magnetic poles and the high rotational speed it is impractical to laminate the magnetic cicuit. An objective of this exercise was thus to determine how practical it would be to use solid steel for the entire magnetic circuit. The material chosen for this bearing was type 17-4PH Martensitic steel which was heat treated, prior to machining, in order to relieve any possible internal stresses, obtain the highest degree of magnetic softness according to the manufacturer's specifications and to improve the machineability of the material. According to the manufacturer the magnetisation curve of this steel, after heat treatment, corresponds very closely to that of mild steel. This was taken for granted. The main reasons for choosing this material were its high corrosion resistance, superior tensile strength and good machineability, making it far superior to mild steel.

Driving coils:

These coils were wound with 250 turns of 0,2mm diameter enamelled copper wire on a 30mm potcore coil former. The dc copper resistance was measured as 2,5Ω. The magnetising inductance (ie the inductance associated with the flux that crosses the gap between the stator and the rotor) was measured as 4,42 mH which compares very well with the calculated value of 4,3 mH obtained from eq. 3.8.

The above inductance was obtained by positionong a search coil of 10 turns in the gap so as to effectively couple with the total flux crossing the gap from one of the pole faces. The induced voltage in this search coil was used to derive the inductance as explained later in chapter 3.

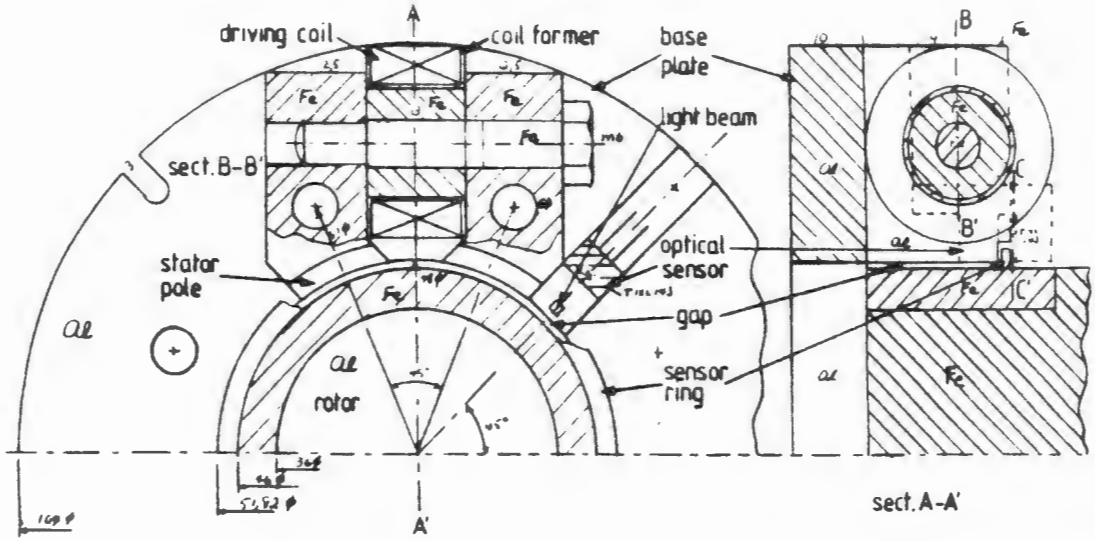

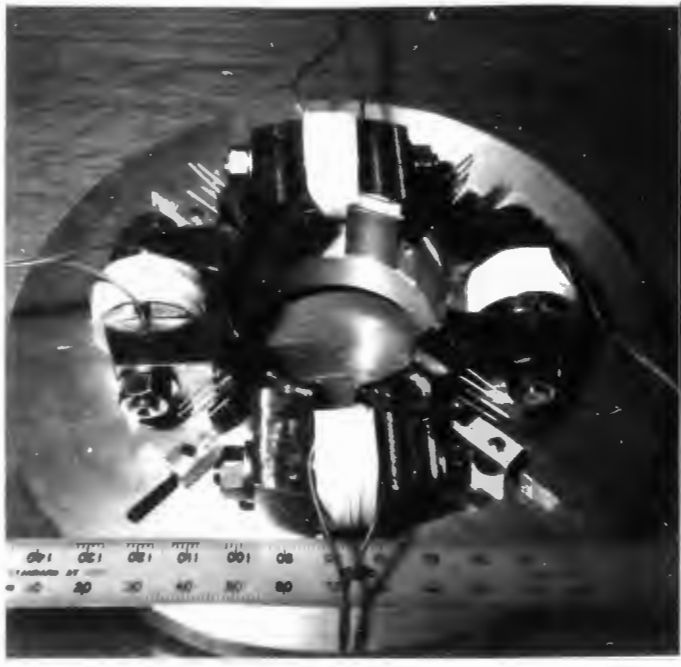

stator with control coils

and optical sensors

total system

FIG.1.3 SINGLE RADIAL MAGNETIC BEARING

Rotor:

The rotor assembly was constucted by shrinking the martensitic steel bearing element over the end of a solid aluminium shaft. A 3mmx100mm steel quill was fitted into the opposite end of the aluminium shaft. The loose end of this quill was clamped into the chuck of a 25000 r/min. router thus providing a flexible coupling for the purpose of driving the rotor at high speed. With this flexible coupling the magnetic bearing end of the rotor was, for all practical purposes, completely free to move in the radial plane with the driving coils in the demagnetised state. The rotor shaft was normally operated with its axis in the vertical direction and with the magnetic bearing on top, except when constant gravity loading tests were carried out, in which case the whole assembly was turned horisontally.

Position sensors:

Optical sensors were used on this bearing employing the same basic principle as that described in the literature [22],[24]&[42]. Instead of using an incandescant lamp etc., which may not always be very reliable, a commercially available so-called "source and sensor assembly" was employed which has an infrared light emitting diode which illuminates a phototransistor. Both these units are moulded into a single rugged plastic body with the infrared light beam crossing a slot in the stucture. Four of these assemblies were mounted around the cicumference of the rotor at 90 degree intervals between the stator driving magnets in such a way that one half of the above 1,27mm square light beam was interrupted by a thin flange on the rotor when the rotor was in its neutral position. A radial displacement of the rotor would cause a differential in the photocurrents of two diametrically opposed sensors. This differential current is then amplified, producing a displacement signal for the axis in question. By summing the displacement signals from these two orthogonal axes in

the correct sense, the displacements along the driving coil axes, which are displaced 45 degrees to the former, are obtained. By positioning the sensors between the driving coils in stead of directly in line with them, the whole bearing assembly can be made much more compact rendering it much more rugged and thus less susceptable to parasitic mechanical resonances, which could be very bothersome when attempting to optimise the system response (see later - chapter 5). Since the displacement along any one of the two driving coil axes is now derived from four sensors, in stead of one or two, this has an averaging effect which makes the system less sensitive to small irregularities on the rotor rim. Lastly, since the sensors are used as pairs in a differential mode, the position signals are less sensitive to temperature, voltage and ambient light fluctuations.

Discrete time notch filter: (see fig. 1.5)

This filter is fully described in chapter 6. Its function is to eliminate displacement signal which arise from imbalance of the rotor. It is only switched into the feedback loop at high speed when the sampling frequency, which equals the rotation frequency, is high enough so that the system will not become unstable. A circuit diagram of this filter is given in appendix 6A.

Compensator:

The magnetic bearing with positional feedback is closed-(as well as open-) loop unstable. The main objective of this thesis is, as stated previously, to synthesise H(s) in an optimal way so that, in the first instance, the system becomes stable and secondly, to provide the system with a suitable dynamic response. The reader is referred to chapter 5 for details where a circiut diagram of H(s) is shown in fig. 5.2.

Continuous time notch filter:

Parasitic mechanical resonances, particularly when weakly

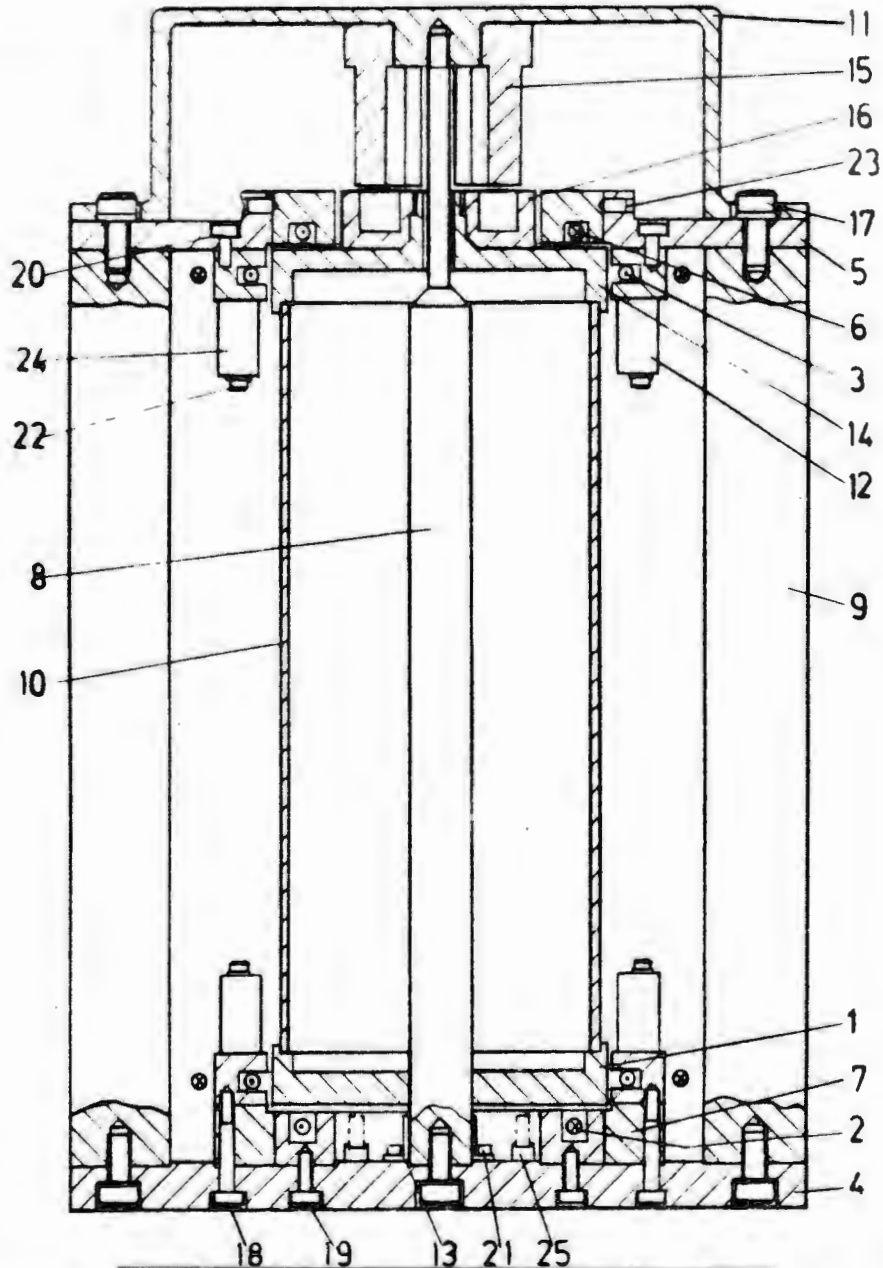

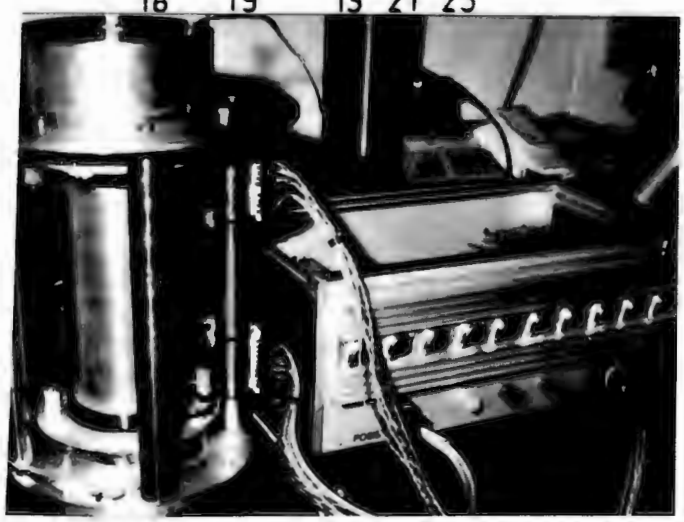

total system

FIG.1.4 EXPERIMENTAL 3-DIMENSIONAL MAGNETIC BEARING

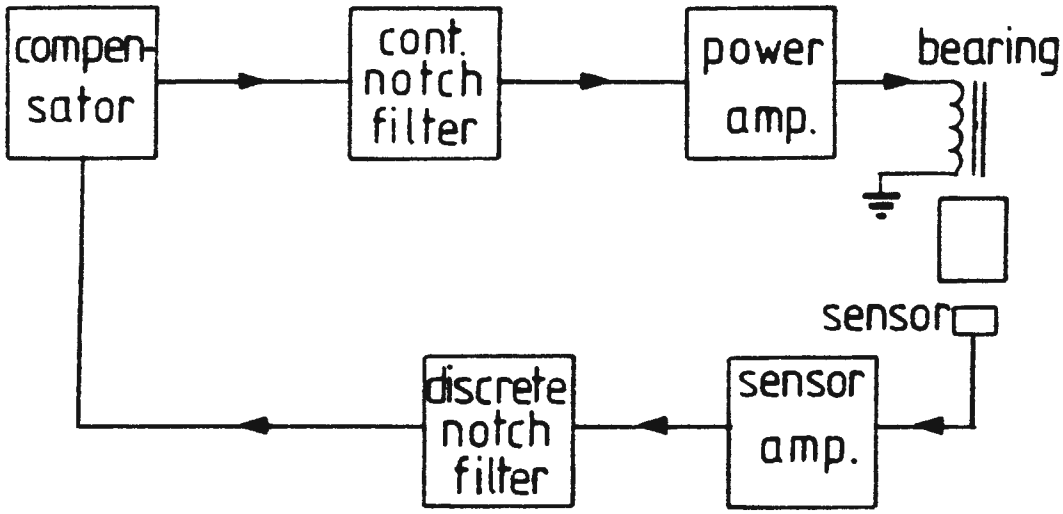

FIG. 1.5 BLOCK DIAGRAM OF CONTROL LOOP

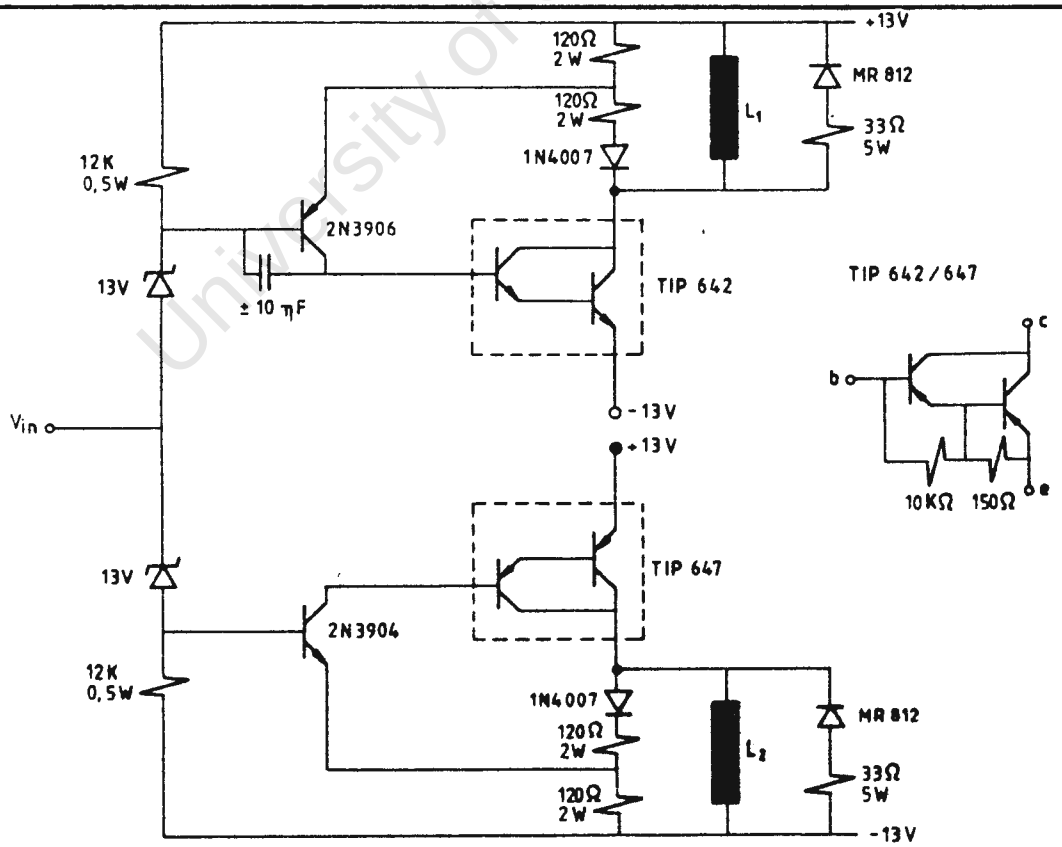

FIG. 1.6 POWER AMPLIFIER

damped, modify the dynamics of the system, leading to a degradation in performance and often to instability. This problem was experienced with the solid rotor shaft of this bearing. Since this rotor was required to operate at high speed, no simple form of mechanical damping could be incorporated. The problem was readily solved electronically with this notch filter which was tuned to eliminate the rotor resonance frequency of 925 Hz. A circuit diagram of the latter may be found in appendix 4A and further details are given in chapters 4 and 5.

Power amplifier:

A "pseudo class B" amplifier was used as shown in fig. 1.6. With a positive input signal, say e, a voltage $A_v e$ is applied to one of the driving coils (coil x^+), where A_v is the amplification factor of the amplifier. When the input signal changes polarity to say -e, the energy in coil x^+ is returned to the supply and a voltage $A_v e$ is applied to the opposite coil (x^-). The value of A_v was nominally 2.

1.6.2 The three dimensional (5 active axis) bearing

This bearing system is shown in fig. 1.4 and is mainly an extension of the above system to 5 (as opposed to 2) actively controlled axes. Conceptually the "other end" of the rotor which was coupled to the router motor via a flexible quill is now also provided with a radial bearing. An axial magnetic bearing is also added. The combination of the latter two bearings thus provide the positioning function formerly provided by the quill. A small 3-phase axial flux permanent magnet motor was built for driving the rotor. This motor was mounted on top of the bearing so that the attraction force between the permanent magnet on the rotor and the stator poles would counteract the gravity force on the rotor. This arrangement offers the possibility of investigating the so-called "virtual zero power" concept [25], in spite of the fact that it was realised all along that permanent magnets suitable for lifting a fullscale flywheel would be prohibitively expensive. This "virtual zero power" concept involves the balancing of the gravity

force on the flywheel exactly with the force set up by a permanent magnet. The only function of the driving magnets is then to maintain the rotor in this unstable state of equilibrium. Under quiescent conditions, with zero mechanical and electrical noise, the power delivered to the control coils is "virtually zero".

The control loops of this bearing were designed along the same lines as for the single radial bearing, the only major departure being in the type of position transducer used.

Table 1.1 **LEGEND to Fig. 1.4**

1	Rotor Bearing Element	13	Proximity Sensor
2	Axial Driving Coil (lower)	14	Rotor Bearing Element
3	Radial Driving Coil	15	Motor Stator
4	Base Plate	16	Magnet Holder (Motor)
5	Cover Plate	17	Capscrew
6	Axial Driving Coil (upper)	18	"
7	Spacer Ring	19	"
8	Central Pillar	20	"
9	Outer Pillar	21	"
10	Rotor	22	"
11	Motor Housing	23	Grubscrew
12	Proximity Sensor	24	Proximity Sensor

Inductive proximity sensors:

The ferrite core inductive sensor that was developed for this bearing undergoes an impedance change when its distance from a nearby forromagnetic and/or conductive surface changes. These sensors were, in the case of the four radial axes, also operated in a differential mode, similar to the optical sensors above. In the case of the radial axis, however, both sensors had to be mounted underneath the rotor with one serving as a position transducer whilst the other acted as a reference. When the surface that is sensed is predominantly conductive (as opposed to ferromagnetic) the sign of the position signal is inverted, as can be seen from the curves of fig.1.7. The

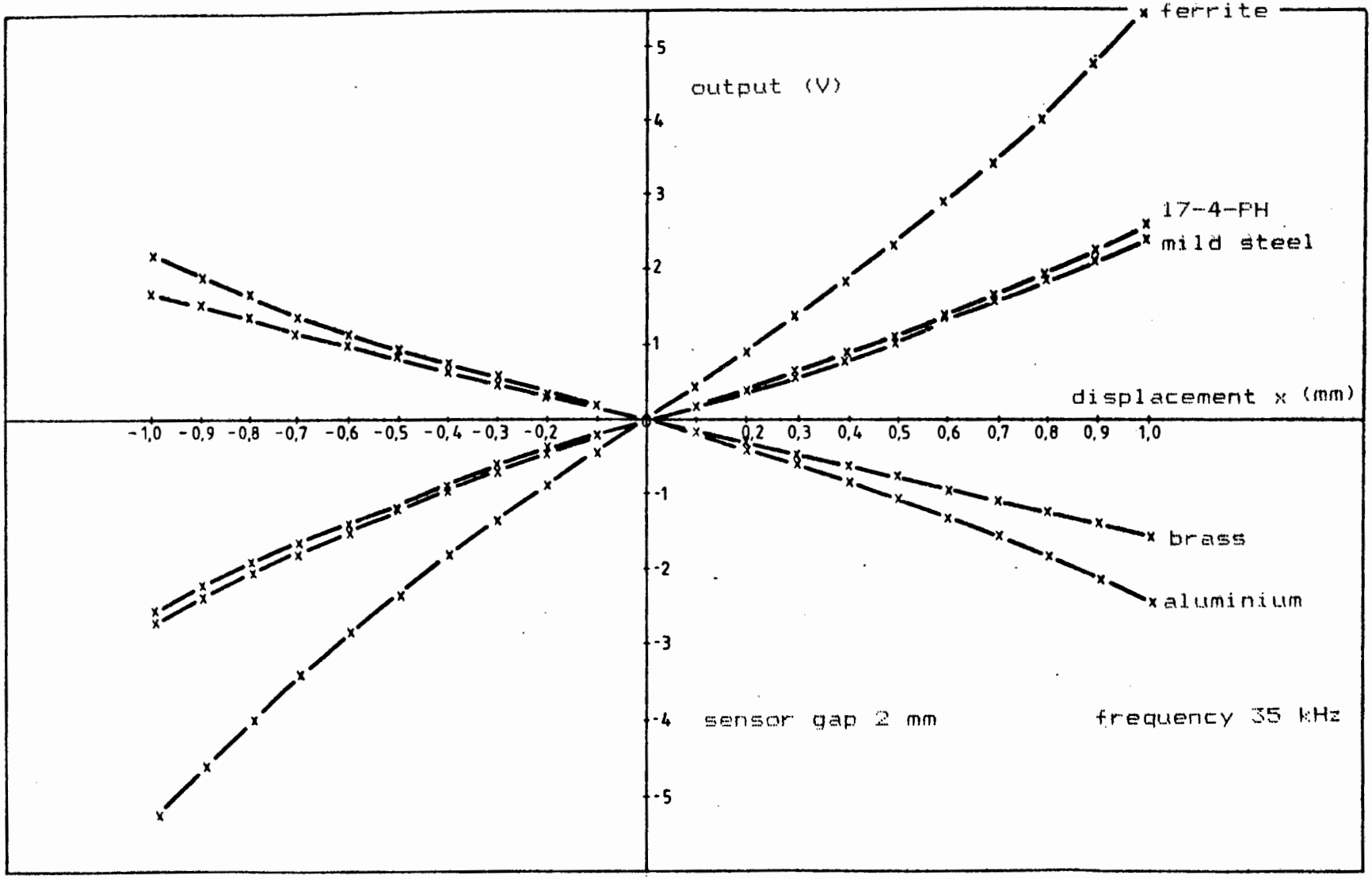

FIG.1.7 INDUCTIVE SENSOR CHARACTERISTIC

operation of these sensors is fully described in an internal report [26].

The main advantages of these proximity sensors are their lower sensitivity to minor surface irregularities than optical sensors, no special shapes such as thin flanges etc. on the rotor are required as in the case of the optical sensors and, as a consequence of the latter, one has a greater freedom of choice in their placing. The major disadvantage that was experienced was their sensitivity to magnetic interference which made it impractical to mount them between the driving magnets such as was done with the optical sensors in bearing no.1. Even after moving them some distance away considerable effort was required to provide adequate magnetic screening as well as filtering of the sensor signal. Initially the parasitic feedback caused by this coupling between the drive magnets and the sensors was so severe that the dynamic performance of the system was severely degraded, a situation which could not be improved by simply adjusting the feedback parameters. However, after the above screening and filtering was successfully carried out very desireable dynamic performance characteristics could be obtained.

Multi-variable feedback control:

It was realised from the beginning that with the method of control employed here a certain amount of cross-coupling was to be expected between the various control loops. This cross-coupling arises from rotor dynamics and, with the rotor stationary, has the same nature as the cross-coupling which is experienced with multi-point magnetic suspension of vehicles [22],[27]&[42]. With a rotating rotor the situation becomes much more complex due to the gyroscopic effects of the rotor. A general analysis of the dynamics of this rotating body is not possible because of the complexity and non-linearity of the system (see, for instance, ref[28]). An approximate transfer function matrix, which relates all the displacements of the rotor to all the input forces may be derived by making various "linearising assumptions". These assumptions are valid if

one considers that, due to the mechanical restraints placed on the movement of the rotor, the angular displacements of the rotor can only be very small. Such a transfer function matrix was derived by the author using a different approach to that of Craig [29] for the dynamically tuned gyroscope. Identical results were obtained, however. This transfer function matrix could not be verified experimentally since the gyroscopic and other cross-coupling effects of the experimental rotor were so small that they were swamped by noise. This observation indicates that, at least for this experimental experimental 3-dimensional bearing, all cross-coupling may be ignored and the feedback loops designed seperately. The transfer function matrix is thus considered to be purely diagonal. Using this approach with the experimental bearing, very satisfactory results were obtained in practice. Since no experimental verification of the abovementioned analysis can be presented this work will not be included in this thesis. It will hopefully be reported on at a later stage.

CHAPTER 2

TYPES OF MAGNETIC BEARINGS

In order to set the background, this chapter is mainly a superficial and qualitative review of various types of magnetic bearings. In most cases purely qualitative arguments are sufficient to indicate whether the particular bearing under consideration is suitable for flywheel energy storage applications.

For the sake of convenience magnetic bearings may be divided into two main categories, ie:
1 Repulsion type magnetic bearings and
2 Attraction type magnetic bearings.

2.1 Repulsion Type Magnetic Bearings

This category may again be subdivided into eddy-current or induction magnetic bearings and double magnet bearings.

2.1.1 Eddy-current Bearings

This type, which has been investigated extensively (see, for instance the bibliography which is given in reference [22]), is normally applied to high speed vehicles, such as trains, where a strong magnetic field is set up by cryogenic superconducting magnets in one of the two elements, normally the one on the vehicle, whilst the other element (the rail) consists of a conductive sheet. Due to relative motion between the two elements eddy currents are induced in the conductive sheet which oppose the moving magnetic field. The vehicle experiences levitational as wel as drag forces. A great advantage of such a levitational system is that it is inherently stable and well damped. Disadvantages are that levitation is lost below a certain minimum relative velocity and, more important, the drag forces are so high that this type of magnetic bearing is impractical for flyweel energy storage systems (see Nasar, Boldea, 1976, [23]).

2.1.2 Double Magnet Bearings

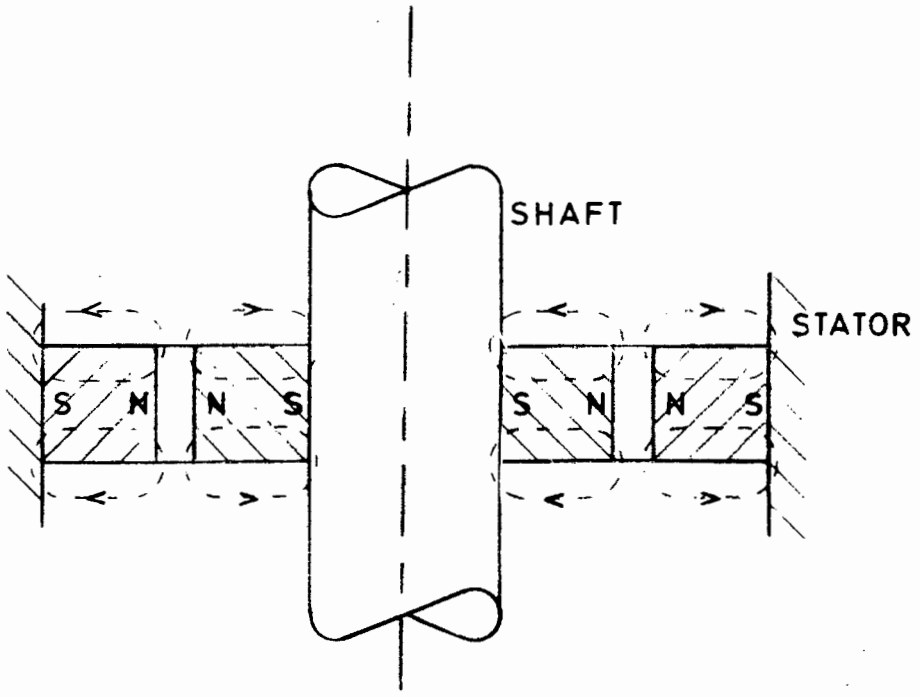

FIG. 2.1 REPULSION RADIAL MAGNETIC BEARING with PERMANENT MAGNETS

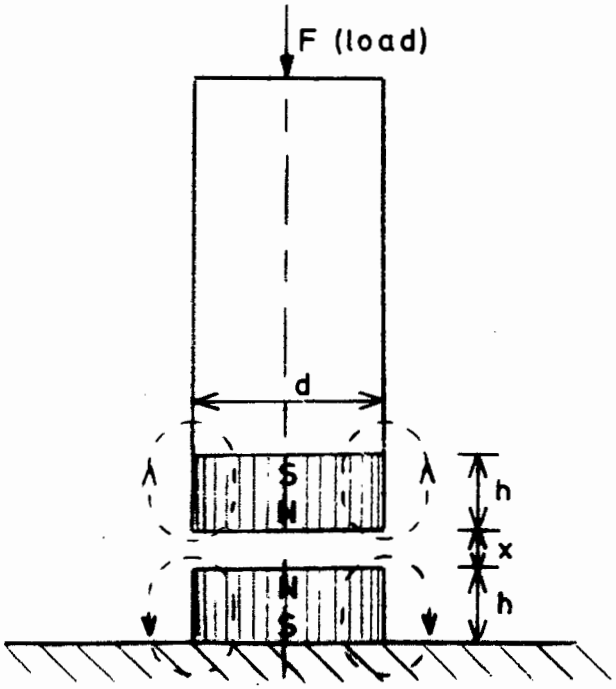

FIG. 2.2 REPULSION AXIAL MAGNETIC BEARING with PERMANENT MAGNETS

In this type of bearing either a permanent- or an electromagnet is mounted in each one of the elements, with like poles facing each other, resulting in the elements repelling each other. In figures 2.1. and 2.2. two examples of these bearings are shown.

According to Earnshaw [30], a body can be stabilised by the above procedure in at most two of the three geometric dimensions. In the third dimension either a servo system or mechanical bearings are required for stability. Wang and Marx [31] report on the development of a three dimensional bearing, of this type, where the above stability problem was overcome means of servo controlled electromagnets, replacing the permanent magnets in at least one of the axis.

Because of the relatively small BH product, and consequently small repulsion forces, that could be obtained in the past with permanent magnets, this technique has only been applied to very light rotors such as, for instance, Watt-hour meters [20]. This maximum BH product was typically $30kJ/m^3$. With modern rare earth magnets such as samarium cobalt ($SmCo_5$) this figure has been raised to approximately 120 kJ/m^3 with a corresponding increase in repulsion forces. In an experiment carried out with samarium cobalt magnets, as shown in fig. 2.2, repulsion forces were measured according to the graph in fig. 2.3.

The repulsion type bearing, when constructed with permanent magnets, is virtually lossless, and thus may be considered to be ideal in this respect.

At the time of this writing, however, rare earth permanent magnets are prohibitively expensive for suspension of energy storage flywheels. It may be argued that electromagnets are ultimately more expensive because they continuously draw power. It is estimated, however, that the power consumption for suspending an 18 MJ flywheel could be as low as 10 Watts which represents an anual energy consumption of 87,66 kWh. It is most unlikely that the cost

of the latter amount of electric energy will ever exceed the interest on the capital for permanent magnets which will cost approximately R2000-00. This type of bearing will thus not be considered any further in this investigation.

2.2 The Attraction Type Magnetic Bearing

Such a system may consist of permanent magnets, electromagnets or a combination of both, where, as implied by the name, attraction forces are employed. This type of bearing is inherently unstable but offers the advantage that it can support greater forces than the repulsion bearing. In systems incorporating permanent magnets the losses could theoretically approach zero since the permanent magnets could provide the main lifting force, hence no quiescent current is required as explained in chapter 1 section 1.6.2 and ref. [25].

In a larger system, such as will be investigated here, where economic considerations exclude the use of permanent magnets, iron losses may nevertheless approach a theoretical zero (see later) whilst copper losses may be kept low enough by carefull design to render the system practical for long term energy storage applications. Attraction type magnetic bearings were probably firstly incorporated into gyroscopes and later into momentum wheels and flywheel energy stores in spacecraft (Poubeau, 1977, [32]). More recently they are being used in turbomolecular pumps [33] and presently are finding their way into high precision machine tools [34] and probably many other applications.

2.2.1 The Resonance Magnetic Bearing

This is a sub-category of the attraction type magnetic bearing which has been investigated by Kaplan [35][36], Jayawant and Rea [37]. In a publication by Frazier, Gilinson and Oberbeck [44] this type of bearing has been dealt with exhaustively. It possesses a significant advantage over most other attraction type bearings because of its inherent so-called "static" stability, in the sense

that no servo system is required. Dynamically its performance is not acceptable and special damping mechanisisms are required which are described in the above references. Basically two stationary electromagnets are placed on opposite sides of the rotor or moveable element of the bearing. An alternating current of fixed frequency f_o is caused to flow through both of these electromagnets, causing opposing pulsating magnetic forces to act upon the rotor. With the rotor in the neutral position both electromagnets will have equal inductance. With equal applied voltages equal currents will flow, giving rise to equal but opposing forces. The rotor thus experiences zero resultant force. Equal capacitors are coupled in series with each of the electromagnets, the values of which have been chosen to "detune" the resultant LC networks slightly from f_o. This "detuning" is chosen so that should the rotor move away from say electromagnet no.1, the resonant frequency of LC network no. 1 will shift closer to f_o due to the resultant inductance change. The current in this circuit rises sharply, provided that the "Q" is high enough. At circuit no. 2 the opposite happens. The end result is a restoring force on the rotor.

The major disadvantage of this technique arises from the fact that an ac power supply is required which gives rise to constant iron losses in the bearing. The significance of this becomes more apparent when considering the fact that the rotor element of the magnetic bearing cannot be laminated easily, nor can it be manufactured from ferrite materials, due mainly to mechanical strength considerations for high speed operation.

2.3 Magnetic Bearing Configurations and Geometry

As mentioned previously, due to Earnshaw [30], at least one of the axes of the totally magnetic bearing system has to be controlled actively by a servo loop. The following three configurations are thus possible.

2.3.1 Radially Passive, Axially Active Bearing

This configuration is suitable for applications where very

low or zero acceleration forces are encountered in the radial plane, such as with a vertical axis stationary flywheel where the required radial restoring forces are very small. Sufficient damping in the radial plane may be obtained by means of passive eddy current dampers [19].

For stationary terrestrial applications the constant gravitational force has to be counterbalanced by the axial bearing. Provided the elements of the latter posess an axi-symmetrical geometry, no iron losses will be experienced in spite of the constant magnetic flux through the elements and relative high speed rotation. This is explained later.

A disadvantage of this configuration is the fact that the drive motor/generator should preferably be of the more expensive axial air gap type since a radial air gap motor may develop radial magnetic imbalance forces which may become too large for the passive radial bearing.

2.3.2 Axially Passive, Radially Active Bearings

Due to the high cost of permanent magnets the main loads placed on the bearing would normally be supported by the active axes. Furthermore, an active radial bearing is always lossy under load because it has to be controlled independently along the two orthogonal radial axes. Usually four stator poles would be required (two per axis). Under load and with rotation the rotor element would thus experience cyclic changes in magnetic flux density, with associated iron losses (see later chapter 7).

Although this configuration would be suitable for small vertical axis rotors such as, for instance, gyroscopes, it will not be dealt with any further in this investigation due to the drawbacks it poses for larger systems.

2.3.3 Fully Active Magnetic Bearings

As the name implies, all axes are actively controlled by means of feedback loops. This is certainly the most

versatile configuration and can be used under virtually all conditions, the only disadvantage being its complexity. Typically five axes have to be controlled actively (ie two radial axes per shaft end and one axial axis).

With the foregoing discussion in mind this configuration becomes an obvious choice for mobile bulk energy storage systems. In the following chapters the actively controlled bearing will thus be analysed in detail.

CHAPTER 3

THE CURRENT DRIVEN MAGNETIC BEARING WITH INFINITE MASS STATOR

From now on, for the sake of brevity, the term *magnetic bearing* will be used to replace "actively controlled attraction type magnetic bearing" (see chapter 2).

In this chapter the equations describing the behaviour of the above bearing, similar to the equations of chapter 5 in reference [22] and also in ref.[27], are derived. The main difference is that the core eddy current effects are also taken into account. The influence of eddy currents has been considered by Bohn [46] for an electromagnetic levitation system employing solid tracks and magnetic cores. The eddy currents in the latter case are continuously induced with vehicle movement and the primary concern is the resultant loss of levitation and the asssociated drag on the vehicle which leads to an increased power consumption. In this investigation the main interest lies in the influence which the eddy current have on the dynamic performance of the feedback system. As pointed out later on, the eddy currents here are only of a transient nature and associated power losses are thus of secondary importance. Bohn has thus adressed an altogether different problem. The equations characterising the system will be written as a set of nonlinear state equations which will then be used to obtain a set of linear state equations describing the dynamic behaviour of the rotor for very small displacements from its neutral or "zero" position. A similar state space linear model was also derived by Gottzein and Lange [27] for a linear motion bearing (suspended vehicle) where variation in track height is one of the prime considerations. The latter phenomenon is absent here and as a consequence a different and more suitable state vector is chosen. In any case, this analysis is more detailed than can be found in any of the above references. It is felt that, although such detail may be considered to be superfluous by the expert, it is essential for the uninitiated reader.

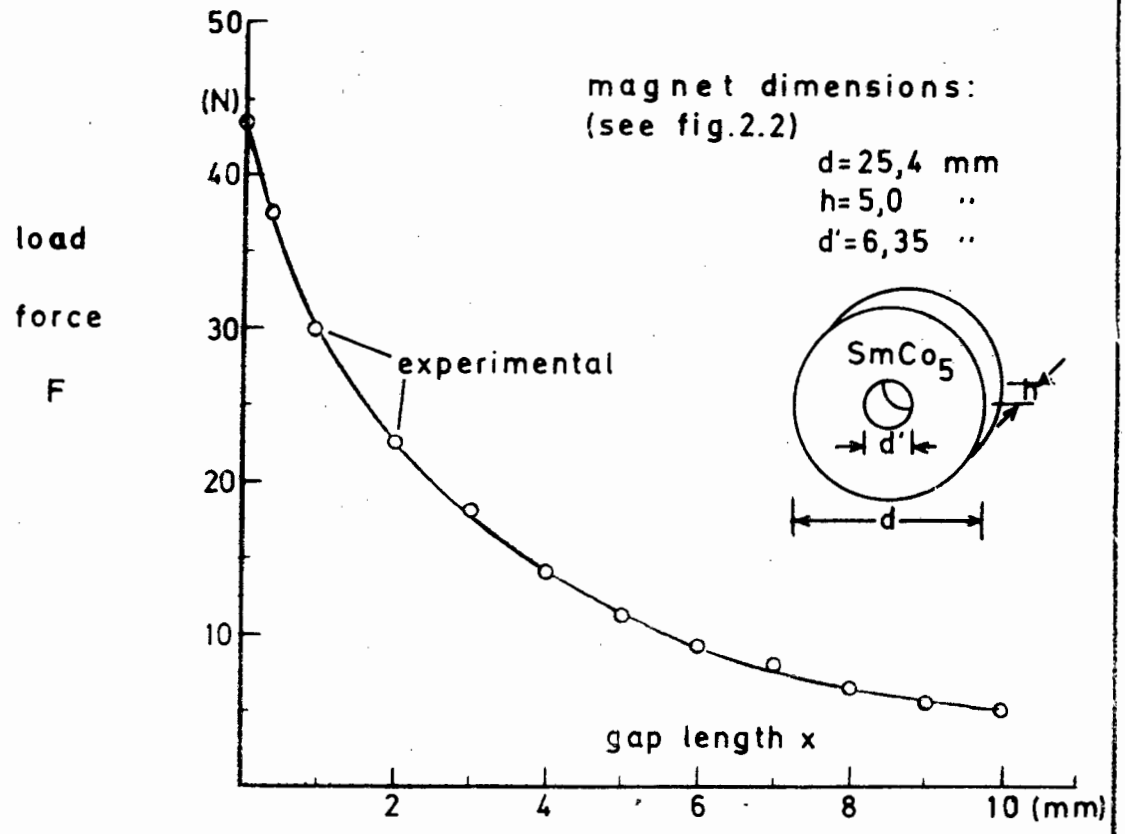

FIG. 2.3 CHARACTERISTIC of REPULSION BEARING

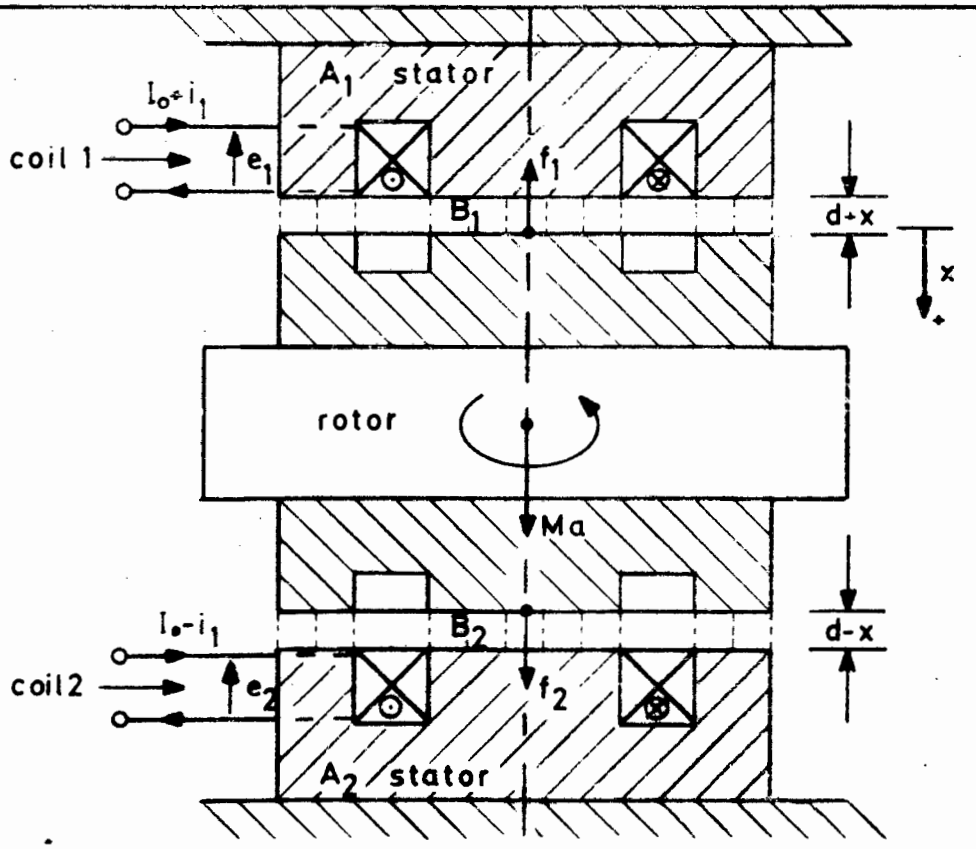

FIG. 3.1 ACTIVE AXIAL MAGNETIC BEARING

The various axes of the bearing system are initially assumed to be orthogonal to each other and are thus considered to operate independently with little or no mutual influence. The basic principles governing the behaviour of the bearing are the same for all axes, consequently only one axis (ie the axial one) will be analysed and the results obtained may then be applied to any other axis with the neccessary change in parameters.

3.1 The Physical System

An axial bearing is shown in its simplest form in fig. 3.1. Two electromagnets, A_1 and A_2, form the stator elements. The magnetomotive forces (mmf's), which are set up by the coils of A_1 and A_2, result in magnetic flux densities B_1 and B_2 which couple with the rotor elements and in turn cause opposing magnetic forces f_1 and f_2 to act upon the rotor. The rotor will be in equilibrium provided

$$f_1-f_2=Ma \text{ (N)} \qquad (3.1)$$

where M=total mass of the rotor (kg)
and a=total acceleration experienced by the rotor (m/s^2).

At this stage it is of interest to note that, in the absence of a radial bearing, the system in fig. 3.1 is inherently stable in the radial plane, because any radial displacement of the rotor will cause an increase in the reluctance of the magnetic flux paths resulting in an associated radial restoring force. Further, with the rotor in the radially neutral position, it is quite evident that, in spite of normal rotation of the rotor, no closed path can be found in either of the elements where any change in flux coupling takes place. Thus no voltages are induced in the elements and no eddy currents, with associated losses, will flow. Because no change in magnetisation takes place, no hysteresis losses will occur either. This lossless operation is due to the axial symmetry of the elements.

3.1.1 Assumptions and Simplifications

Assume the coils and all other parameters of the pole pairs 1 and 2 to be identical. Generally the rotor has an axial displacement of x (m) from the central or neutral position in the axial direction. With the rotor in the neutral position the distance between the elements of both pole pairs is d (m).

Under no-load conditions and with the rotor stationary in the axially neutral position, equal quiescent currents $I_o > \emptyset$ are forced to flow in both coils 1 and 2.

Under transient or non-equilibrium conditions a control current $i_1(t)$ is superimposed upon I_o in such a way that the resultant currents for coils 1 and 2 ie $i_2(t)$ and $i_4(t)$ respectively, will never go negative nor exceed the allowed maximum current I_m.

Thus:

$$\left.\begin{array}{l} i_2(t) = \begin{cases} I_o + i_1(t) & \text{for } -I_o < i_1(t) < I_m - I_o \\ \emptyset & \text{for } i_1(t) < -I_o \\ I_m & \text{for } i_1(t) > I_m - I_o \end{cases} \\ \text{and} \\ i_4(t) = \begin{cases} I_o - i_1(t) & \text{for } I_o - I_m < i_1(t) < I_o \\ \emptyset & \text{for } i_1(t) > I_o \\ I_m & \text{for } i_1(t) < I_o - I_m \end{cases} \end{array}\right\} \quad \text{(A)} \ldots (3.2)$$

where $I_m > I_o$ is the maximum current that can flow in either coil due to the current limit of the servo amplifier that drives the coils. The restrictions indicated in equations (3.2) imposed on i_2 and i_4, preventing either from going negative, are necessary because the magnetic forces acting upon the rotor are only dependent on the magnitude of the magnetising currents and not on their sign (see later eq. (3.12)).

It is further assumed that the reluctance of the air gaps between the pole pairs is dominant, thus the reluctance of the iron is neglected. This assumption implies flux

densities in the iron which are well below the saturation level.

Initially it will be assumed that the stator elements are infinitely large or immoveably fixed to mechanical "ground" and can consequently, not be displaced. This obviously does not agree with the practical situation but is a simplification which is brought in to gain an initial "feel" for the system under investigation. Later on this restriction will be removed to provide a more general and accurate model of the system.

3.2 Equivalent Circuit of the Electromagnets

As stated previously, the rotor elements of the bearing have to be solid steel components. Furthermore the stator elements, particularly in the case of the axial bearing being considered, should preferably also be machined out of solid steel as it would be difficult and costly to obtain such a shape in laminated form. The result of employing this unlaminated structure is that eddy currents will flow during flux changes of the magnetic field which in turn will influence the dynamic behaviour of the system.

The effect of the above eddy currents can be represented most conveniently by a resistor r_1 connected in parallel with the magnetising inductances L_1 and L_2 of the coils (see fig. 3.2).

The above iron resistance r_1 can be determined by an experimental Bode plot of either $e_1/i_2(t)$ or $e_2/i_4(t)$, where e_1 and e_2 are the induced voltages across coils 1 and 2 respectively. In appendix 3A it is shown, from experimental data, that this representation is a fair approximation of the true physical system. This model is only valid at relatively low frequencies, as shown in fig. 3A.1. At high frequencies other parasitic effects dominate, as can be expected.

The effective value of the magnetising inductance L_o (see eq. (3.8), sect.3.3) was determined experimentally as

follows:

Referring to fig. 3.2 a voltage transfer function A(s), relating the the voltage e_1 to the driving coil voltage, may be derived:

$$A(s)=\frac{r_1 s}{L_{le}\left(s^2+\frac{r_1 L_1+r_1 L_{le}+r_{cu} L_1}{L_1 L_{le}}s+\frac{r_1 r_{cu}}{L_1 L_{le}}\right)} \quad \text{.....(3.2a)}$$

With the poles of A(s) real and spaced widely apart

$$A(s_{mid})\doteq\frac{L_1}{L_1+L_{le}} \quad \text{.....(3.2b)}$$

Where $A(s_{mid})$ is the transfer function of the equivalent circuit in the frequency range between the two poles of A(s). The frequency response of A(s) is determined experimentally by placing a search coil in the gap between the rotor and stator just large enough to couple with all the flux that crosses the gap from one pole. The voltage induced in this search coil

$$e_s=e/N \quad \text{.....(3.2c)}$$

where N is the turns ratio between the driving coil and the search coil. The input voltage is obviously measured directly across the driving coil terminals.

Such a frequency response was measured for bearing no.1 and is presented in a Bode plot in fig. 3.1a. It can be seen here that $A(j\omega_{mid})=-6dB$ thus $L_1=L_{le}$. The total inductance L_1+L_{le} was measured in the same frequency range and found to be 8,84 mH, thus $L_1=4,42$ mH which is surprisingly close to the theoretical value of 4.3 mH calculated with eq. (3.8). By using the same Bode plot and this value of L_1, r_1 is determined from the high frequency cutoff $f_h=5$ kHz where the phase angle of $A(j\omega)$ is -45 degrees. r_1 is found to be 138,8 Ω.

The parameters for this driving coil are the following:

Effective pole area	$A=2,28\times10^{-4}$ m^2
Number of turns	$n=245$
Gap length	$d=10^{-3}$ m
Number of turns on search coil:	10
DC driving coil resistance	$r_{Cu}=1,85$ Ω.

Conclusion: From the above results and the Bode plot of fig. 3.1a it may be concluded that, although the model developed here for the driving coils appears to be rather rudimentary, it nevertheless seems to be fairly accurate.

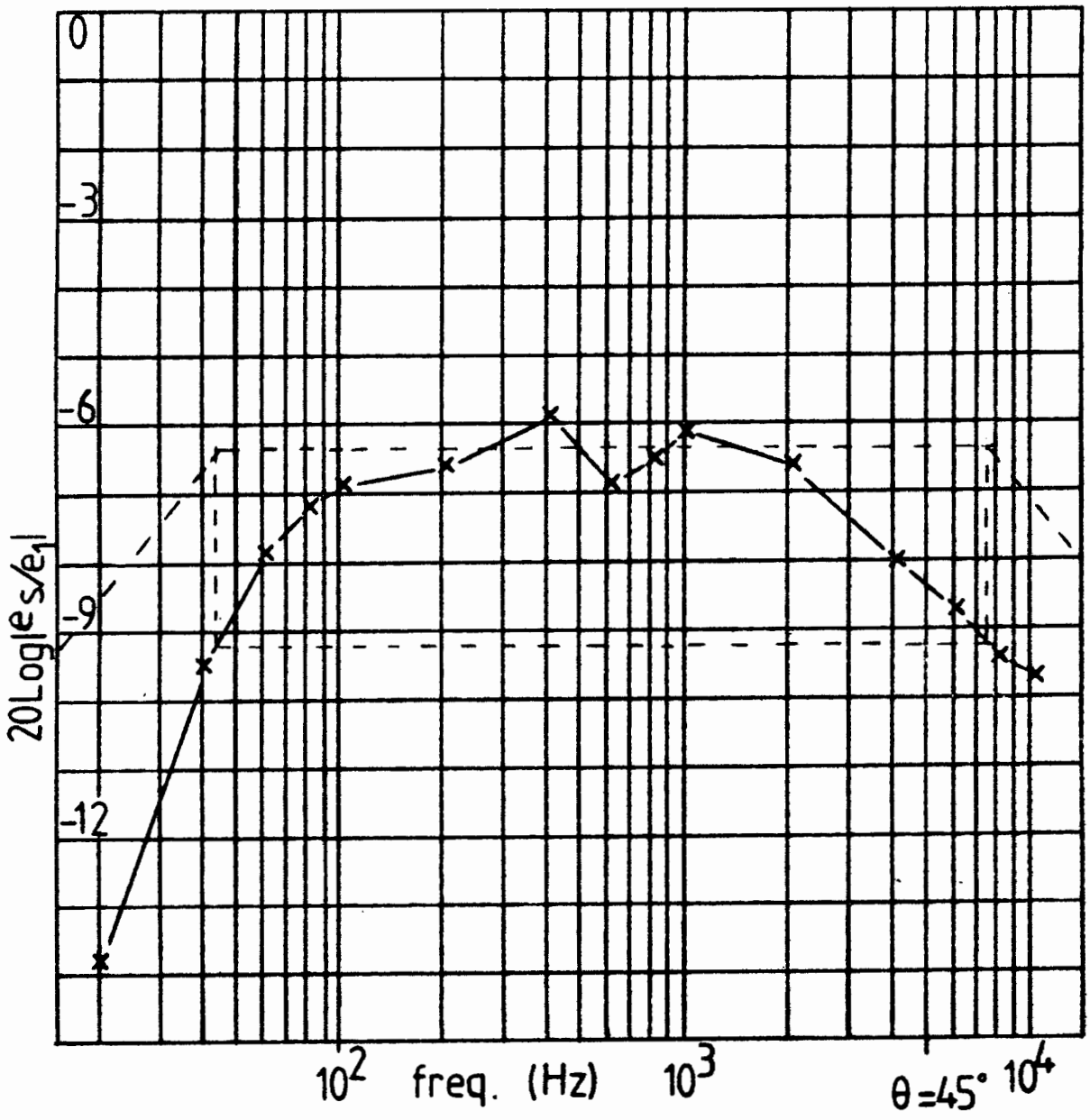

FIG.3.1a CHARACTERISTIC OF CONTROL COIL

3.3 Magnetic Forces on the Rotor

Referring to fig. 3.2 it can be seen that, due to the shunting effect of r_1, the total coil current $i_2(t)$ does not flow through the magnetising inductance. The true magnetising current is thus

$$i_{m1}=I_o+i_3(t)=i_2(t)-e_1/r_1 \quad (A) \qquad (3.3a)$$

and similarly for coil 2:

$$i_{m2}=I_o+i_5(t)=i_4(t)-e_2/r_1 \quad (A) \qquad (3.3b)$$

The following relations are thus valid for coil 1:

The magnetic field strength $$H_1=\frac{n(I_o+i_3)}{2(d+x)} \quad (A/m) \qquad (3.4)$$

where n=number of turns on coil 1.

The magnetic flux density $$B_1=\frac{\mu_o n(I_o+i_3)}{2(d+x)} \quad (Tesla) \qquad (3.5)$$

where μ_o=permeability of the gap=$4\pi\times10^{-7}$ (H/m)

The magnetic flux $$\varphi_1=\frac{\mu_o An(I_o+i_3)}{2(d+x)} \quad (Weber) \qquad (3.6)$$

where A=effective pole area (m^2)

The induced coil voltage $$e_1=n\frac{d\varphi_1}{dt}=dL_o\frac{d}{dt}\left[\frac{I_o+i_3}{d+x}\right] \quad (V) \qquad (3.7)$$

where $L_o\triangleq\frac{\mu_o An^2}{2d}$ is the coil inductance at x=Ø (H) (3.8)

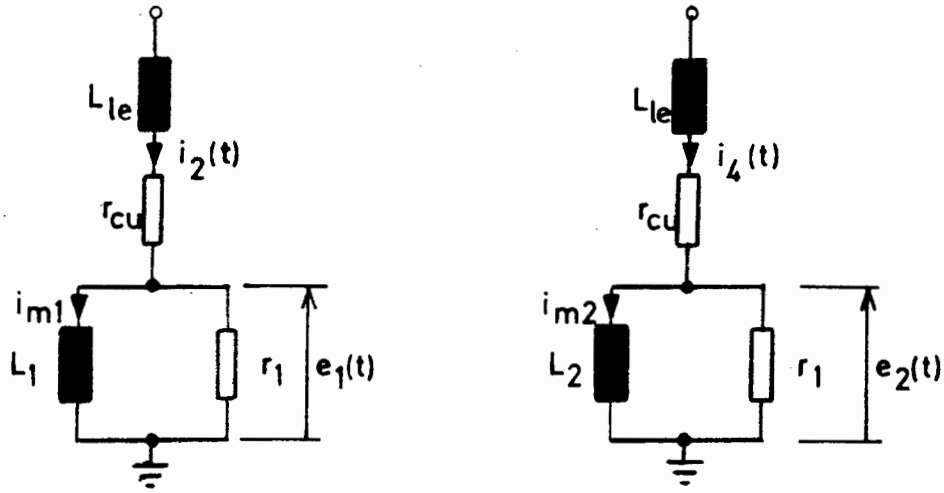

FIG. 3.2 EQUIVALENT CIRCUITS of MAGNETIC BEARING CONTROL COILS

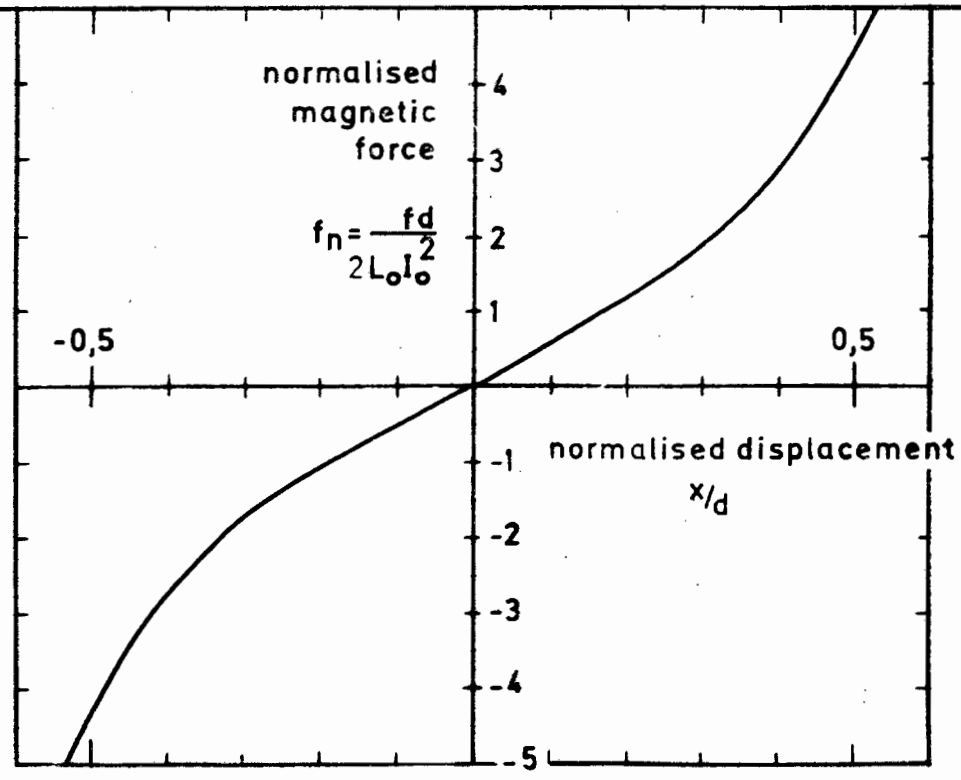

FIG.3.3 MAGNETIC FORCE vs. DISPLACEMENT for EQUAL and CONSTANT COIL CURRENTS I_O

The stored energy in the gap $W_1 = (B_1 H_1/2) \times$ gap volume

$$= \frac{\mu_o n^2 (I_o + i_3)^2 A}{4(d+x)} = \frac{L_o d (I_o + i_3)^2}{2(d+x)} \quad (J) \qquad (3.9)$$

The magnetic force between the poles

$$f_1 = \frac{\delta W_1}{\delta x} = \frac{-L_o d}{2}\left[\frac{I_o + i_3}{d+x}\right]^2 = \frac{-\varphi_1^2}{\mu_o A} \quad (N) \qquad (3.10)$$

Similarly the attraction force between pole pair 2

$$f_2 = \frac{L_o d}{2}\left[\frac{I_o + i_5}{d-x}\right] = \frac{\varphi_2^2}{\mu_o A} \quad (N) \qquad (3.11)$$

The resultant magnetic force on the rotor

$$f = \frac{L_o d}{2}\left[\left[\frac{I_o + i_5}{d-x}\right]^2 - \left[\frac{I_o + i_3}{d+x}\right]^2\right] \quad (N) \qquad (3.12)$$

From equation (3.12) it can be seen that for $i_3 = i_5$ the sign of f is such that it would tend to increase any displacement $x \neq 0$ irrespective of the sign of x, which provides some insight into the inherent instability of the system when no feedback is applied. With $x = 0$, $i_3 = i_5$ and no gravitational or other load, the rotor will be in a state of unstable equilibrium. In fig. 3.3 the force f is shown graphically as a function of x, for $i_3 = i_5 = I_o$, normalised with respect to L_o, d and I_o. Here it can also be seen that a new equilibrium state may be obtained for various external forces f_e whilst maintaining $i_3 = i_5 = I_o$ and merely selecting a new displacement x where $f = f_e$.

3.4 Linear Model from the Nonlinear Equations

From the previous section it is clear that we are dealing with an open-loop unstable nonlinear system (see for instance, eq (3.12)). When confronted with the problem of designing a feedback loop the most straightforward approach seems to be that of deriving a linear model for very small displacements from the neutral position whereupon standard linear control techniques may be employed in the design of the feedback loop which would then ensure good stability

and dynamic behaviour at least in the vicinity of this point. After having gone through this procedure further measures can then be taken to compensate for the system nonlinearities should it prove to be necessary. At this stage it is thus essential to obtain such a linear model.

Firstly a set of state variables have to be selected for describing the dynamic behaviour of system in a set of nonlinear state equations. An obvious choice for these variables would be all the variables representing stored energy in the system such as:

1. displacement x - for potential energy in a gravitational field,
2. velocity v=dx/dt .....(3.13)
for kinetic energy of the rotor due to linear motion,
3. flux φ_1 for stored magnetic energy, mainly in the gap of pole pair 1, and
4. flux φ_2 for stored energy, mainly in the gap of pole pair 2.

Alternately i_3 and i_5 may be chosen in the place of φ_1 and φ_2, also representing stored magnetic energy (expressed as $Li^2/2$). Irrespective of the choice of variables, the stored magnetic energy will also be a function of the state variable x as seen in eq. (3.6). Since fluxes $\varphi_{1\&2}$ are relatively complex functions of current i and displacement x, i_3 and i_5 will be preferred. Most important, however, is that the selected state vector

$$\mathbf{x}=[x \; v \; i_3 \; i_5]^t \quad \text{.....(3.14)}$$

(where 't' denotes the transpose of the given row vector) is a minimal set totally describing the state of the system.

From equations (3.2), (3.3), (3.7), (3.12), (3.13) and Newton's second law of motion, the following set of nonlinear state equations are obtained (see Appendix 3B):

$$\left.\begin{aligned}
\dot{x} &= v && (m/s)\\
\dot{v} &= \frac{L_o d}{2M}\left[\left(\frac{I_o + i_5}{d-x}\right)^2 - \left(\frac{I_o + i_3}{d+x}\right)^2\right] - a && (m/s^2)\\
\dot{i}_3 &= \left(\frac{I_o + i_3}{d+x}\right)v - \frac{r_1(d+x)}{dL_o} i_3 + \frac{r_1(d+x)}{dL_o} i_1 && (A/s)\\
\dot{i}_5 &= -\left(\frac{I_o + i_5}{d-x}\right)v - \frac{r_1(d-x)}{dL_o} i_5 - \frac{r_1(d-x)}{dL_o} i_1 && (A/s)
\end{aligned}\right\} \quad \ldots\ldots\ldots\ldots (3.15)$$

Where the external acceleration a and the control current i_1 are taken as independent inputs to the system.

From eq. (3.15) the Jacobian matrices [38][39]

$$\mathbb{A} = \begin{bmatrix} \emptyset & 1 & \emptyset & \emptyset \\ \dfrac{2L_o I_o^2}{Md^2} & \emptyset & \dfrac{-L_o I_o}{Md} & \dfrac{L_o I_o}{Md} \\ \emptyset & \dfrac{I_o}{d} & \dfrac{-r_1}{L_o} & \emptyset \\ \emptyset & \dfrac{-I_o}{d} & \emptyset & \dfrac{-r_1}{L_o} \end{bmatrix} \quad \text{and} \quad \mathbb{B} = \begin{bmatrix} \emptyset & \emptyset \\ -1 & \emptyset \\ \emptyset & \dfrac{r_1}{L_o} \\ \emptyset & \dfrac{-r_1}{L_o} \end{bmatrix} \quad \ldots\ldots\ldots (3.16)$$

are found (see Appendix 3B).

The corresponding linear state equations for small displacements of $\mathbb{X}$ about the nominal point are

$$\dot{\mathbb{X}} = \mathbb{A}\mathbb{X} + \mathbb{B}\mathbb{R} \quad \ldots\ldots\ldots\ldots\ldots\ldots\ldots\ldots\ldots\ldots\ldots\ldots\ldots\ldots (3.17)$$

where the input vector $\mathbb{R} = [a \; i_1]^t$ ..... (3.18)

Transforming to the complex frequency (s) domain the above equations become

$$
\left.
\begin{aligned}
sX &= V \\
sV &= \frac{2L_o I_o^2}{Md^2} X - \frac{L_o I_o}{Md} I_3 + \frac{L_o I_o}{Md} I_5 + A \\
sI_3 &= \frac{I_o}{d} V - \frac{r_1}{L_o} I_3 + \frac{r_1}{L_o} I_1 \\
-sI_5 &= \frac{I_o}{d} V + \frac{r_1}{L_o} I_5 + \frac{r_1}{L_o} I_1
\end{aligned}
\right\} \quad \ldots\ldots\ldots\ldots\ldots\ldots (3.19)
$$

In correspondence with standard practice, all upper case variables denote the Laplace transform of the corresponding lower case time dependant variable.

It is evident from equations (3.19) that variables I_3 and I_5 are identical except for a difference in sign. By setting

$$I = I_3 = -I_5 \quad \ldots\ldots\ldots\ldots\ldots\ldots\ldots\ldots\ldots\ldots\ldots\ldots\ldots\ldots\ldots\ldots (3.20)$$

equations (3.19) reduce to a 3rd order system:

$$
s\begin{bmatrix} X \\ V \\ I \end{bmatrix} = \begin{bmatrix} \emptyset & 1 & \emptyset \\ \dfrac{2L_o I_o^2}{Md^2} & \emptyset & \dfrac{-2L_o I_o}{Md} \\ \emptyset & \dfrac{I_o}{d} & \dfrac{-r_1}{L_o} \end{bmatrix} \begin{bmatrix} X \\ V \\ I \end{bmatrix} + \begin{bmatrix} \emptyset & \emptyset \\ -1 & \emptyset \\ \emptyset & \dfrac{r_1}{L_o} \end{bmatrix} \begin{bmatrix} A \\ I_1 \end{bmatrix} \quad \ldots\ldots\ldots (3.21)
$$

or in vector-matrix notation

$$s\mathbf{X}_1 = \mathbf{A}_1 \mathbf{X}_1 + \mathbf{B}_1 \mathbf{R}_1 \quad \ldots\ldots\ldots\ldots\ldots\ldots\ldots\ldots\ldots\ldots\ldots\ldots\ldots\ldots (3.22)$$

where all the terms above are defined by eq.(3.21).

The characteristic equation of the system without feedback which is obtained by setting

$$|s\mathbf{I} - \mathbf{A}_1| = \emptyset \quad \ldots\ldots\ldots\ldots\ldots\ldots\ldots\ldots\ldots\ldots\ldots\ldots\ldots\ldots\ldots\ldots (3.23)$$

is found to be

$$s^3+(r_1/L_o)s^2-2r_1I_o^2/(Md^2)=\emptyset \quad \ldots\ldots (3.24)$$

The root locus of eq. (3.24) for variation in the term $K\triangleq 2r_1I_o^2/(Md^2)$ is constructed by rewriting eq. (3.24) as

$$1-K/[s^2(s+r_1/L_o)]=\emptyset \quad \ldots\ldots (3.25)$$

The root locus of eq. (3.25) is plotted in fig. 3.4 where it can be seen that the roots are real for values of K ranging from $\emptyset$ to $4r_1^3/(27L_o^3)$ at which point the two left half plane roots break away from the real axis at $s=-2r_1/(3L_o)$.

At the above breakaway point the relationship

$$I_o^2/(Md^2)=2r_1^2/(27L_o^3) \quad \ldots\ldots (3.26)$$

is valid.

The inherent instability of the system is demonstrated here once more by the 3rd root locus which starts at the origin and moves along the positive real axis for $K>\emptyset$.

A signal flow graph may be constructed directly from equations (3.21). A simpler and more useful one for obtaining a suitable feedback compensator is obtained, however, by transforming eq. (3.21) as follows:
Combine the 1st and 3rd equation of equations (3.21) to yield

$$I=(I_o/d)X+[r_1/(L_os)](I_1-I) \quad \ldots\ldots (3.27)$$

From equations (3.2) and (3.3) it can be shown that

$$I=I_1-E/r_1 \quad \ldots\ldots (3.28)$$

where E is the Laplace transform of the induced coil voltage e_1.

By defining $P=E/s$ $\ldots\ldots (3.29)$

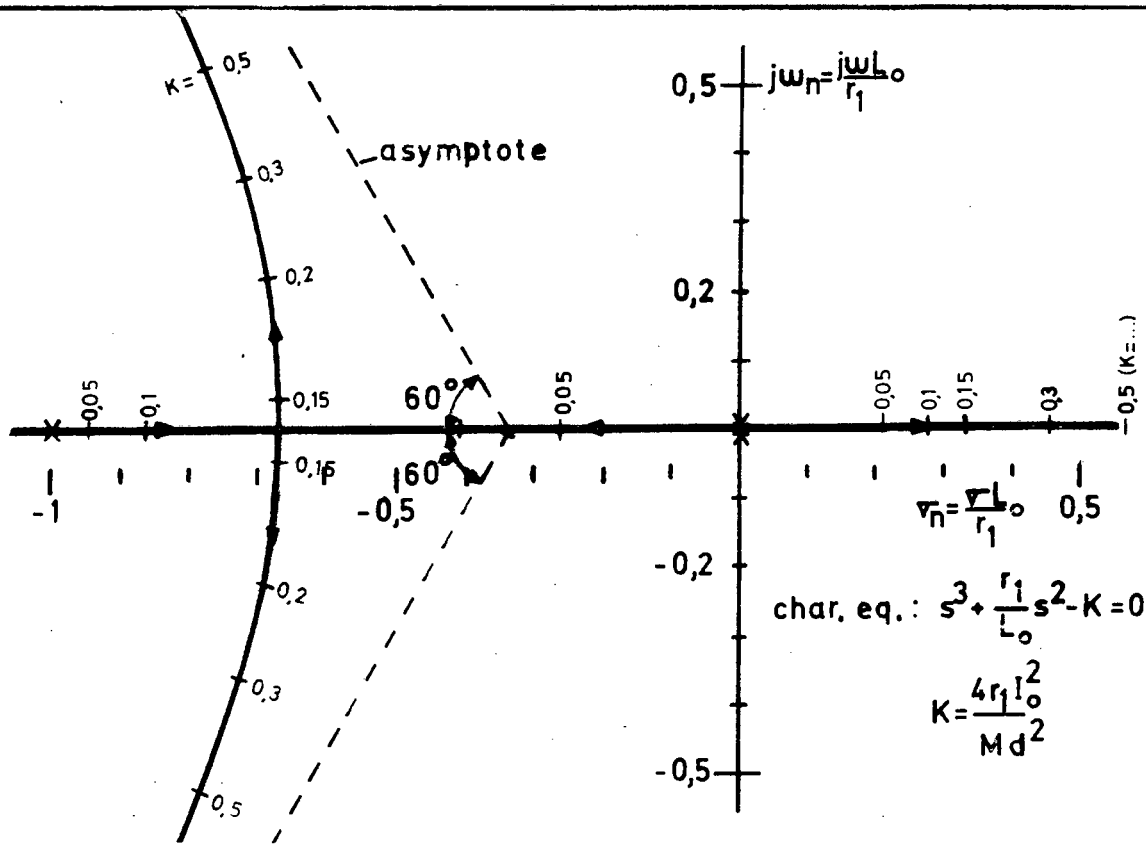

FIG. 3.4 ROOT LOCUS of LINEARISED BEARING without FEEDBACK

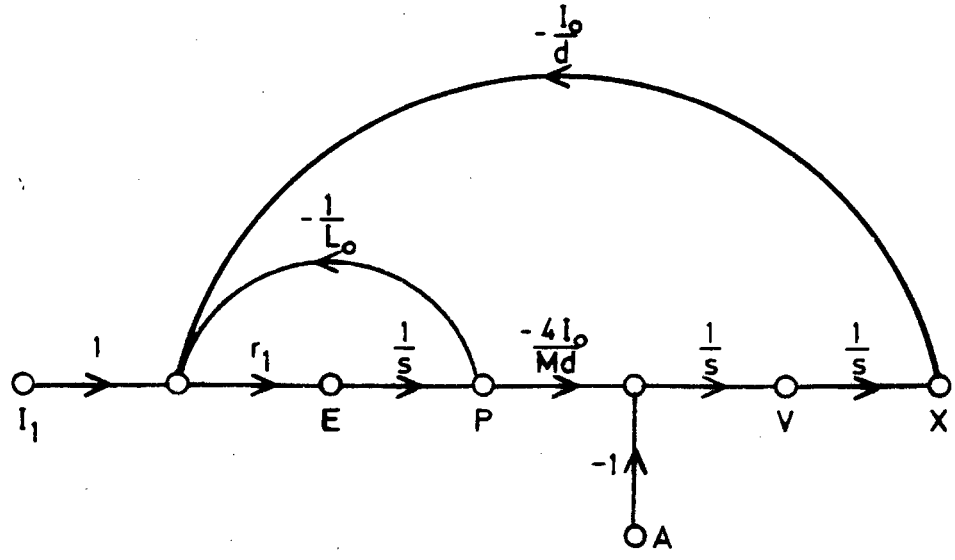

FIG.3.5 SIGNAL FLOW GRAPH of OPEN LOOP MAGNETIC BEARING

eq. (3.28) becomes

$$I=I_1-sP/r_1 \quad \text{.....(3.30)}$$

Replacing this value for I into eq. (3.27) and (3.21) provides a new set of state equations:

$$sX=V \quad \text{.....(3.31a)}$$
$$sV=-[2I_o/(Md)]P+A \quad \text{.....(3.31b)}$$
$$sP=E=-(r_1I_o/d)X-(r_1/L_o)P+r_1I_1 \quad \text{.....(3.31c)}$$

The new state variable p defined above is the time integral of e_1 and thus linearly related to the incremental flux change $\Delta\varphi$. This can be seen from eq. (3.7).

Equations (3.31) provide a more compact signal flow graph than eq. (3.21) with the output variable E forming an integral part thereof as shown in fig. 3.5.

This signal flow graph may now be used to determine the incremental stability of the system for various feedback strategies, and will be returned to later on in chapter 5.

CHAPTER 4

MODEL OF THE VOLTAGE DRIVEN MAGNETIC BEARING

Practical experience with two different current driven magnetic bearings, designed around the model derived in chapter 3, has proven them to be difficult to stabilise. A feedback loop was designed analytically, whereafter considerable trial and error adjustment of the feedback parameters was required before asymptotic stability could be obtained. After this the stability margins still left a lot to be desired. Usually the amount of damping was too low, or the settling times too long and the amount of loading the bearing could tolerate before breaking into oscillation far below the design value. One of the main contributing factors to the above problem is possibly the inverse square relationship between the magnetic force and the gap length as expressed by eq. (3.12). Details of the above investigation were reported by a co-worker [40] and thus will not be repeated here.

By driving the coil with a voltage source instead of a current source satisfactory results were obtained. The compensation network in this case had been designed from a Bode displacement vs. input voltage plot of the bearing. The procedure for this design will be described below.

Controlling the coil voltage amounts to controlling the time derivative of the magnetic flux. This, in effect, amounts to controlling the flux and consequently also the magnetic force between rotor and stator. The inverse square law mentioned above is thus eliminated because the magnetic force is no longer a function of gap length. Referring to the linear model in fig. 3.5 this technique amounts to removing the positive feedback loop which is formed partially by the branch $-I_o/d$ which couples the output back into the system. The gap length (ie x) still has an influence on the magnetising current. The only remaining nonlinearity which has to be contended with is the square law relationship between magnetic force and magnetic flux according to equations (3.10) and (3.11). Judging from the

practical experience gained with this technique it is just as effective as the technique used by Jayawant [24] for overcoming the same problem, but with the added advantage that no additional sensor (Hall element) has to be built into the gap for providing a flux control loop as was done by Jayawant.

This nonlinearity is handled analytically by means of describing function techniques which enable the designer to predict the performance of the the system for all signal levels. The limitation of the linear incremental model of the previous chapter which is only applicable to small signals is thus removed.

These arguments indicate that the above approach is much more powerful than that of the previous chapter.

This chapter will thus mainly be devoted to deriving the describing functions for the transfer of input voltage to magnetic force. Firstly, the case of the non-saturating core is considered, to be followed by the case where the core is being driven into saturation by the sinusoidal control voltage. Hereafter the simplifying assumption of an infinite mass stator is removed in order to obtain a model of the mechanical system which is closer to reality. An attempt will also be made to describe mathematically a severe mechanical resonance which was encountered in the rotor. Finally the theoretical Bode plot of position vs input voltage obtained from the models of this chapter are compared with experimentally measured results.

4.1 Describing Functions

4.1.1 Introduction:

From equation (3.7) the magnetic flux for any one of the two pole pairs may be written as

$$\varphi(t)=(1/n)\int_0^t e(\tau)d\tau+\Phi_0 \quad (W) \qquad (4.1)$$

where Φ_0 is the quiescent magnetic flux.

According to equations (3.10) and (3.11) the force between any two bearing elements

$$f=\varphi^2/(\mu_o A) \quad (N) \qquad (4.2)$$

can only be an attraction force. The coil currents thus have to be controlled in such a way that an increase of the current in one coil will coincide with an equal decrease in the current of the opposite coil. A further constraint is that neither of these currents will be allowed to change sign, as stated by eq. (3.2).

Referring to eq. (4.1) the above may be rephrased as follows:
Although the induced voltage e is allowed to make negative excursions, its time integral and thus $\varphi(t)$ will never be negative. In practice this is achieved by not actively driving e below zero, but only allowing it to go below zero in a freewheeling mode. This means that energy cannot be stored into but only extracted from the coil when $e<0$ and thus φ will never change sign. Circuitry for achieving this function is shown in fig. 4.1. The average (short term) coil voltage is determined by the mark-space ratio of the high frequency (20 kHz) chopper. This mark-space ratio is varied sinusoidally for alternate half cycles on alternate coils. During the "off" period of the chopper the coil voltage drops to -V (nominally) and will remain there until all the energy in the coil has been returned to the supply -V whereupon it will drop back to zero or until the chopper changes back to the "on" state which would cause e=+V. After the initial turn-on transient the quiescent current I_o has no influence on e.

4.1.2 Describing Function with Non-saturating Core:

When a sinusoidal signal

$$e_c=\hat{E}\sin\omega t \qquad (4.3)$$

is applied to the input of the power amplifier which drives

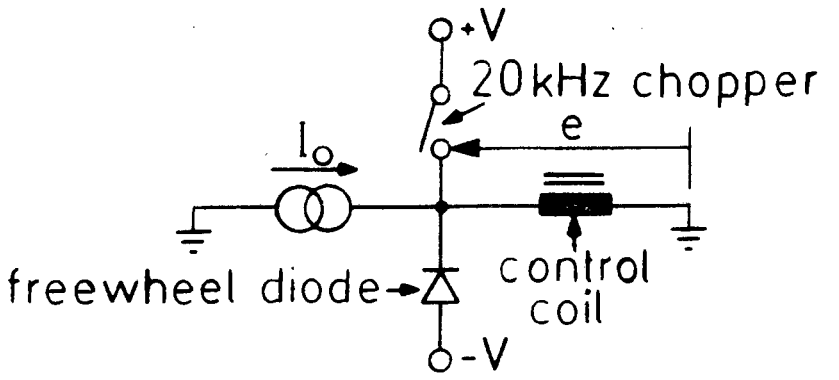

FIG. 4.1 VOLTAGE CONTROL of CONTROL COIL

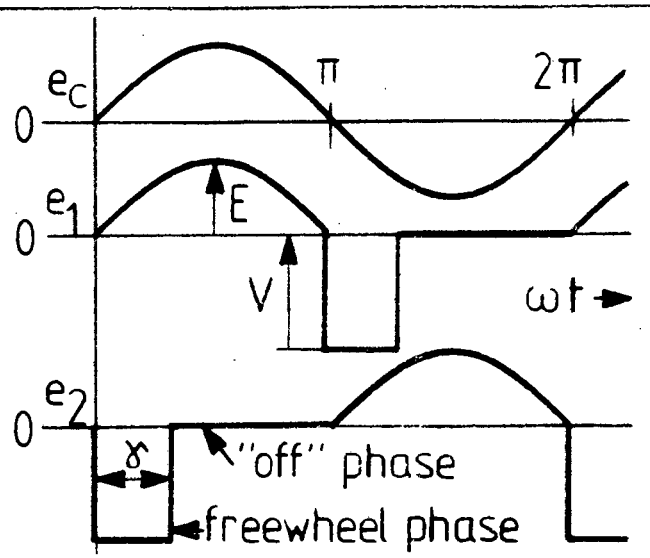

FIG. 4.2 VOLTAGE WAVE FORMS

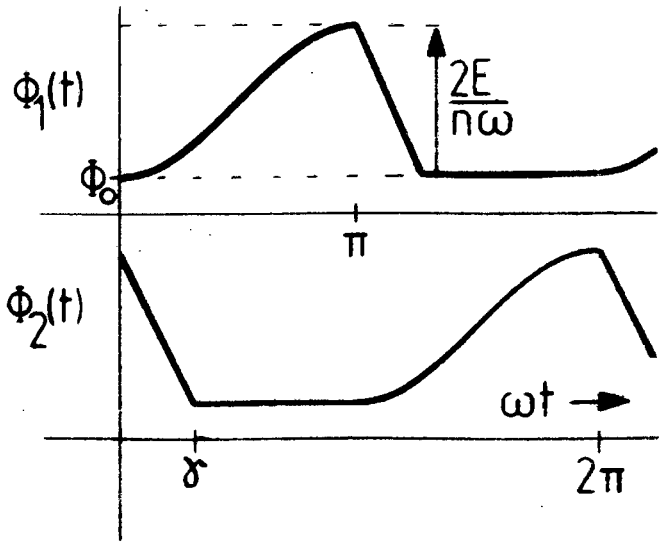

FIG. 4.3 MAGNETIC FLUX WAVEFORMS

the coils, alternate half cycles of this waveform are applied to coils no. 1 and 2 in turn. Assuming the power amplifier to have a voltage gain of 1 and a rolloff frequency far greater than any of the system frequencies which are of any importance, the average (ie average relative to the chopper frequency, but instantaneous relative to control loop frequencies) coil voltages are

$$e_1=\hat{E}\sin\omega t \text{ for } 2k\pi<\omega t<(2k+1)\pi$$
$$e_2=\hat{E}\sin(\omega t-\pi) \text{ for } (2k+1)\pi<\omega t<2(k+1)\pi \quad \ldots\ldots\ldots\ldots\ldots\ldots (4.4)$$

where $k=0,1,2..$etc.

Radial frequency ω is assumed to be well below the chopper frequency and the inductance of the coils large enough so that we only need to consider the average coil voltage as shown in fig. 4.2.

For steady state operation there is no buildup of energy in the coils, thus after the freewheeling phase, which follows each half sinusoid, the magnetic flux must return to its quiescent value Φ_o which is set up by the quiescent current I_o. From equations (4.1) and (4.2) we may write (see also fig. 4.2):

$$\int_0^{\pi}\hat{E}\sin\theta d\theta+\int_{\pi}^{\pi+\gamma}(-V)d\theta=0 \ldots\ldots\ldots\ldots\ldots\ldots\ldots\ldots\ldots\ldots (4.5)$$

and from this

$$\gamma=2\hat{E}/V \text{ (rad)} \ldots\ldots\ldots\ldots\ldots\ldots\ldots\ldots\ldots\ldots\ldots\ldots\ldots\ldots (4.6)$$

where γ is the freewheeling angle.

The waveform of the flux $\varphi_1(t)$ is shown in fig. 4.3.

During the "half sinusoid" phase, with no core saturation

$$\varphi_1(t)=(1/n)\int_0^t\hat{E}\sin\omega\tau d\tau+\Phi_o=(\hat{E}/n\omega)(1-\cos\omega t)+\Phi_o, \ldots\ldots\ldots (4.7)$$

during the freewheeling phase

$$\varphi_1(t)=2\hat{E}/(\omega n)+\Phi_o-(V/n)(t-\pi/\omega)$$
$$\text{for } \pi/\omega<t<(\pi+\gamma)/\omega \quad \ldots\ldots(4.8)$$

and during the "off" phase

$$\varphi_1(t)=\Phi_o \text{ for } (\pi+\gamma)/\omega<t<2\pi \quad \ldots\ldots(4.9)$$

For coil no. 2 the waveform of $\varphi_2(t)$ is identical except for a time delay of π/ω seconds.

The total force on the rotor in the negative x-direction (from eq. (4.2))

$$f_T(t)=(1/\mu_o A)[\varphi_1^2(t)-\varphi_2^2(t)] \text{ (N)} \quad \ldots\ldots(4.10)$$

thus

$$f_T(t)=\begin{cases} \frac{1}{\mu_o A}\left[\left(\frac{\hat{E}}{\omega n}(1-\cos\omega t)+\Phi_o\right)^2-\left(\frac{2\hat{E}}{\omega n}+\Phi_o-\frac{V}{n}(t)\right)^2\right] & \left|0<t<\frac{\gamma}{\omega}\right. \\ \frac{1}{\mu_o A}\left[\left(\frac{\hat{E}}{\omega n}(1-\cos\omega t)+\Phi_o\right)^2-\Phi_o^2\right] & \left|\frac{\gamma}{\omega}<t<\frac{\pi}{\omega}\right. \\ \frac{1}{\mu_o A}\left[\left(\frac{2\hat{E}}{\omega n}+\Phi_o-\frac{V}{n}(t-\frac{\pi}{\omega})\right)^2-\left(\frac{\hat{E}}{\omega n}(1+\cos\omega t)+\Phi_o\right)^2\right] & \left|\frac{\pi}{\omega}<t<\pi+\frac{\gamma}{\omega}\right. \\ \frac{1}{\mu_o A}\left[\Phi_o^2-\left(\frac{\hat{E}}{\omega n}(1+\cos\omega t)+\Phi_o\right)^2\right] & \left|\frac{\pi+\gamma}{\omega}<t<\frac{2\pi}{\omega}\right. \end{cases} \quad \ldots(4.11)$$

The describing function is found from the fundamental component of this periodic force acting on the rotor.

Due to the symmetry of the system under consideration, the forces f_1 and f_2 are equal. The signals e_1 and e_2 generating f_1 and f_2 are shifted in phase by π radians relative to each other but f_1 and f_2 act upon the rotor in opposite directions. The two fundamental components will thus be in phase with each other. It is thus only necessary to determine one of these components, say C_1 of f_1. The fundamental component of f_T will then be $2C_1$.

If the fundamental component of f_1 is expressed as

$$c_1(t)=A_1\cos\omega t+B_1\sin\omega t \quad \ldots\ldots(4.12)$$

the Fourier components A_1 and B_1 are found to be

$$A_1=\frac{-e}{\pi\mu_o A}\left\{(\Phi_o+e)\pi+4v+\frac{2v\Phi_o}{e}(1-\cos\gamma)-\frac{2v^2}{e}\sin\gamma\right\} \text{ and}$$

$$B_1=\frac{-e}{\pi\mu_o A}\left\{\frac{4e}{3}-\frac{2v^2}{e}(1-\cos\gamma)-\frac{2v\Phi_o}{e}\sin\gamma\right\} \quad \ldots(4.13)$$

where $e=\frac{E}{n\omega}$ and $v=\frac{V}{n\omega}$

These expressions for A_1 and B_1 are derived in appendix 4A.

The amplitude of one half of the fundamental component of f_T is

$$C_1=(A_1^2+B_1^2)^{\frac{1}{2}} \quad \ldots\ldots(4.14)$$

The phase shift of this fundamental component relative to the input sinal e_c (eq. (4.3)) is

$$\psi=\tan^{-1}(A_1/B_1) \quad \ldots\ldots(4.15)$$

The describing function is thus

$$N(E,\omega)=|2C_1/E|\mathrm{Arg}(\psi) \quad \ldots\ldots(4.16)$$

4.1.3 Describing Function with Saturating Core

Since the coils are voltage driven, conditions where the magnetic flux $\varphi(t)$ will tend to exceed the saturation value of Φ_m (Weber) for the core material could easily arise, particularly at low frequencies. In the idealised case, ie with a true voltage source and zero coil resistance, the magnetic flux will simply be forced to any required value to satisfy eq. (4.1), and when $\varphi(t)$ exceeds Φ_m the magnetising current can be expected to reach very high

values.

In any practical system current limiting will be incorporated to protect the output stage of the power amplifier and the driving coils from overheating, thus essentially limiting $\varphi(t)$ to Φ_m.

In order to simplify the analysis it is assumed that, with the half sinusoidal voltage of the previous section being applied to the driving coil, $\varphi(t)$ will initially rise smoothly according to eq. (4.1) and then stop rising abruptly the moment Φ_m is reached. This progress of φ_m is shown in fig. 4.4.

The Fourier coefficients for the fundamental frequency of the force wave arising from this flux waveform are the following (for their derivation see appendix 4C):

$$A_1' = \frac{1}{\pi\mu_o A}\left[-e(e+\Phi_o)\beta + \left(\frac{7}{4}e^2 + 2e\Phi_o + \Phi_o^2 - \Phi_m^2\right)\sin\beta - \frac{e+e\Phi_o}{2}\sin 2\beta + \frac{e^2}{12}\sin 3\beta + 2v^2\sin\gamma' + 2\Phi_o v\cos\gamma' - 2\Phi_m v\right]$$

and (4.17)

$$B_1' = \frac{1}{\pi\mu_o A}\left[\frac{e^2}{3} + e\Phi_o + (\Phi_m^2 - (e+\Phi_o)^2)\cos\beta + e(e+\Phi_o)\cos^2\beta - \frac{e^2}{2}\cos^3\beta + 2v^2(1-\cos\gamma') + 2\Phi_o v\sin\gamma'\right]$$

where $\beta = \cos^{-1}\{1-(n\omega/\dot{E})(\Phi_m-\Phi_o)\}$ for $2\dot{E}/(n\omega)+\Phi_o > \Phi_m$
and $\gamma' = (\Phi_m-\Phi_o)/v$

The describing function for the saturating core $N_s(\dot{E},\omega)$ is found by using the above coefficients A_1' and B_1' in equations (4.14) and (4.16).

At the transition from the non-saturating to the saturating case, the angle $\beta=\pi$ and $\Phi_m=2e+\Phi_o$. Replacing these values into equations (4.17) reduces them to equations (4.13).

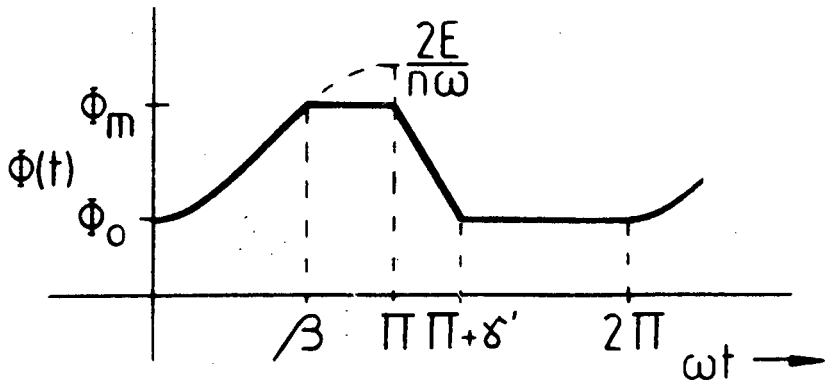

FIG. 4.4 FLUX WAVE with CORE SATURATION

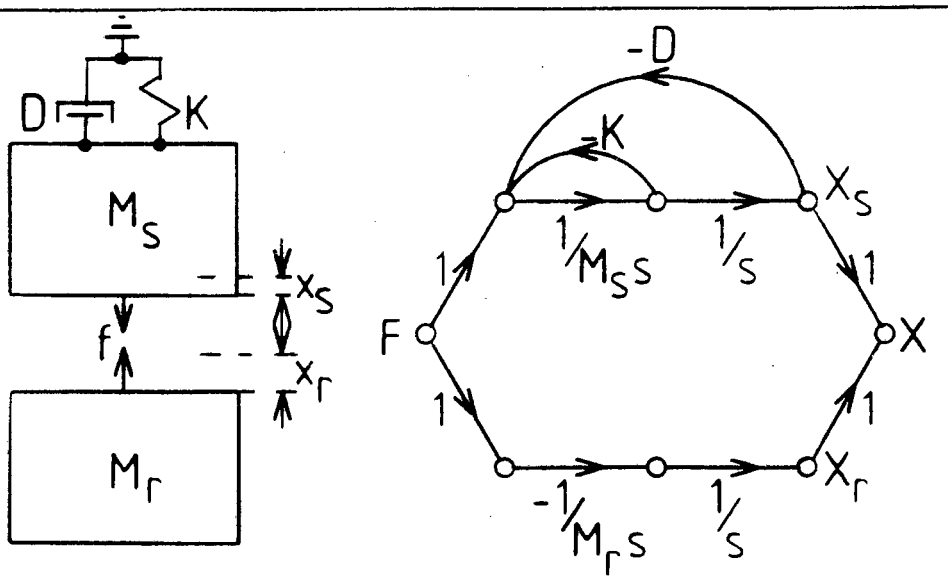

FIG. 4.5 MECHANICAL SYSTEM

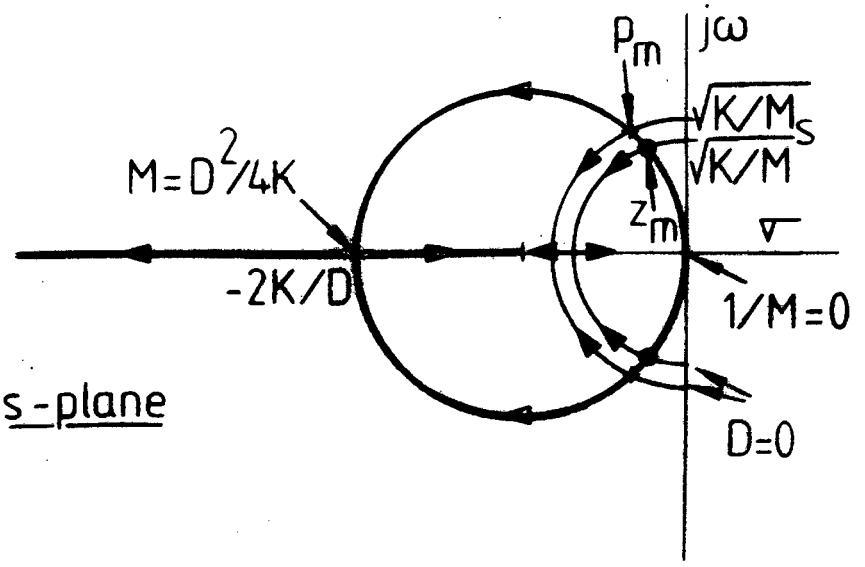

FIG. 4.6 LOCII of MECHANICAL POLES and ZEROS

4.2 The Mechanical System with Finite Mass Stator

In all but those systems with very small rotors it is an oversimplification to assume the mass of the stator to be infinite. In a flywheel system, which is intended for mobile applications, the stator mass will usually only be a small fraction of the rotor mass and the stator will usually also be suspended on flexible mountings. The dynamics of the stator will thus have a marked influence on the system performance.

In its simplest form the rotor-stator system is as presented in fig. 4.5. The following dynamical equations apply to this system:

$$\left.\begin{aligned} M_s s^2 X_s + D s X_s + K X_s &= F \\ M_r s^2 X_r &= -F \end{aligned}\right| \quad \ldots\ldots\ldots\ldots\ldots\ldots\ldots\ldots\ldots\ldots (4.18)$$

where the subscripts r and s refer to the rotor and stator respectively.
X is the transform of the displacement x from the neutral position,
F is the transform of the attraction force f,
M is the mass,
D is the damping constant of the suspension and
K is the stiffness of the suspension.
In practice the relative displacement between rotor and stator is usually measured as

$$X = X_r - X_s \quad \ldots\ldots\ldots\ldots\ldots\ldots\ldots\ldots\ldots\ldots\ldots\ldots\ldots\ldots\ldots\ldots (4.19)$$

From the above equations we obtain the transfer function for the mechanical system, relating position to force

$$G_m(s) = \frac{X}{F} = \frac{-\left(s^2 + \frac{Ds}{M} + \frac{K}{M}\right)}{M_e s^2 \left(s^2 + \frac{Ds}{M_s} + \frac{K}{M_s}\right)} \quad \ldots\ldots\ldots\ldots\ldots\ldots\ldots\ldots\ldots\ldots (4.20)$$

which also may be written as

$$G_m(s)=\frac{-(s-z_{m1})(s-z_{m2})}{M_e s^2 (s-p_{m1})(s-p_{m2})} \qquad \ldots\ldots(4.21)$$

where

$$M=M_r+M_s,\quad M_e=\frac{M_r M_s}{M_r+M_s},$$

$$z_{m1},z_{m2}=-\frac{D}{2M}\pm\left[\frac{D^2}{4M_s^2}-\frac{K}{M}\right]^{1/2} \text{ and} \qquad \ldots\ldots(4.22)$$

$$p_{m1},p_{m2}=-\frac{D}{2M_s}\pm\left[\frac{D^2}{4M_s^2}-\frac{K}{M_s}\right]^{1/2}.$$

The locii for the above poles and zeros for $0<D<(KM_s)^{1/2}$ and $0<D>(KM)^{1/2}$ are concentric circles of radius $(K/M_s)^{1/2}$ and $(K/M)^{1/2}$ respectively, with centres at the origin of the complex s-plane. Such a locus is obtained in the case of the zeroes z_{m1} and z_{m2} by setting

$$s^2+\frac{D}{M}s+\frac{K}{M}=0 \qquad \ldots\ldots(4.23)$$

and rewriting it as

$$1+\frac{D}{M}\cdot\frac{s}{s^2+\frac{K}{M}}=0 \qquad \ldots\ldots(4.24)$$

Standard root locus construction techniques provide the abovementioned circles (see fig. 4.6).

By rewriting eq.(4.23) as

$$1+\frac{D}{M}\cdot\frac{s+\frac{K}{D}}{s^2}=0 \qquad \ldots\ldots(4.25)$$

a different circular locus is found with radius K/D centred at s=-K/D for variable M with K and D constant.

The intersections of the latter circle with the former two provide the locations of the mechanical poles and zeros as

depicted in fig. 4.6. It can be seen here that for all complex z_m and p_m, p_m will be further removed from the origin and thus at a higher ω but also with a higher "damping ratio" than z_m.

For very large M_s, $M_e \doteq M_r$, the poles and zeros move very close together and their effects tend to cancel each other, reducing the transfer function to that of the infinite mass stator case:

$$G_m(s) = -1/(M_r s^2) \qquad (4.26)$$

4.3 Total Transfer Function of a Voltage Driven System

Combining the results of the previous two sections provides the sytem transfer function which, for $s=j\omega$, is

$$G_s(j\omega) = N_s(\hat{E},\omega) \cdot \frac{(j\omega - z_{m1})(j\omega - z_{m2})}{M_e \omega^2 (j\omega - p_{m1})(j\omega - p_{m2})} \qquad (4.27)$$

It is important to know what the small signal response of $G_s(s)$ is. For very small input voltage amplitudes $\hat{E}$, equations (4.13) reduce to

$$A_1 = \frac{-\hat{E}\Phi_o}{\mu_o An\omega} \quad \text{and} \quad B_1 = \frac{4\hat{E}\Phi_o}{\pi \mu_o An\omega} \qquad (4.28)$$

The describing function now becomes

$$N(\hat{E},\omega) = \frac{N\lfloor\theta_o}{\omega} = \frac{2\Phi_o}{\mu_o An\omega}\left(1+\left(\frac{4}{\pi}\right)^2\right)^{1/2} \lfloor \tan^{-1}\frac{\pi}{4} \qquad (4.29)$$

$$= \frac{2{,}577\times 10^{6} B_o}{n\omega} \lfloor -38{,}146^{\circ} \qquad \text{where } B_o \triangleq \frac{\Phi_o}{A}$$

It can be seen from eq. (4.29) that $N(\hat{E},\omega)$ will contribute a -20dB/decade slope to the Bode amplitude plot of the system transfer function. This slope is not coupled to a phase shift of $-\pi/2$ radians as the case would be with a

linear system. Instead, the phase shift is -38,146° (Ø,6658 rad.), which leads to a greater phase margin when designing a compensator along conventional (linear) lines.

4.4 Transfer Function of a Practical System

Only after stabilising a magnetic bearing by means of the correct feedback compensation network, as will be described fully in the next chapter, can the transfer function be measured. This is done by injecting an external sinewave signal into the feedback loop and then comparing the output voltage from the position transducers V_x to the input voltage to the power amplifier V_{in} at various frequencies.

A Bode amplitude plot of one of the experimental bearings developed for this investigation is presented in fig. 4.7.

The effects of the mechanical poles and zeros are very pronounced as can be seen by the "kink" in the general -6ØdB/decade trend of this curve. This curve displays a very good correspondence to the theoretical curve of $G_m(j\omega)$, obtained from eq. (4.2Ø) or (4.21), particularly for frequencies above 2ØØ r/s. The relevant parameters for this bearing were the following:

Table 4.1 **EXPERIMENTAL BEARING PARAMETERS**

Rotor mass	M_r=Ø,7	kg
Stator mass	M_s=3,147	kg
Stator damping constant	D=5Ø	N.s/m
Stator mounting spring constant	K=2,4x10^5	N/m
Mechanical zeros:	$z_{m1,2}$=6,51+/-j249,9	rad/s
Mechanical poles:	$p_{m1,2}$=7,96+/-j276	rad/s
MAXIMUM BEARING LOAD: 3Ø N (approx.) (3 kg)		

The deviation at low frequencies is most likely due to the copper resistance of the coils which was not taken into account when deriving $G_m(s)$ above.

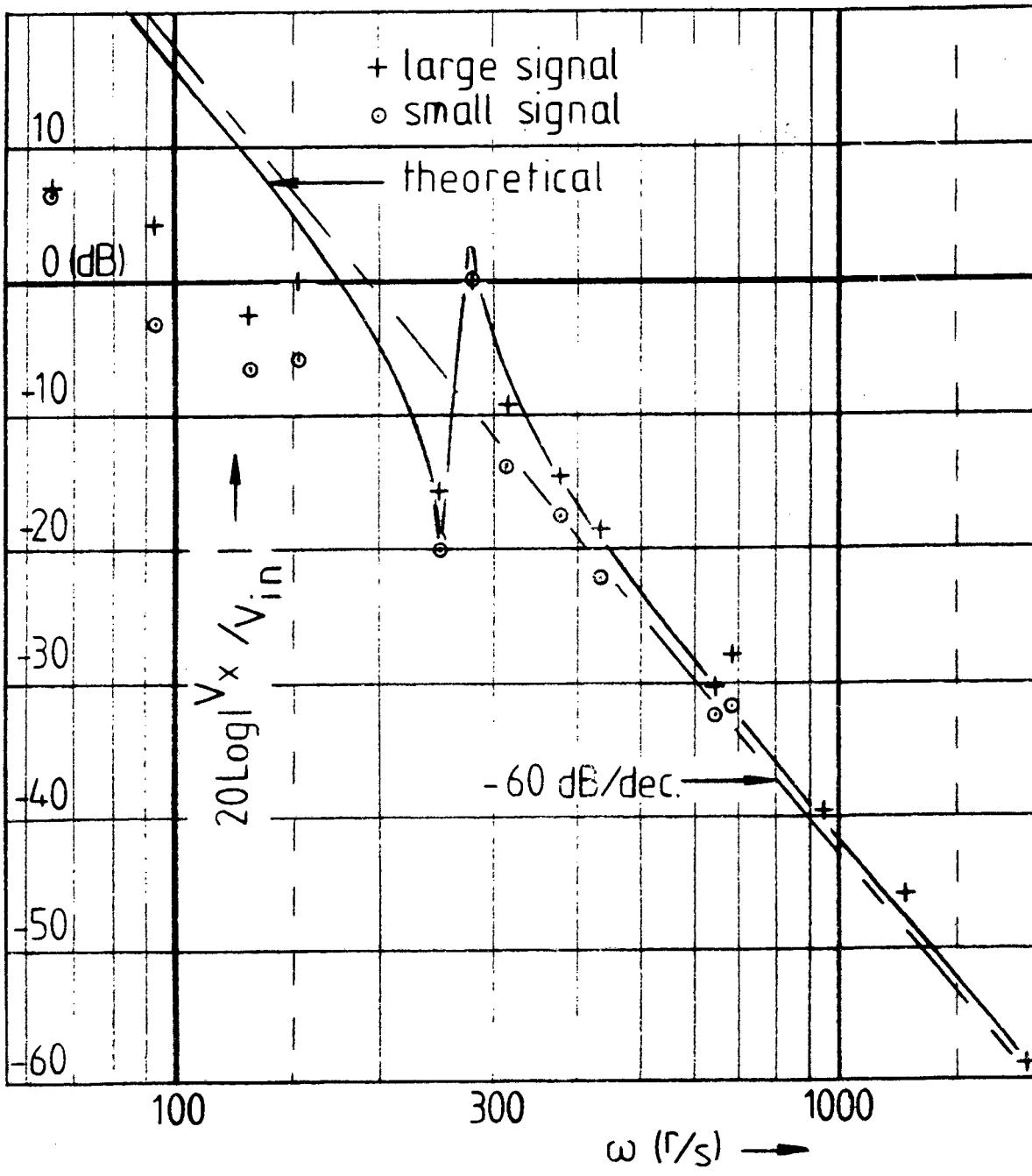

FIG.4.7 VOLYAGE DRIVEN BEARING TRANSFER FUNCTION

A smaller resonance "kink" was observed at approximately 69Ø rad/s which was due to a different resonance mode of the stator assembly. A very sharp resonance peak was also observed at ω_o=5812 rad/s which was clearly due to mechanical resonance of the rotor since it could be felt distinctly by touching the rotor, whereas it was barely noticeable when touching any other part of the bearing. Furthermore it could be dampened out either by gripping the stationary rotor or by wrapping a short length of solder wire around the drive quill at the base of the rotor. This rotor resonance requires special attention since both of the above damping procedures are impractical for high speed operation.

4.4.1 Rotor Resonance

The stator resonance "kink" in the transfer function of the mechanical system described above was characterised by a complex pole pair in close proximity to a complex zero pair. An attempt will now be made to characterise the observed rotor resonance peak at 5812 rad/s.

It must be appreciated that this resonance was peculiar to the specific rotor used in the experimental bearing and in a practical flywheel system it may not exist at all. In this case the rotor comprised a solid aluminium shaft with a steel ring shrunk over one end to form the magnetic bearing rotor pole. This rotor thus formed a very lightly damped resonator which was manifested by the abovementioned peak in the transfer function and by the deafening but pure, high pitched tone which emanated from the rotor before countermeasures could be taken!

In the above case the position transducer was an optical source and sensor assembly. The light beam incident upon the sensor was partially interrupted by a thin disc mounted on the rotor (see chapter 1, section 1.6). The output signal obtained was so low in the vicinity of the rotor resonance that the curve shape could not be reliably determined. The amplitude curve nevertheless appeared to

fall off steadily, with increasing frequency, at 60 dB/decade on either side of ω_o and the resonance itself could probably be represented by a single sharp peak. The top of this peak could be measured accurately because of its height, rising 53,5 dB above the general trend. This corresponds to an amplification of 473,15.

The curve shape described here may be represented by the transfer function

$$G_r(s)=\frac{(s-z_r)(s-z_r^*)}{(s-p_r)(s-p_r^*)} \qquad \text{.....(4.30)}$$

which has to be "cascaded into" the "system" of eq. (4.27).

z_r^* And p_r^* above are the complex conjugates of z_r and p_r respectively which both lie on a circle, centred at the origin of the complex s-plane, with radius ω_o. Writing

$$z_r=m_6+jm_7 \text{ and } p_r=m_8+jm_9 \qquad \text{.....(4.31)}$$

the above circular location condition is expressed as

$$m_6^2+m_7^2=m_8^2+m_9^2=\omega_o^2 \qquad \text{.....(4.32)}$$

Equations (4.30) through (4.32) produce:

$$G_r(j\omega)=\left[\frac{(\omega_o^2+\omega^2)-4\omega^2 m_7^2}{(\omega_o^2+\omega^2)-4\omega^2 m_9^2}\right]^{1/2} \angle\theta_r \qquad \text{.....(4.33)}$$

from which

$$G_r(j\omega_o)=\left[\frac{\omega_o^2-m_7^2}{\omega_o^2-m_9^2}\right]^{1/2} \angle\phi^\circ=\frac{m_6}{m_8}\angle\phi^\circ \qquad \text{.....(4.34)}$$

where

$$\theta_r = \tan^{-1}\left(-\frac{\omega-m_7}{m_6}\right)+\tan^{-1}\left(-\frac{\omega+m_7}{m_6}\right)-\tan^{-1}\left(-\frac{\omega-m_9}{m_8}\right)-\tan^{-1}\left(-\frac{\omega+m_9}{m_8}\right) \quad \text{.....(4.35)}$$

The -3dB point of $G_r(j\omega)$ is where

$$\omega \doteq \omega_o {}^{+}/_{-} m_8 \quad \text{.....(4.36)}$$

Thus the bandwidth of this resonance peak $B_{Gr}=-2m_8$ (m_8 is negative) is easily determined experimentally and was found to be 12,5 rad/s. The parameters for the rotor resonance are thus:

Table 4.2 **ROTOR RESONANCE PARAMETERS**

resonant frequency	$\omega_o=5812$	rad/s
amplitude of resonance peak	$\lvert G(j\omega_o)\rvert=473,15$	
bandwidth of resonance peak	$B_{Gr}=12,5$	rad/s
real part of zeros	$m_6=-2957,2$	rad/s
imaginary part of zeros	$m_7=+5003,4$	rad/s
real part of poles	$m_8=-6,25$	rad/s
imaginary part of poles	$m_9=+5811,99$	rad/s

The total system transfer function now becomes

$$G(s)=G_s(s)G_r(s) \quad \text{.....(4.37)}$$

where G_s and G_r are obtained from equations (4.27) and (4.33) respectively.

Bode amplitude plots of G(s) are presented in fig. 4.8 for various flux densities B_o and input voltage amplitudes E. In order to compare these curves with experimental data $G(j\omega)$ was multiplied by an additional factor of 10^4, which represents the amplification of the position transducer in Volts/meter. The dotted curve sections in fig. 4.8 are

those sections of the transfer function where core saturation occurs. No saturation is experienced along the solid portions of these curves.

Comparing figures 4.8(a) through (c) indicates that the greatest variation in gain, due to variation in $\bar{E}$, occurs with B_o=Ø, whereas this variation is very small with B_o=Ø,55 Tesla. Due to magnetic remanence in the core material the situation of fig. 4.8(a) may never be encountered in practice. The curve of fig. 4.8(b), where B_o=Ø,ØØ55 Tesla shows a close correspondence to the experimentally measured data.

Core saturation on the low frequency side causes a smaller roll-off than the 6Ø dB/decade which is expected for the linear case. This may partially explain the deviation from the -6ØdB/decade trend for frequencies below 2ØØ rad/s. As stated previously the copper resistance of the coil r_{Cu} probably accounts for the rest of the deviation.

4.5 Conclusion

Comparing the theoretical and experimental results it appears that the majority of the physical effects present in the experimental system are taken into account in the transfer function of the voltage driven magnetic bearing which was derived in this chapter. This is confirmed by the general correspondence that exists between the theoretical and experimental Bode plots of figs 4.7 and 4.8. In practice the total amount by which the curves shift with amplitude variation is restricted by the magnetic remanence of the core material. Even where the latter two curves do not agree quantitatively, they provide sufficient insight into the behavior of the nonlinear system to enable the designer to go about correcting any malfunction of a magnetic bearing in an intelligent and systematic manner. This model of the bearing, represented by G(s) (eq. (4.37)), will be used in the next chapter to investigate various approaches in the design of a suitable feedback compensation network.

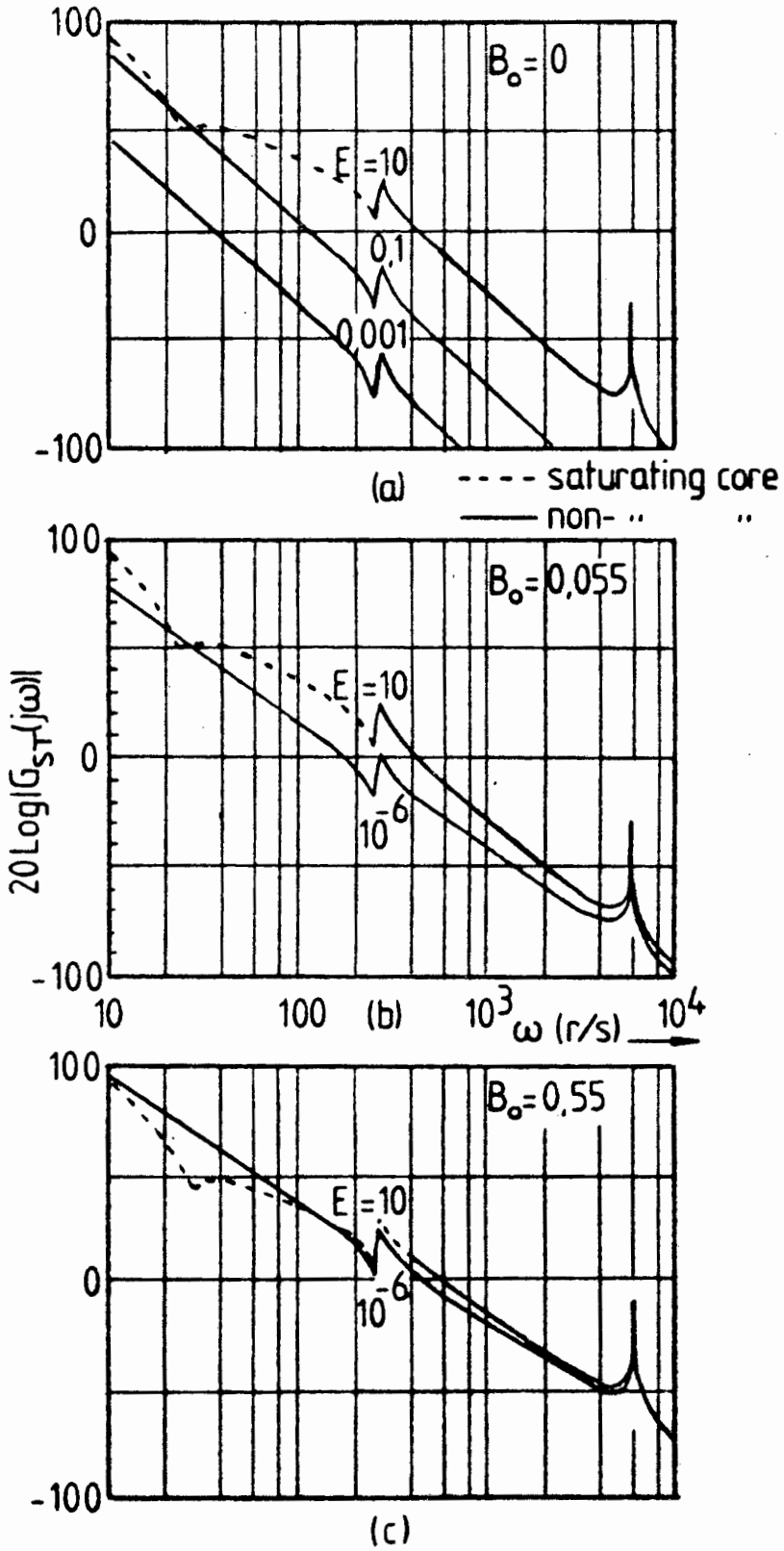

FIG.4.8 BODE-AMPLITUDE PLOTS for TOTAL SYSTEM TRANSFER FUNCTION $G(j\omega)$

CHAPTER 5

FEEDBACK CONTROL AND COMPENSATION OF SINGLE MAGNETIC BEARINGS

Armed with the system models that were developed in chapters 3 and 4, it is now possible to develop a feedback system that will ensure asymptotic stability of the rotor about a neutral point. This neutral point, measured relative to the stator, is chosen so that there exists no mechanical contact between rotor and stator. The feedback system should ensure a suitable dynamic response to meet the performance specifications dictated by the bearing application. Ideally such a magnetically suspended system should be critically damped and be capable of responding fast enough to any disturbance which may be expected during normal operation to prevent rotor stator contact. In mobile applications, the most commonly encountered disturbance would be an acceleration with an expected maximum value of approximately 20 m/s^2 .

For stationary systems, with rigidly mounted stators, the most severe mechanical disturbances will be of seismic origin such as earth tremors and quakes. Thus, the "worst case" condition, for which the bearing has to be designed, will be dictated by the seismic data for the envisaged site and by economic considerations.

Keeping the above in mind it will be appreciated from the above that "normal expected disturbances" will be a matter of definition. It may be assumed that so-called mechanical "touch down" bearings will be built into the system to accommodate any "abnormal" excursion of the rotor from the neutral position, arising from "abnormal" disturbances.

Various control strategies will now be investigated. As stated in chapter 4 significantly better results were obtained with voltage control than with current control and consequently only voltage control will be considered.

Firstly standard Bode-diagram compensation techniques will

be applied to the small signal model of the bearing which was derived in section 4.5. After this has been successfully done the feedback compensation thus obtained will be applied to the large signal (describing function) model and tested for stability.

Hereafter state variable feedback, by means of a state observer, will be investigated. It will be shown that for this application the state observer concept may be reduced to a simpler feedback compensator equivalent to that obtained by means of the Bode-diagrams.

Lastly the possibility of achieving stability without feedback from sensors will be considered for bearings with nonzero quiescent current, where it will be shown that the system is completely observable from the coil voltage-current relationship and that the feedback compensator problem may be reduced to a type of impedance matching problem.

5.1 Bode-Diagram Compensator Design

The compensator transfer function H(s) has to be chosen so that when the loop gain G(s)H(s) has dropped to 1, the phase shift should be below 180°, but preferably below 135°, to ensure a good phase margin. Where $20\log|G(j\omega)H(j\omega)|=0$ the slope of $20\log|G(j\omega)H(j\omega)|$ should be in the vicinity of -20 dB/decade, or stated differently once more, where $20\log|G(j\omega)|=20\log|1/H(j\omega)|$ the difference in slope between $20\log|G(j\omega)|$ and $20\log|1/H(j\omega)|$ should be approximately 20dB/decade.

Thus, if the Bode-amplitude plot of $20\log|1/H(j\omega)|$ should cross that of $20\log|G(j\omega)|$ where the latter has a slope of -60 dB/decade, the slope of $20\log|1/H(j\omega)|$ should preferable be -40 dB/decade, as shown in fig. 5.1.

$H(j\omega)$ is chosen so that this crossing will occur along a section of the $G(j\omega)$ curve which is "well behaved" such as beyond the mechanical resonance "kink" shown in fig. 5.1. This will allow for a considerable variation in allowable

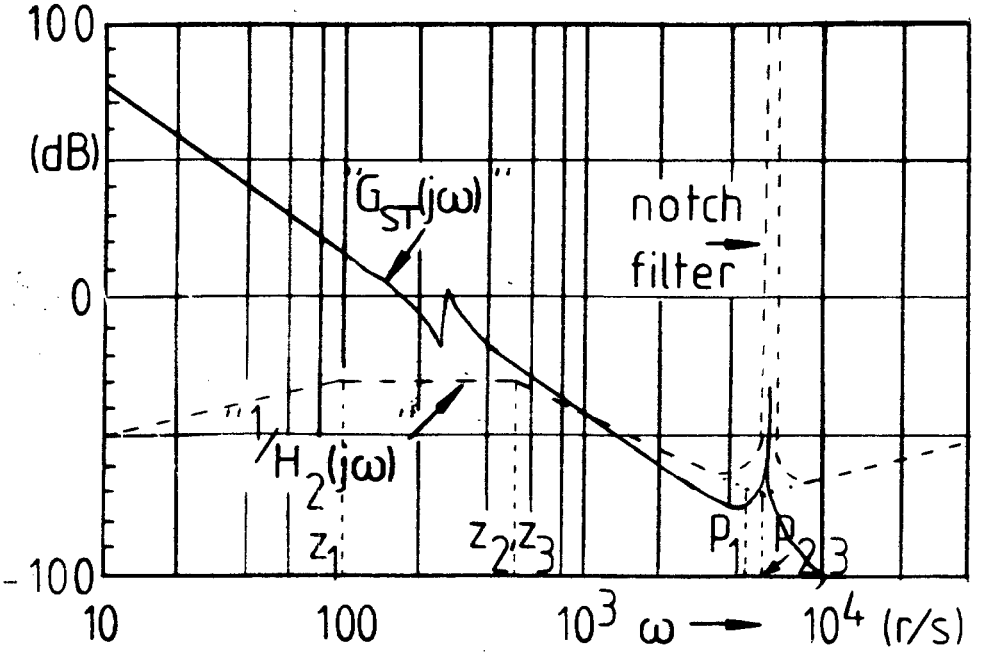

FIG. 5.1 GRAPHICAL COMPENSATOR DESIGN

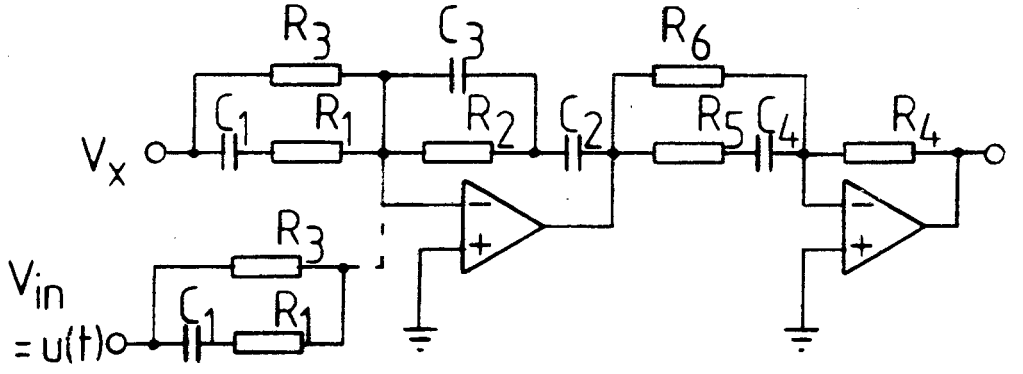

FIG. 5.2 COMPENSATOR

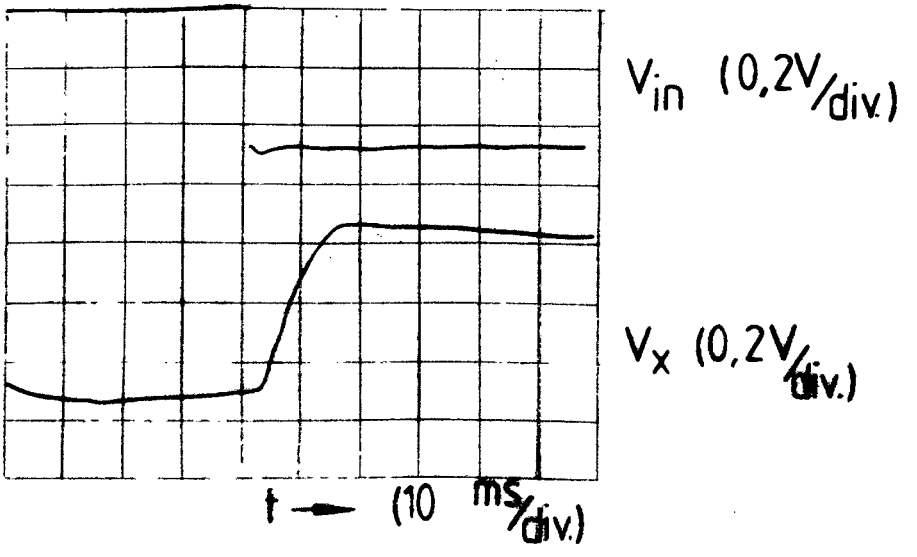

FIG. 5.2A STEP RESPONSE with COMPENSATOR

gain in both G(jω) and H(jω).

In the practical system investigated it was necessary to cause the H(jω) curve to flatten out on the low frequency side to avoid the suspension resonance "kink". It was found, furthermore, in an effort to improve the settling time of the system, that the crossing point could not be shifted to a much higher frequency, due to the rotor resonance peak in G(jω) at 925 Hz (5812r/s). An additional notch filter was incorporated into the feedback loop to maintain 1/H(jω) above this resonance peak (see appendix 5A).

Ignoring the notch filter and the curve shape beyond it for the moment, the following elementary transfer function for the compensator in the vicinity of the crossover point is derived:

$$H(s)=K_c(s-z_2)(s-z_3) \quad \ldots\ldots(5.1)$$

where K_c is positive and real.

In order to reduce noise sensitivity and make H(s) realisable, 3 poles, p_1, p_2 and p_3, have to be added at high frequencies giving:

$$H_1(s)=K_c(s-z_2)(s-z_3)/[(s-p_1)(s-p_2)(s-p_3)] \quad \ldots\ldots(5.2)$$

where all z and p are real and negative.

The 3 latter poles provide H(s) with a roll-off of 20 dB/decade at high frequencies. In order to obtain a zero steady state error integral feedback may be added to H(s) producing a +20 dB/decade slope in $20\log|1/H(j\omega)|$ at low frequencies. To retain the correct shape near the crossover frequency an additional zero at $s=z_1$ is added (see fig. 5.1).

The feedback compensation now becomes:

$$H_2(s)=K_c(s-z_1)(s-z_2)(s-z_3)/[s(s-p_1)(s-p_2)(s-p_3)]\ldots\ldots(5.3)$$

The circuit shown in fig. 5.2 was used to synthesise $H_2(s)$ where the component values shown below render the following parameters for H(s):

Table 5.1

Compensator Parameters:

K_c	$=1,723\times10^7$
z_1	$=-96,3$ r/s
z_2	$=-495$ r/s
z_3	$=-496$ r/s
p_1	$=-4630$ r/s
p_2	$=-5447$ r/s
p_3	$=-5447$ r/s

Component values:

R_1	$=270\ \Omega$	R_6	$=2k7\ \Omega$
R_2	$=12\ k\Omega$	C_1	$=0,68\ \mu F$
R_3	$=15\ k\Omega$	C_2	$=0,15\ \mu F$
R_4	$=18\ k\Omega$	C_3	$=18\ nF$
R_5	$=270\ \Omega$	C_4	$=0,68\ \mu F$

In terms of component values we may write: $H_2(s)=$

$$\frac{(R_1+R_3)(C_2+C_3)R_4(R_5+R_6)\left[s+\frac{1}{(R_1+R_3)C_1}\right]\left[s+\frac{1}{(C_2+C_3)R_2}\right]\left[s+\frac{1}{(R_5+R_6)C_4}\right]}{(R_1R_3R_5R_6C_2C_3)s\left[s+\frac{1}{R_1C_1}\right]\left[s+\frac{1}{R_2C_3}\right]\left[s+\frac{1}{R_5C_4}\right]}\ldots\ldots(5.4)$$

The above compensator, together with the notch filter of section 5.2, gave exellent dynamic response to a step input signal simulating position as shown in fig. 5.2. The rotor

of bearing no. 1 could safely be spun at all speeds up to the maximum attainable of 25 000 r/min. (2618 r/s). At the same time a square wave perturbation signal V_{in} was applied driving the rotor from x=-0,25 mm to x=0,25mm. The measured settling time of the rotor was approximately 10ms (see fig. 5.2a).

With the rotor stationary a thin rope was looped around it with which it was pulled in the radial plane through a spring balance. As this radial load was increased the rotor displacement was noted by displaying the displacement signal on an oscilloscope. There was no perceptible displacement, even at the maximum sensitivity setting, representing less than 10µm per division on the oscilloscope, which indicated the successful operation of the integral feedback. Only after the maximum load, which was found to be 3,5kg in this case, was exceeded, control was lost and the displacement would suddenly jump to its maximum value of 1mm.

It was expected that radial loading may have some adverse effect on the system performance at high speeds due to the magnetic hysteresis and eddy current effects that would be present in the rotor. Due to the unsymmetry in magnetic fields under these conditions the resultant force set up by the above parasitic effects would not be in line with the control axis concerned and a degree of crosscoupling between the initially orthogonal axes is to be expected. These effects were not analysed theoretically but an attempt was made to measure them experimentally by rotating the whole bearing through 90 degrees so that the rotational axis was horisontal, thus loading the bearing in the radial plane by gravity. For bearing no. 1 this loading amounted to 0,7 kg, which was also determined by means of the spring balance as described above. The dynamic performance, with a step input as above, under these loading conditions, was identical to the unloaded case. It was thus concluded that these parasitic effects could safely be neglected when considering the dynamic performance.

In conclusion it may thus be stated that this phase-gain method of compensator design is very successful, provided parasitic resonance effects are taken into account. In practice the latter proved to be the most difficult problem to overcome since these resonances, due to their parasitic nature, are usually not known beforehand and their presence makes it very difficult to achieve asymptotic stability. After overcoming this hurdle they can be measured readily which allows appropriate countermeasures to be taken.

5.2 Large Signal (Describing Function) Analysis of Magnetic Bearing with Compensated Feedback

Since the describing functions $N(\hat{E},\omega)$ and $N_s(\hat{E},\omega)$ derived in the previous chapter are also frequency dependent the total loop gain $L(s)=G_s(s)H(s)$ which includes either $N(\hat{E},\omega)$ or $N_s(\hat{E},\omega)$ is plotted in the gain-phase plane in order to test the system for stability. $H(s)$ is the compensator transfer function derived in the previous section. The gain-phase plot of $L(j\omega)$ is shown in fig. 5.3 for various driving voltage amplitudes $\hat{E}$ and quiescent flux densities B. It will be seen that for very low $\hat{E}$ and B the curve passes to the left of the critical point suggesting the existence of a stable limit cycle. Such a limit cycle was only observed in the practical system on very rare occasions and normally would disappear after practically any form of disturbance. This was in spite of the fact that the quiescent current was zero and there was no bias force on the bearing as it was operated in the horisontal plane. This phenomenon suggests that the remanent flux in the magnetically "soft" core material is normally sufficient to shift the gain-phase curve upwards so that it passes to the right of the critical point ensuring asymptotic stability. This effect also reduces the amount of shift caused by amplitude variation considerably, making the assumption of the system being linear, when designing the compensator, more valid. This progressive decrease in the gain variation as a function of amplitude with increasing flux density can be seen when progressing from fig. 5.3a through fig. 5.3c.

A fairly large amplitude limit cycle could, however, be

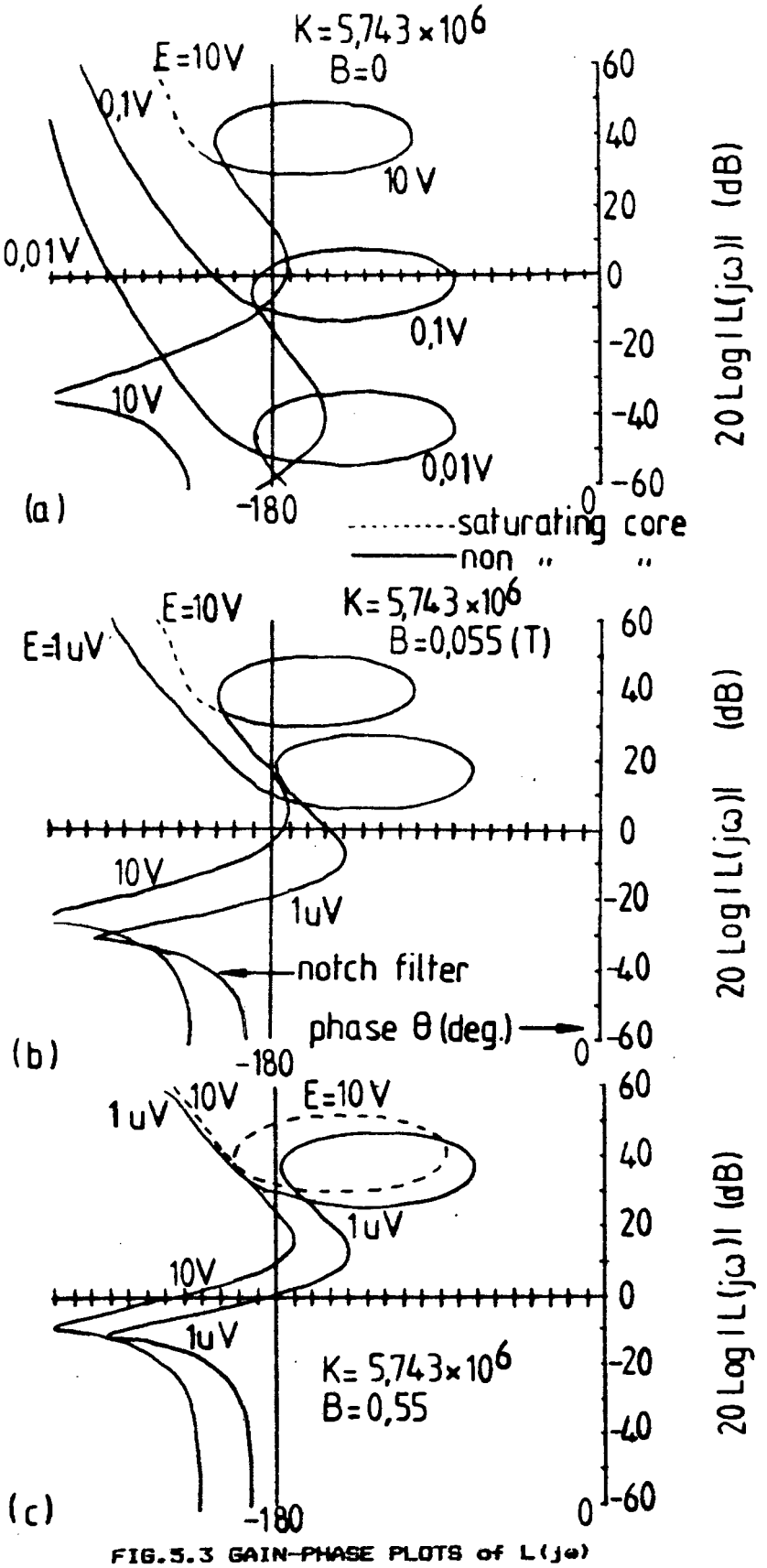

FIG.5.3 GAIN-PHASE PLOTS of L(jω)

brought on at will by reducing the loop gain sufficiently, thus causing the gain-phase curve to pass to the left of the critical point. This leads to the buildup of oscillations which in turn shift the gain-phase curve upwards untill the curve passes exactly through the critical point whereupon the amplitude of oscillation remains stable, representing a stable limit cycle. This stable limit cycle is caused by the upper one of the two crossings of the gain-phase curve with the -180 degrees axis (ie when ignoring the resonance loop in the curve for the moment) as can be seen with the Ø,1V and Ø,ØØ1V curves in fig. 5.3a. On the other hand, if the gain-phase curve is moved up far enough, such as by a combination of high gain, high amplitude and high flux density the lower -180 degree axis crossing could be caused to move through the critical point causing an unstable limit cycle to develop because a further increase in amplitude causes the curve to move further to the left, away from the critical point. This situation is depicted in fig. 5.3c.

This unstable limit cycle behaviour was confirmed experimentally by increasing the gain and loading the bearing considerably, thus creating a large quiescent flux, whereupon it would break into oscillation. Removal of the load would cause it to stabilize immediately, provided the gain was not above some critical level, beyond which the oscillations would persist simply because sufficient shift in the curve could then be maintained by $\tilde{E}$ alone to sustain the oscillations.

A gain setting could be found, however, where no limit cycle could be brought on, and yet satisfactory dynamic response could be maintained.

5.3 State Variable Feedback

When the small signal (linear) model of the voltage driven bearing in section 4.3 is simplified, as explained below, and represented in state variable form, the following state equations are obtained (double width, upper case characters denote vectors or matrices):

$$s\mathbf{X}=\mathbf{A}\mathbf{X}+\mathbf{B}u \qquad \ldots\ldots(5.5)$$

where $\mathbf{A}=\begin{bmatrix} \emptyset & \emptyset & \emptyset \\ \frac{1}{M} & \emptyset & \emptyset \\ \emptyset & 1 & \emptyset \end{bmatrix}$, $\mathbf{B}=\begin{bmatrix} -R \\ \emptyset \\ \emptyset \end{bmatrix}$, $\mathbf{C}=\begin{bmatrix} \emptyset & \emptyset & 1 \end{bmatrix}$,

$\mathbf{X}=\begin{bmatrix} f \\ v \\ x \end{bmatrix}$, u is the input (scalar) and

$$R=\frac{2B}{\mu_o n}\left[1+\left(\frac{4}{\pi}\right)^2\right]^{\frac{1}{2}} \quad \text{from eq. (4..29)} \qquad \ldots\ldots(5.6)$$

Thus the transfer function relating magnetic force to input voltage obtained from eq. (5.5) is assumed to be R/s which provides a phase shift of $-\pi/2$ rad. for $s=j\omega$ instead of -Ø,666 rad. (-38,146°) as determined in section 4.3 (see eq.(4.29)). Such an assumption makes the transfer function compatible with classic linear systems theory and leads to a more conservative design because the true phase shift is less than that assumed in the linear model.

The negative sign of R in $\mathbf{B}$ has been inserted here for convenience to indicate negative feedback. In practice the summing amplifier for branches k_1, k_2 and k_3 (see below) would provide the required sign inversion.

If ω is assumed to be remote from the suspension resonance "kink" eq. (4.27) may be written as

$$G_s(j\omega)=jR/M\omega^3 \qquad \ldots\ldots(5.7)$$

where $M=M_e$ for $\omega<<z_m, p_m$
and $M=M_r$ for $\omega>>z_m, p_m$

The latter is derived from equations (4.2Ø), (4.22), (4.29) and (5.6).

Applying direct state variable feedback to the above simplified model gives a system with characteristic polynomial

$$P_c(s)=s^3+(Rk_1/M)s^2+(Rk_2/M)s+Rk_3/M \quad \ldots\ldots\ldots\ldots\ldots\ldots (5.8)$$

Assuming $P_c(s)$ to have 3 arbitrary but equal roots at $s=-\lambda$ gives

$$P_c(s)=s^3+3\lambda s^2+3\lambda^2 s+\lambda^3 \quad \ldots\ldots\ldots\ldots\ldots\ldots\ldots\ldots\ldots\ldots (5.9)$$

Equating corresponding coefficients in equations (5.8) and (5.9) produces

$$k_1=3\lambda/R$$
$$k_2=3\lambda^2 M/R$$
$$k_3=\lambda^3 M/R \quad \ldots\ldots\ldots\ldots\ldots\ldots\ldots\ldots\ldots\ldots\ldots\ldots (5.10)$$

In the absence of noise this state variable feedback is equivalent to feeding back from x alone via a feedback network with transfer function:

$$H(s)=(Mk_1 s^2+k_2 s+k_3)$$
$$=(M\lambda/R)(3s^2+3\lambda s+\lambda^2) \quad \ldots\ldots\ldots\ldots\ldots\ldots\ldots\ldots (5.11)$$

Applying such a hypothetical compensator to the full system model of eq. (4.37) produces the gain-phase plot for the loop transfer function

$$L(j\omega)=G_{st}(j\omega)H(j\omega) \quad \ldots\ldots\ldots\ldots\ldots\ldots\ldots\ldots\ldots\ldots (5.12)$$

It can be seen here that, with a suitable choice of parameters, such feedback provides a phase margin of approximately 110° to 142° and an infinite gain margin. This clearly rules out any possibility of an unstable limit cycle which makes it worth investigating. See fig. 5.4.

An important observation to be made at this stage is that state variable feedback is equivalent to using a feedback compensator with a single input signal, X, which then also

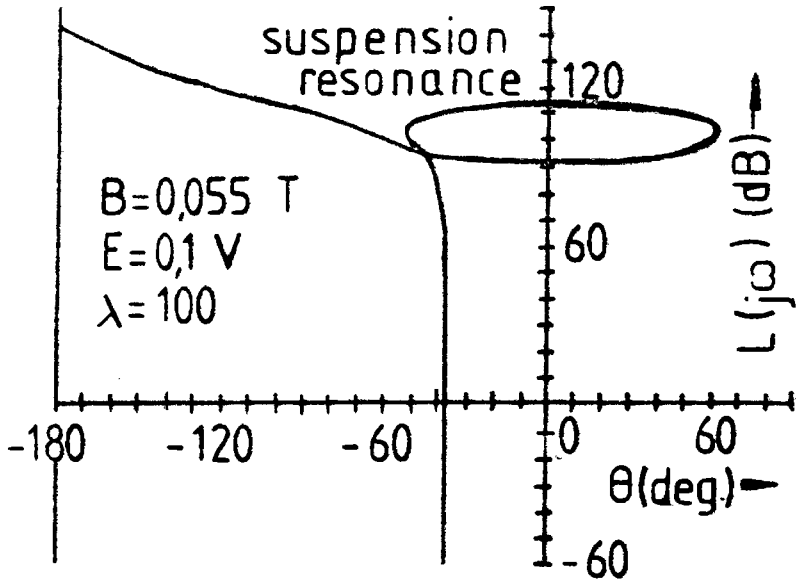

FIG. 5.4 GAIN PHASE PLOT of L(jω) with STATE VARIABLE FEEDBACK

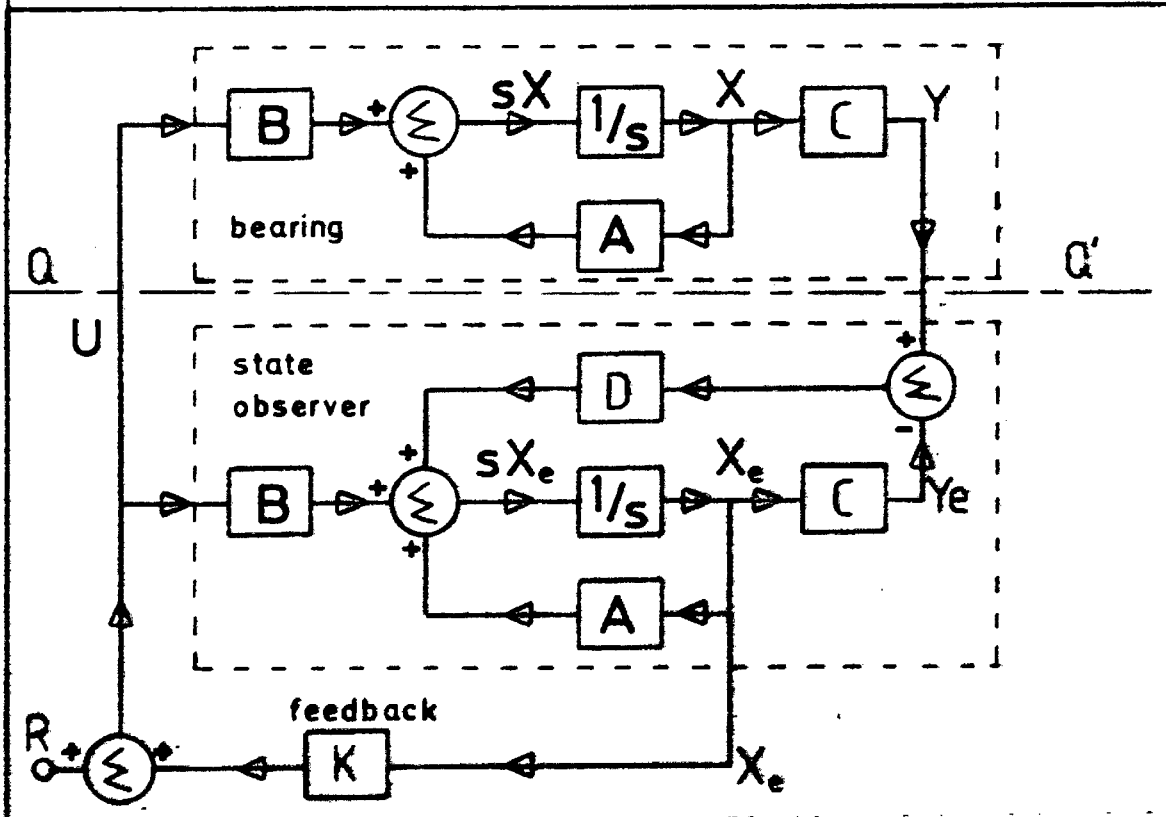

FIG. 5.5 MAGNETIC BEARING with STATE OBSERVER FEEDBACK

differentiates X twice, but without the disadvantage of being as noise sensitive as a true differentiator.

5.3.1 State Observer

Transducers for measuring all the states of the system are not readily available and are very costly. This problem suggests the incorporation of an observer which will estimate the system states. These estimated values are then used for feedback. In so doing an equally good dynamic response may be obtained after the initial transient has died away, since the estimated values will asymptotically approach the true values after the decay of the transient, irrespective of the type of input signal.

The validity of the above statement, although generally true, will be tested for this type of application.

The magnetic bearing represented in state variable form with associated state observer is represented by the block diagram of fig. 5.5. The well known fundamental concepts of this state observer will be repeated here (for a more detailed discussion the reader is referred to the literature).

At the onset it must be emphasised that the system (magnetic bearing in this case) is assumed to be linear time invariant, in other words only small displacements about the neutral point are considered. This is in order to make the theory valid and manageable. Practical experience as well as the results given above indicate that such an assumption produces workable results.

It will be seen from fig. 5.5 that, temporarily ignoring block D, the observer is a simulation of the system and thus the dynamic behaviour of both the system and the observer are described by identical state space equations:

$$sX = AX + BU$$
$$Y = CX \qquad \ldots\ldots\ldots\ldots\ldots\ldots\ldots\ldots\ldots\ldots (5.13)$$

and

$$sX_e = AX_e + BU$$
$$Y_e = CX_e \qquad \ldots\ldots\ldots\ldots\ldots\ldots\ldots\ldots\ldots\ldots (5.14)$$

where X is the system state vector and
X_e is the estimated state vector in the observer.
Y and Y_e are the corresponding output vectors,
whilst A, B and C are matrices of matching dimensions.

Since the latter matrices are identical for both systems it is clear that, provided the initial conditions are identical, $X_e = X$ and $Y_e = Y$ for all inputs and all time. As long as this is the case the input to and consequently also the output from block D is zero and eq. (5.14) holds.

At turn-on $X \# X_e$, initially, and thus $Y \# Y_e$. For the observer

$$sX_e = AX_e + BU + D(Y - Y_e) \ldots\ldots\ldots\ldots\ldots\ldots\ldots\ldots (5.15)$$

From the above we obtain the following for the difference vector $(X - X_e)$ between the two systems:

$$s(X - X_e) = (A - DC)(X - X_e) \ldots\ldots\ldots\ldots\ldots\ldots\ldots\ldots (5.16)$$

In this equation it is seen that $(X - X_e)$ is independent of the input U and will thus decay to zero provided all the eigenvalues of $(A - CD)$ are in the left half of the complex s-plane.

The design problem is thus firstly to choose D to be conformable with C and secondly to ensure that the above requirement concerning the eigenvalues is met.

After this has been done a suitable feedback matrix K is chosen that will be identical to that chosen for direct state variable feedback to give the system any desired dynamic response.

It must be appreciated, however, that the above dynamic response may only be achieved for inputs and disturbances which occur in vectors R, U and in the feedback path (through K). This is due to the symmetry of the total system. All responses due to such inputs and disturbances will cancel at the input of D and thus any natural frequencies associated with D will not be "excited". Any unsymmetrical disturbance, however, which occurs in either the bearing or the observer alone, will cause these natural frequencies to be "excited" and the ensuing response will generally be poorer than that of a direct state variable feedback system.

Returning to the magnetic bearing, it must be kept in mind that the input reference R is usually held at zero, since the rotor is only required to remain in its neutral (zero) state and thus the input node for R need not physically exist.

Further it is to be expected that most of the disturbances encountered will be unsymmetrical (ie in the bearing only) and unless these disturbances are measured and the whole system is modified so that they may be considered as inputs some of the advantages of the state observer are lost, as explained above.

After the removal of the node R the whole system below the line QQ^1 in fig. 5.5 may be seen as a simple feedback network coupling the output Y of the bearing back to the input. The transfer function matrix of this feedback system is found to be

$$H_o(s)=K(sI-A-BK+DC)^{-1}D \qquad \text{.....(5.17)}$$

The values $K=[k_1\ k_2\ k_3]$ in eq. (5.10) will be used below for state observer feedback.

The difference feedback matrix for the state observer is defined as

$$\mathbf{D}=[d_1\ d_2\ d_3]^t \qquad (5.18)$$

To ensure convergence between the true and estimated state vectors the 3 eigenvalues of $(\mathbf{A}-\mathbf{DC})$ are conveniently chosen to be equal to some arbitrary real value $-\delta$. This produces

$$|s\mathbf{I}-\mathbf{A}+\mathbf{DC}|=s^3+d_3s^2+d_2s+d_1/M$$

$$=s^3+3\delta s^2+3\delta^2 s+\delta^3 \qquad (5.19)$$

Thus $d_1=M\delta^3$

$d_2=3\delta^2$

$d_3=3\delta$ $\qquad (5.20)$

The laborious task of calculating $H_o(s)$, which is a scalar in this case, according to equation (5.17), can now be undertaken. Such a calculation finally produces

$$H_o(s)=\frac{(k_1d_1+k_2d_2+k_3d_3)s^2+\left(\frac{k_2d_1}{M}+d_2k_3\right)s+\frac{d_1k_3}{M}}{s^3+(Rk_1+d_3)s^2+\left(Rk_1d_3+d_2+\frac{Rk_2}{M}\right)s+Rk_1d_2+\frac{Rk_2d_3}{M}+\frac{Rk_3}{M}+\frac{d_1}{M}} \qquad (5.21)$$

$H_o(s)$ here has the same form as $H(s)$ in eq. (5.2) and if the two should be made identical, identical system performance will result. In order to synthesize the above by means of an observer, which may be a simulator of the true system, at least three operational amplifiers are required whereas $H(s)$, according to eq. (5.2), may be obtained by means of two operational amplifiers only. Mathematically and conceptually the straightforward feedback compensator approach is far simpler than the state observer approach, but produces the same result. The latter thus justifies no further consideration for this application.

5.4 "Sensorless" Feedback Compensation

It should be possible to derive the rotor displacement from the current-voltage relationship at the driving coils. If this is possible the need to install sensors will disappear because, as we have seen above, the system can be stabilised satisfactorily with a position feedback signal only. Stated in more general terms, the following question has to be answered: If the coil voltage is the controlled input to the system and the variable component of the current in the coil (this is the current $i_1(t)$ as defined in section 3.1.1) is taken as the only available output, will the system then be completely observable? In case this is true, then hopefully, a more reliable system may be built at lower cost.

Restricting this investigation to the small signal linear model of the system derived in section 3.4 equations (3.31) are rearranged as follows:

$$\begin{bmatrix} sP \\ sV \\ sX \end{bmatrix} = \begin{bmatrix} \emptyset & \emptyset & \emptyset \\ \frac{2I_o}{Md} & o & o \\ \emptyset & 1 & \emptyset \end{bmatrix} \begin{bmatrix} P \\ V \\ X \end{bmatrix} + \begin{bmatrix} 1 & \emptyset \\ \emptyset & 1 \\ \emptyset & \emptyset \end{bmatrix} \begin{bmatrix} E \\ A \end{bmatrix}$$

$$I_1 = \begin{bmatrix} \emptyset & \emptyset & \frac{I_o}{d} \end{bmatrix} \begin{bmatrix} P \\ V \\ X \end{bmatrix} + \begin{bmatrix} \frac{r_1 + sL_o}{r_1 L_o s} & \emptyset \end{bmatrix} \begin{bmatrix} E \\ A \end{bmatrix} \quad \text{.....(5.22)}$$

Equations (5.22) are defined as

$$sX_v = A_v X_v + B_v R_v$$
$$I_1 = C_v X_v + S_v R_v \quad \text{.....(5.23)}$$

where the subscript v denotes the voltage driven system.

From the above it is seen that the matrix (see Kuo [38], section 4.16)

$$\begin{bmatrix} C_v \\ C_v A_v \\ C_v A_v^2 \end{bmatrix} = \begin{bmatrix} \emptyset & \emptyset & \frac{I_o}{d} \\ \emptyset & \frac{I_o}{d} & \emptyset \\ \frac{2I_o^2}{Md} & \emptyset & \emptyset \end{bmatrix} \quad \ldots\ldots\ldots\ldots\ldots\ldots (5.24)$$

is nonsingular provided $I_o \neq \emptyset$

Thus, as long as the quiescent coil current is kept at some finite nonzero value the system is observable and the concept of "sensorless" feedback may be put to practice. This would be practical where a quiescent current is required to counteract a constant load such as the gravitational load on the axial bearing in this application.

The system of equations (5.22) or (5.23) is depicted graphically in fig. 5.6.

Although there may be numerous different compensator configurations the most straightforward is probably that shown in fig. 5.6. The control current I_1, as can be seen from the figure, consists of 3 components being:

a) a current directly related to position x, say $I_x=(I_o/d)X$
b) the magnetising current $I_m=E/(L_o s)$ and
c) a shunt component $I_s=E/r_1$ due to the eddy currents in the core (see chapter 3).

If the latter two components could be simulated in the compensator and subtracted from I_1 we would have regained I_x. Since I_x is directly related to x, the feedback compensator design problem is now reduced to that of section 5.1. This means two suitable zeros with associated

high frequency poles have to be added into the feedback loop.

Since the system in fig. 5.6 is a two terminal (one port) system where the current into the port is used to control the terminal voltage across it, the total compensator may be seen simply as a compensating impedance:

$$Z(s)=\frac{Z'(s)}{1+\left(\frac{1}{r_1}+\frac{1}{L_o s}\right)Z'(s)}\ (\Omega) \qquad (5.25)$$

where $Z'(s)$ may, for the sake of convenience, be chosen to possess two identical poles and two identical zeros:

$$Z'(s)=\frac{p^2 R_c (s-z)^2}{(s-p)^2}\ (\Omega) \qquad (5.26)$$

where R_c is a constant with dimensions "ohms".
If p is chosen sufficiently large

$$Z'(s)\doteq R_c(s-z)^2\ (\Omega) \qquad (5.27)$$

Assuming current components I_m and I_s of I_1 to be exactly compensated for by branch $-(1/r_1+1/(L_o s))$, the characteristic equation of the total system in fig. 5.6 reduces to:

$$1+\frac{2I_o^2 R_c (s-z)^2}{Md^2 s^3}=0 \qquad (5.28)$$

for which a root locus diagram for variable R_c is presented in fig. 5.7.

At the breakaway point (s=3z), for non-oscillatory response,

$$\frac{2I_o^2}{Md^2}R_c=\frac{27}{4}|z| \qquad (5.29)$$

whilst for $\frac{2I_o^2}{Md^2}R_c>\left|\frac{z}{2}\right|$ (5.30)

asymptotic stability is ensured.
Unfortunately, since Z(s) is not positive real, it cannot be synthesized with passive components only, and thus has

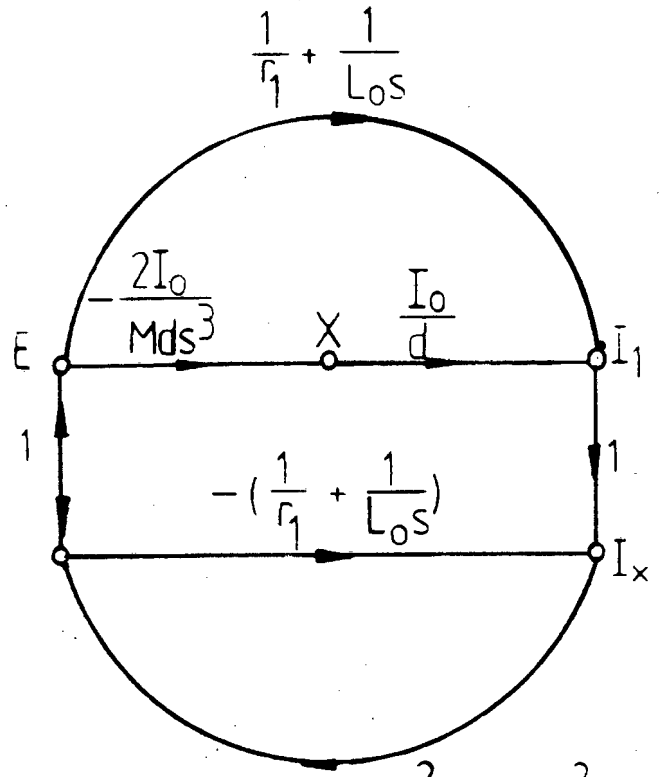

FIG. 5.6 "SENSORLESS" FEEDBACK COMPENSATION

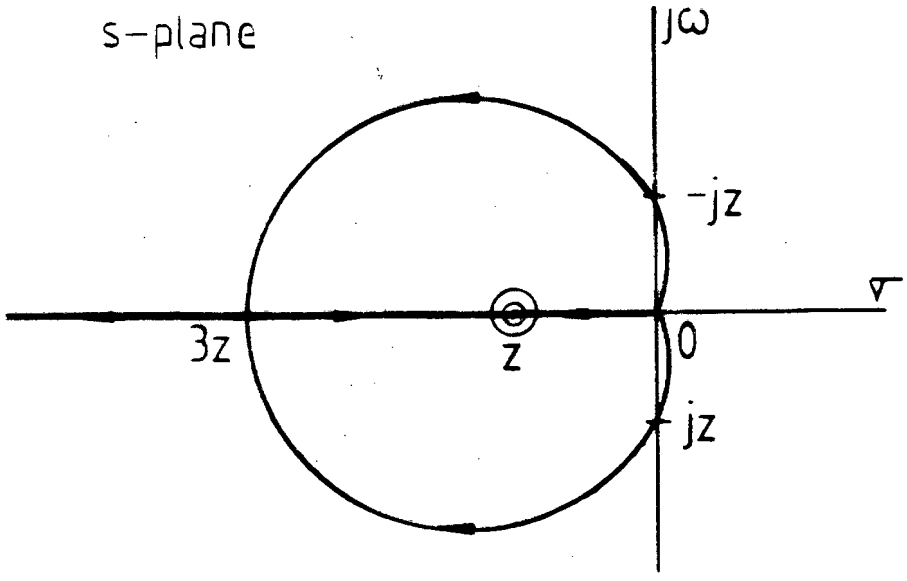

FIG. 5.7 ROOT LOCUS for "SENSORLESS" SYSTEM

to be a trans-impedance amplifier with the necessary dynamic behaviour.

From equations (5.2Ø) and (5.22)

$$Z(s)=\frac{s^3-2zs^2+z^2s}{\frac{s^3}{r_1}+\left(\frac{1}{L_o}-\frac{2z}{r_1}\right)s^2+\left(\frac{z^2}{r_1}-\frac{2z}{L_o}+\frac{1}{R_c}\right)s+\frac{z^2}{L_o}}$$

$$=\frac{r_1 s\left(s^2-2zs^2+z^2\right)}{s^3+\left(\frac{r_1}{L_o}-2z\right)s^2+\left(z^2-2z\frac{r_1}{L_o}+\frac{r_1}{R_c}\right)s+\frac{z^2}{L_o}} \quad \ldots\ldots\ldots\ldots\ldots\ldots (5.31)$$

5.4.1 Practical Results with Sensorless Feedback

Figure 5.8 is a schematic diagram of the circuit used to test the idea of sensorless feedback. This circuit operates as follows:

The total coil current is measured across shunt resistor r_s by means of differential amplifier A_5, which produces an output signal proportional to I_1+I_o. "I_o" is subtracted from this signal in amplifier A_6, to produce an ouput "$-I_1$". A signal "-E" representing -E appears on the output of A_1 which is obtained by amplifying the input voltage to the power amplifier V_{in} by the voltage amplification factor of the power amplifier K_k and simultaneously subtracting the voltage drop across the control coil internal resistance $I_1 r_i$. Signal "-E" is then used to generate the two "current components", "E/r_1" and "$E/(L_o s)$" by means of operational amplifiers A_2 and A_3 respectively. The latter two signals are then subtracted from "$-I_1$" to produce signal "I_x" on the ouput of A_4.

Bode amplitude plots of |"I_x"/"E"| did not correspond to that of $|V_p/E|$, where V_p was the position signal. These Bode amplitude plots are shown in fig. 5.9. The position sensors were of the eddy current type developed especially for the experimental bearing. E was measured by means of a search coil placed in the same slot as the control coil. Thus "I_x" was not a representation of x and, needless to say, the system could not be kept stable when switching the

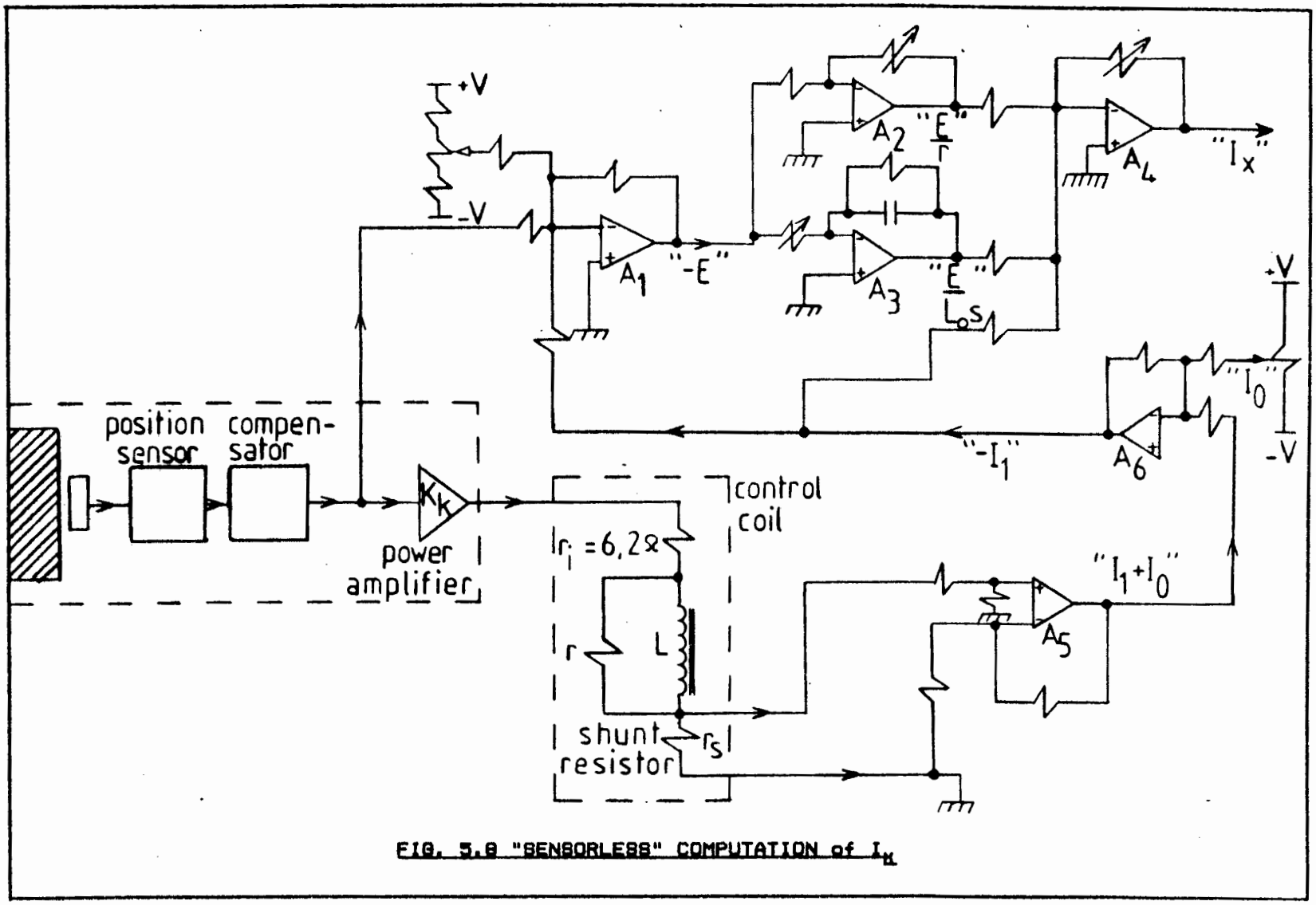

FIG. 5.8 "SENSORLESS" COMPUTATION of I_x

compensator input over from V_p to "I_x". Further measurements revealed that the relationship between E and I_1 also didn't correspond to that predicted by the above theory, indicating that the model of fig. 5.6 does not represent the physical system accurately enough. In the zone where $|I_1/E|$ is expected to roll off at 60 dB/decade, representing $|X/E|$ most closely (see fig. 5.10), this disparity is particularly noticeable.

Practical measurements of the transfer function of input voltage E to position X as well as the very successfull compensator which was designed around this latter transfer function, served to confirm the accuracy thereof. It is thus felt that the current component representing position is being masked by some unaccounted for parasitic effects such as skin effects in the unlaminated magnetic core. This would cause r_1 to be frequency dependent and not constant, as was tacitly assumed in all the foregoing discussions. At the time of this writing this problem was still unresolved and most certainly has to be followed up afterwards due to the potential advantages which it has to offer.

5.5 Conclusion

After investigating the various possibilities dealt with in this chapter, the following procedure appears to produce the best practical results when designing a feedback compensator for a single magnetic bearing:

(a) Draw theoretical Bode-amplitude plots for the voltage driven system with control voltage as input and relative displacement between rotor and stator as output.

(b) Construct (graphically) the asymptotes for the inverse of the feedback transfer function H(s).

(c) Synthesise H(s) and close the feedback loop.

(d) After succeeding in making the practical system asymptotically stable, by varying the parameters (mainly the gain constant) of H(s), the true transfer function (Bode-amplitude plot) is determined experimentally by

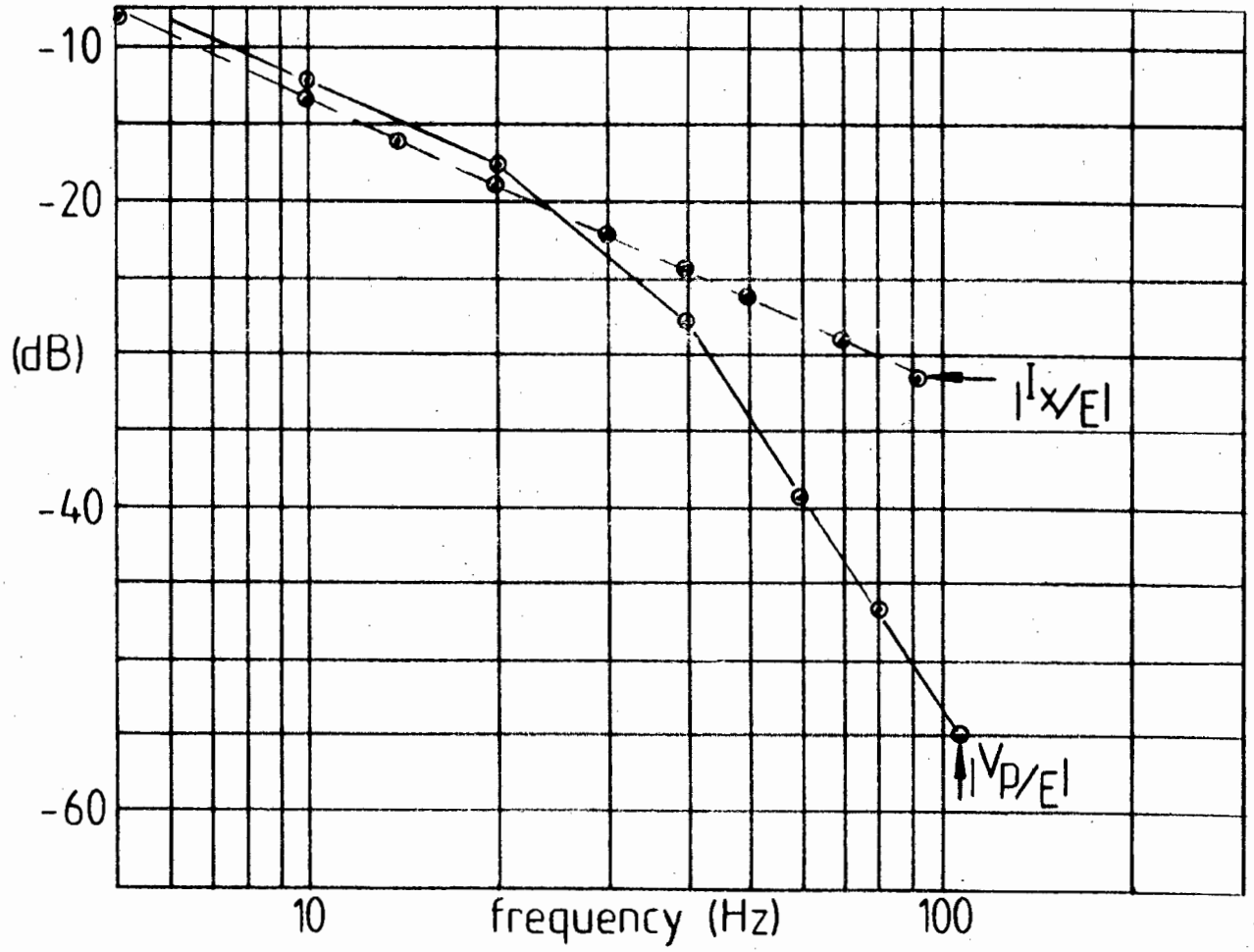

Fig. 5.9 BODE DIAGRAMS of "I_x/E" and $V_{p/E}$

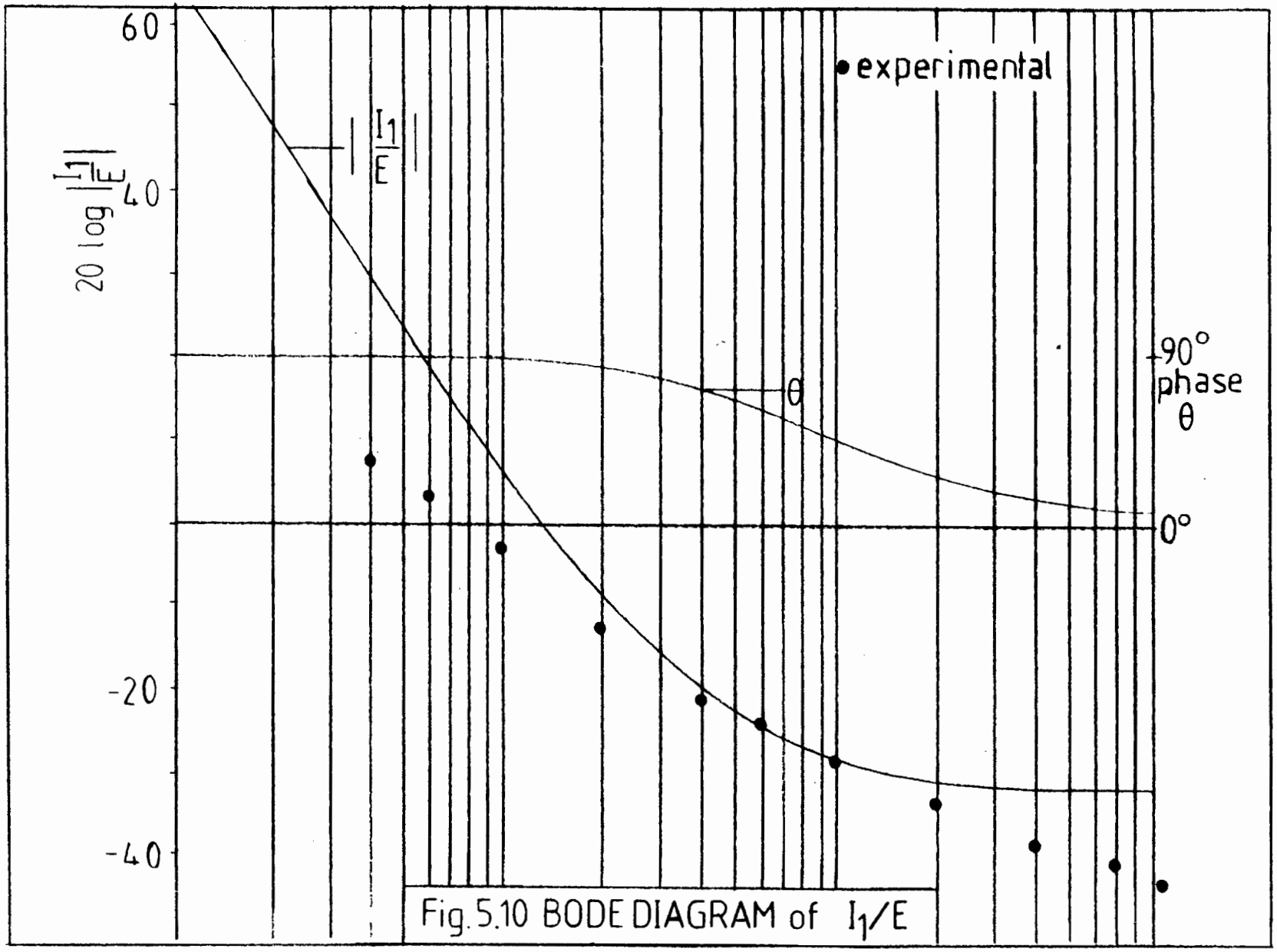

Fig. 5.10 BODE DIAGRAM of I_1/E

injecting a displacement perturbation signal into the loop (input V_{in}, fig. 5.2).

(e) Repeat steps (b) and (c) to obtain a better solution of H(s).

(f) Parasitic rotor resonances are eliminated by employing a notch filter tuned to the resonance frequency (see appendix 4B).

Although the magnetic bearing system is nonlinear, the variation in loop gain due to amplitude variation was found to be sufficiently small to make the above design procedure, based on linear theory, practical. This is mainly due to the effect of the magnetic remanence of the core material. When a more ideal core material is used such as magnetically soft ferrites, a stable limit cycle should be expected.

It was demonstrated that the use of a state observer has no advantage over the straightforward approach outlined above.

Further it was demonstrated theoretically that a "sensorless" system is completely observable from the current-voltage relationship at the driving coil. This suggests a cheaper and more reliable system employing no sensors, but only applicable to magnetic bearings where a nonzero quiescent current is required. This would typically be the case when the bearing is constantly loaded by a gravity field. Practical results obtained with such a "sensorless" system indicated that the theoretical model which was employed here was probably an oversimplification of the practical situation since the bearing could not be stabilised with the compensator based on this model. Follow-up work is thus required regarding this topic.

CHAPTER 6

REDUCTION OF ENERGY LOSSES IN MAGNETIC BEARINGS ARISING FROM ROTOR IMBALANCE

It is virtually impossible to construct a high speed flywheel rotor which is perfectly balanced [1]&[41], and even if it were possible to balance the rotor perfectly at any particular speed, the balance would constantly shift with changing speed due to changing material stresses. The rotor will tend to rotate about its centre of mass which does not normally coincide with the geometric centre of that portion of the rotor from which its position is sensed for the purpose of position control feedback. The position sensors would thus in turn give out cyclic displacement signals which are synchronised with rotor rotation. The servo loop will constantly attempt to correct for this cyclic "displacement" giving rise to unnecessary losses in the system. This phenomenon was found to be particularly noticeable in the radial magnetic bearing investigated here.

6.1 Elimination of Imbalance Signals

The frequency separation between the cutoff frequency required for the servo loop, which will ensure a reasonable settling time, and the lowest rotation frequency whereby the rotor is operated, is found to be rather small, typically about one half of a decade. This phenomenon makes a low pass filter impractical because a cutoff which is too steep will be required which will give rise to ringing that will be quite unacceptable.

The only practical solution seems to be the use of a sharp notch filter with a centre frequency coinciding with the rotation frequency. This centre frequency will have to track the rotation frequency very closely.

The latter requirement will be difficult to meet with any kind of continuous time filter. A discrete time notch filter which derives its sampling signal directly from the

rotor will automatically track the rotor frequency. If at least two samples are taken per revolution the Nyquist criterion is automatically satisfied for the imbalance signals as well as the normal displacement signals which are assumed to be well below the rotation frequency. During runup, whilst the rotation frequency traverses through the passband of the servo loop, the sampling process may be disabled and the displacement signals allowed through continuously to prevent any aliasing. Since this runup time will normally represent a very small proportion of the total operating time the losses associated with imbalance during runup will be negligible.

6.2 Discrete Notch Filter

Assuming that two samples of the displacement signal are taken per revolution of the rotor, the sampling interval for the rotor frequency, and consequently also the imbalance signal, will be π radians per sampling interval. A further assumption which is implied here is that the imbalance signal will be a pure sinusoid, which is not unreasonable, provided that the rotor is machined circularly at the sensors and the characteristic of the position transducers is fairly close to linear.

Since the imbalance signal has to be eliminated, a suitable notch filter is obtained by choosing a discrete transfer function H(z) which possesses a zero $z_1=-1$ and a pole $p_1=-a$ where $-a>-1$ but close to -1 in the complex z-plane. See fig. 6.1.

Thus $H(z)=(z+1)/(z+a)$ .....(6.1)

The corresponding difference equation for H(z) is

$Y(k)=X(k)+X(k-1)-aY(k-1)$ .....(6.2)

where Y(k) is the discrete time output of the filter and X(k) is the discrete time input to the filter.

This filter is implemented by 3 sample and hold (zero order

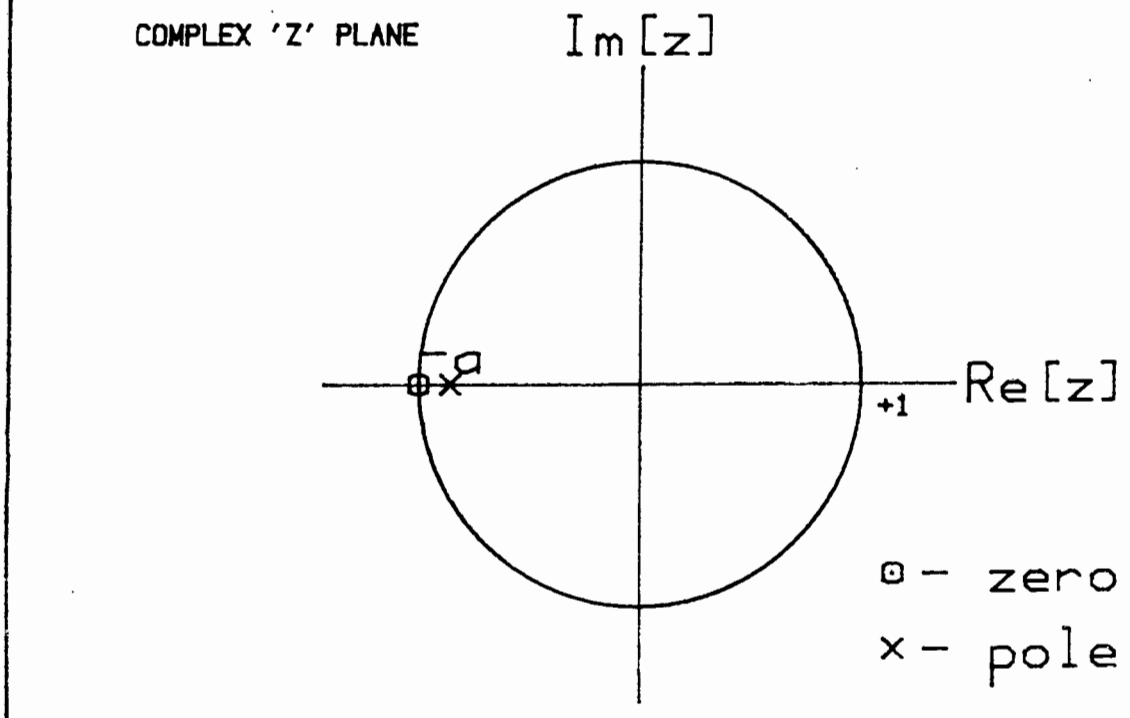

FIG. 6.1 NOTCH FILTER - POLE-ZERO LOCATIONS

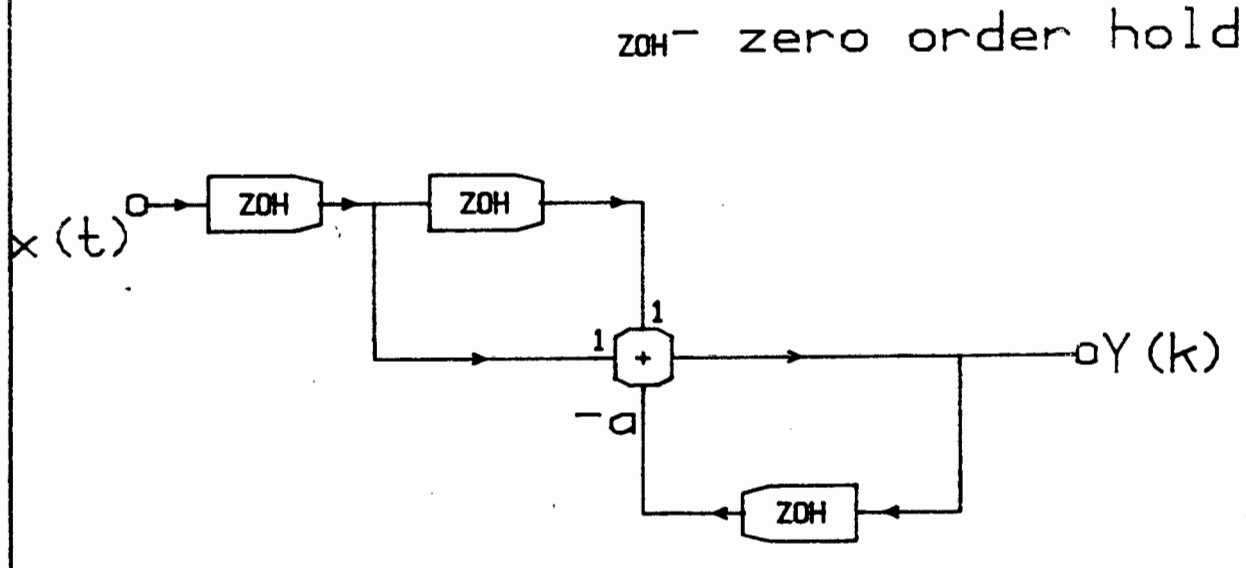

FIG. 6.2 NOTCH FILTER - BLOCK DIAGRAM

hold) circuits and one summing amplifier as shown in block diagram form in fig. 6.2.

The output of the notch filter for a discrete unity step input signal is given by

$$Y(k)=2/(1+a)-\{(1-a)/(1+a)\}(-a)^{k} \quad \ldots\ldots\ldots\ldots\ldots\ldots\ldots\ldots (6.3)$$

Y(k) is plotted for various a in fig.6.3.

6.3 Elimination of Harmonics of the Imbalance Signal

Since the above filter will totally eliminate all signals for which the sampling interval is $(2n+1)\pi$ rad/sampling interval where $n=0,1,2,..$etc., and the rotation frequency corresponds to the case where $n=0$, it is obvious that the fundamental component of the imbalance signal and all its odd harmonics will be eliminated.

All the even harmonics corresponding to sampling intervals of $2n\pi$ rad/sampling interval are aliased and appear as a steady dc component.

The nett effect of this dc signal will be to offset the rotor somewhat from its true neutral position. Most important however is that no cyclic displacement signal is generated and thus all losses associated with such cyclic signals are eliminated.

6.4 Alternate Solution

The above aliasing, which causes the even harmonics to appear as dc signals, suggests an alternate solution to the whole problem. This is obtained by the simple expedient of sampling the displacement signal once per revolution in stead of twice as in the above. This technique causes *all* the Fourier components of the cyclic imbalance signal to appear as dc components simply because the sampling interval is now $2n\pi$ rad/sampling interval. In other words the only addition required, which is to be cascaded into the servo loop, is a simple sample and hold circuit that is clocked once per revolution of the rotor. The price that

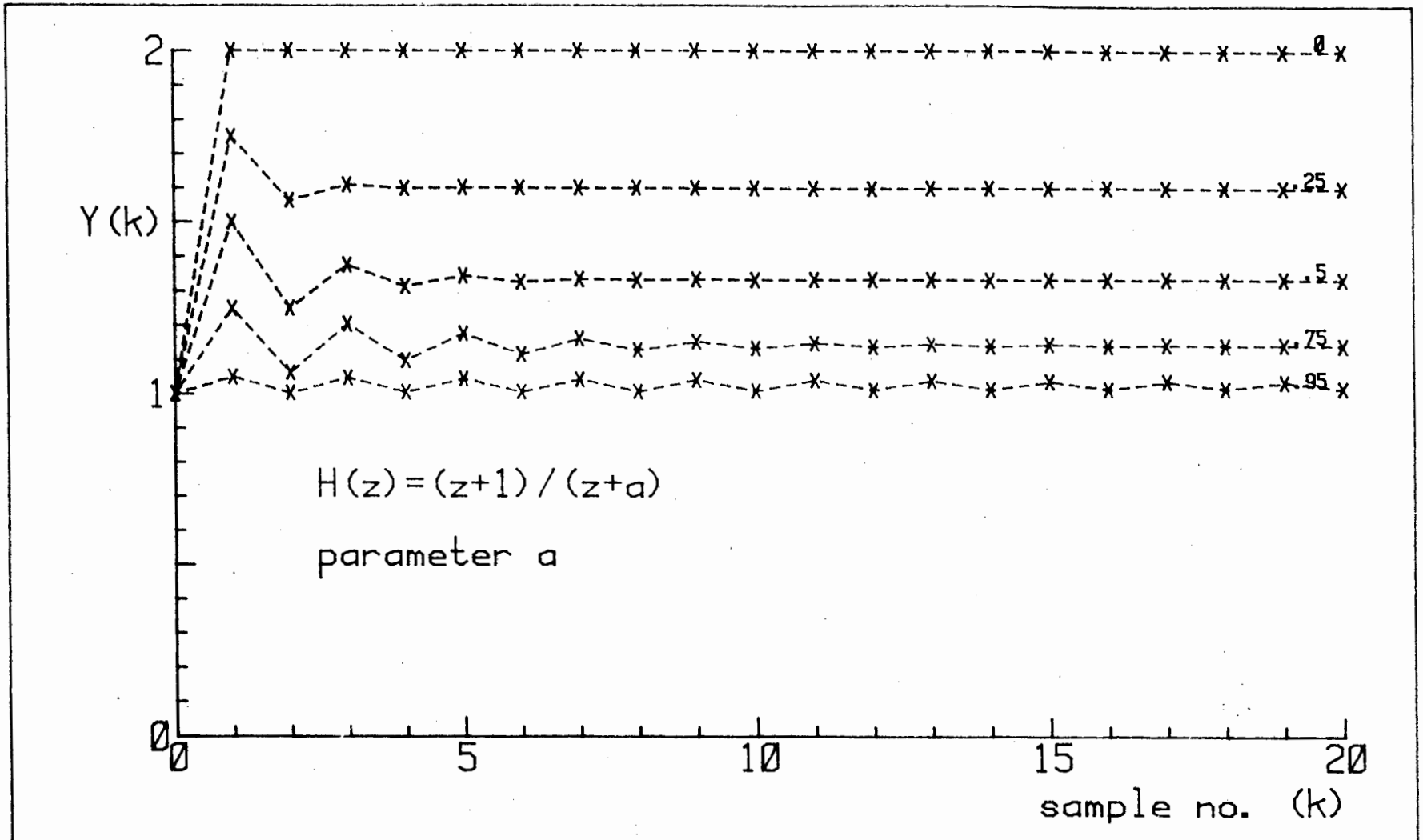

FIG. 6.3 DISCRETE NOTCH FILTER - STEP RESPONSE

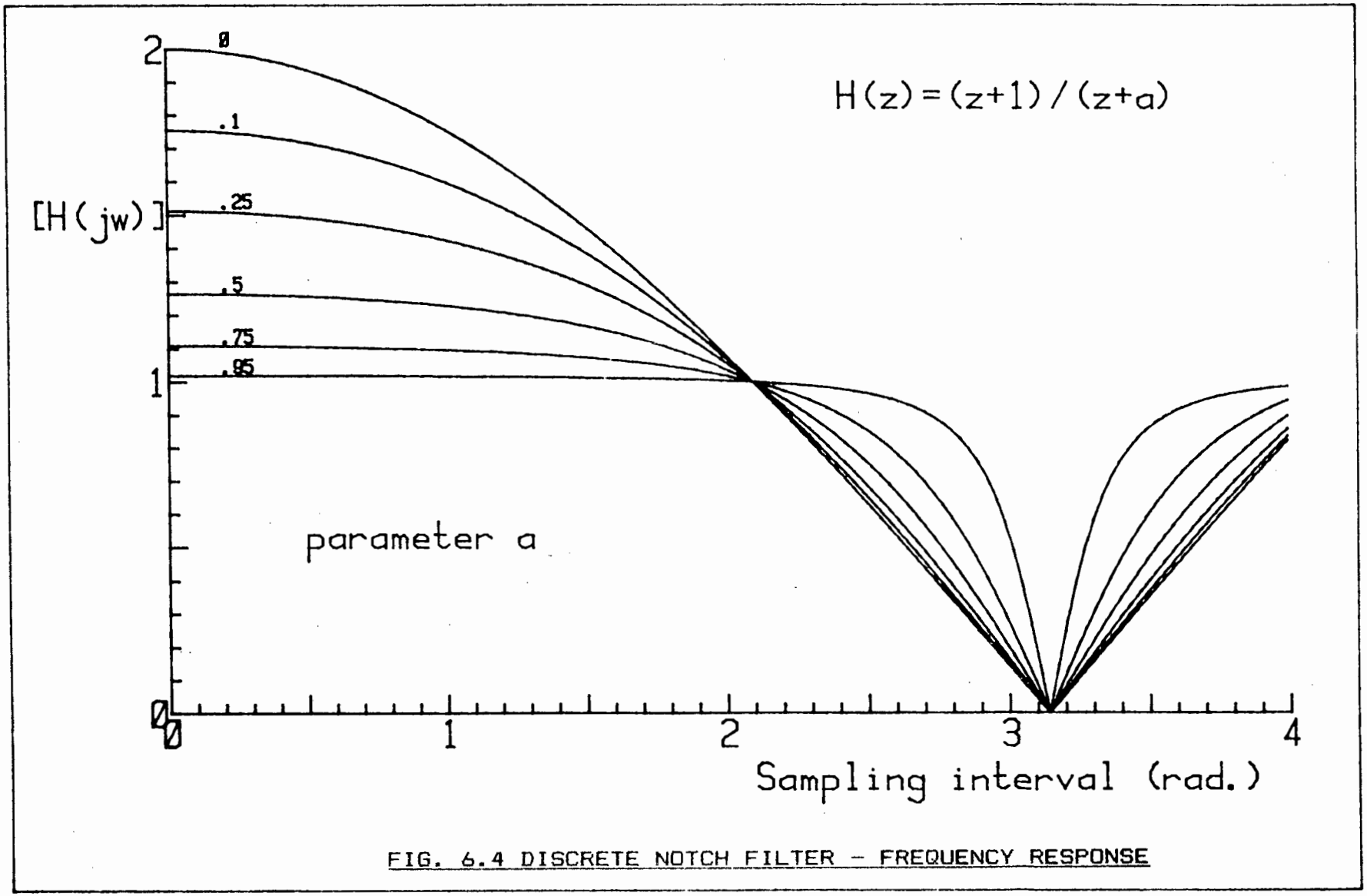

FIG. 6.4 DISCRETE NOTCH FILTER - FREQUENCY RESPONSE

has to be paid for this simpler solution is a factor 2 greater separation required between the max. frequency component of the true displacement signal and the rotation frequency, as well as the abovementioned steady (dc) displacement. The latter can be negligible in many applications especially when the rotor is accurately machined.

6.5 Practical Results and Conclusion

The alternate solution proposed above was tested on the experimental radial magnetic bearing by cascading a sample and hold circuit into the feedback loop. The clock signal for the sample and hold circuit was derived optically from the rotor shaft. During runup the sampling action was inhibited, letting the displacement signal directly through. At full speed (25 000 r/min) the sampling was enabled.

Without sampling the power consumption for this single 2kg radial (2-axis) bearing was 5 Watts and with sampling this power dropped to 0,2 Watts. This was even lower (approximately 50%) than the consumption with the rotor stationary and the sampler inoperative. This observation came as a surprise and could possibly be ascribed to the combined effect of aliasing that the sampler has on the high frequency components of the ever present noise in the system and the frequency dependence of the magnetic losses in the core material. With the sampler in action the speed of rotation also rose perceptably due to the reduced hysteresis and eddy current drag on the rotor.

Rotor displacement signal waveforms, before and after sampling, are shown in fig. 6.5

The results obtained here demonstrate the effectivity of this technique which can be applied to any magnetic bearing, even for other applications. In addition to the drop in power consumption (by a factor of 25 in the above case) the amount of vibration produced drops correspondingly because, due to the notch filter, the

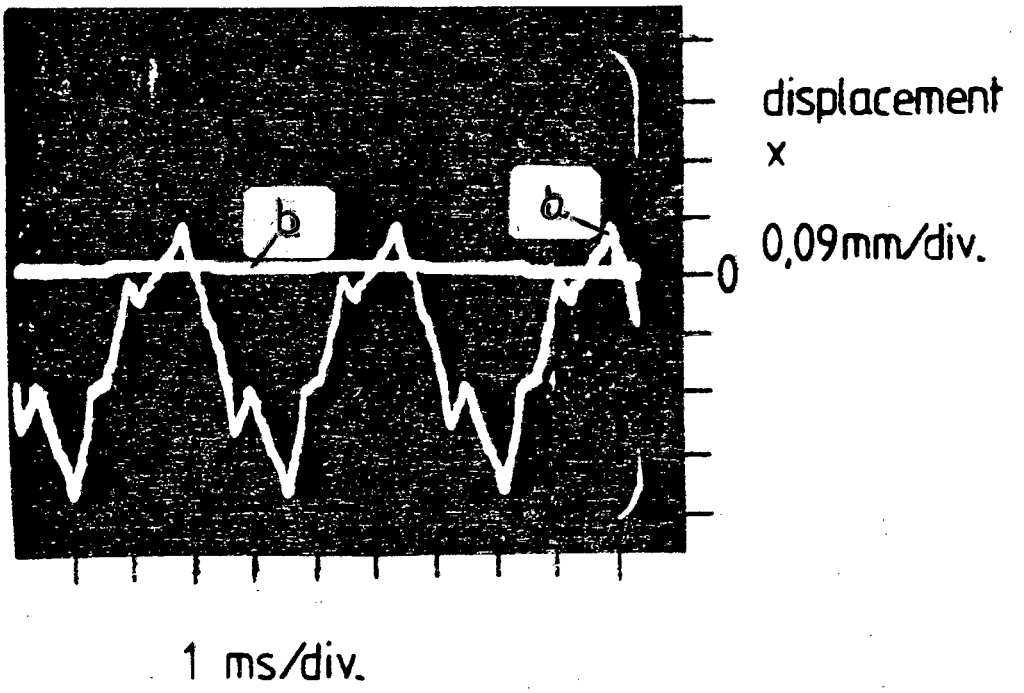

FIG.6.5 DISPLACEMENT SIGNAL (a) BEFORE and (b) AFTER NOTCH FILTER

bearing displays zero stiffness at the rotation frequency. As a consequence no imbalance forces are transmitted to the stator.

The *stiffness* here is the inverse of the mechanical *compliance* which is defined as the ratio of the reaction force that the rotor experiences per unit displacement (N/m). Both the force and the displacement could be sinusoidal functions of time. In an electrical *impedance* analogy of the system the quantities *stiffness*, *force* and *displacement* would be represented by *the inverse of capacitance*, *voltage* and *charge* repectively.

CHAPTER 7

C O N C L U S I O N

7.1 Practical Results Obtained with Magnetic Bearings

Details of practical results, obtained on the various aspects of magnetic bearings which were investigated in this thesis, were presented from time to time in the text where appropriate. At this point a résumé of these results and some remarks of a more general nature are considered neccessary.

A broader theoretical basis, than that found in the literature, for understanding magnetic bearing behaviour, has been developed to the point where it was possible to successfully explain and compensate for stable and unstable limit cycles that would develop mainly under low gain setting and overload conditions repectively. These bearings were controlled by feedback loops based on their small signal linear models. The first was a single radial bearing and the second a three dimensional bearing with five active axes, both described in detail in chapter 1. It was possible to adjust the feedback loops of these bearings so that they were critically to overcritically damped in all their modes with low settling times (<2Ø ms) as illustrated by the curves in fig. 5.2a. This performance was maintained in spite of high speed rotation which gives rise to gyroscopic cross coupling between the various axes. Integral feedback was incorporated, providing the bearing with infinite low frequency stiffness, while the "rotational frequency stiffness" could be made zero to eliminate all losses and vibrations caused by rotor imbalance, causing the power consumption to drop by a factor of 25! (see chapter 6). The model of the bearing which was used also took into consideration the main parasitic resonances of the rotor and the stator. The loading that this bearing could tolerate before "dropping out" or breaking into oscillation was Ø,5 kg/cm^2 of projected magnetic pole area. In the case of oscillations developing, these would cease immediately upon removal of

the overload condition. The magnetic components of these bearings were manufactured from solid steel, which is essential for very high speed rotation and a departure from the standard practice of laminating the magnetic cores.

Although the magnetic bearing is a nonlinear system, it was demonstrated, in theory as well as in practice, that linear control theory is applicable to the system when the control coil voltage is taken as the controlled variable (see chapters 4 and 5). This is important because it simplifies the synthesis of the feedback control loops. The theoretical development which led to this result also serves to point out the limitations of such a "linear" approach, and explains the development of limit cycles either under overload conditions, or with very low loop gain settings.

Taken in its entirety, the results obtained during this investigation were positive, since it led to a deeper insight into the subject and the theoretical results have been very successfully applied, demonstrating the practical usefulness of such bearings, particularly for high speed applications.

7.2 Evaluation of Magnetic Bearings

Practical experience gained in the application of the theories developed has made the following evaluation possible. For details the reader is referred to the main body of the text. The most salient points are summarised individually, as follows:

7.2.1 Rotational Speed

Magnetic bearings may be operated without difficulty from the stationary position up to the maximum speed dictated by the strength of the material of the rotor. In the case of bearing no. 2 investigated here this max. speed of approximately 13000 r/min was dictated by the mechanical strength of the aluminium cilinder (see fig. 1.3). As far as the bearing itself is concerned there is no speed

limitation. For example, a 120 mm diameter maraging steel rotor could be spun up to approximately 80000 r/min. When incorporating the notch filter of chapter 6 the power consumption tends to be even lower than that of the stationary bearing. This was actually observed with bearing no. 1 spinning at 25000 r/min..

7.2.2 Critical Speeds

Critical speeds or resonances which could lead to dangerous mechanical stresses in the rotor are eliminated effectively by incorporating notch filters into the feedback loops or by shaping the frequency characteristic of the feedback path in a suitable manner. This allows the rotor to operate safely over the entire speed range. This shaping is illustrated in fig. 5.1 where it can be seen how the "$^{1}/_{H(j\omega)}$" curve is "shaped" to lie below the stator resonance "kink" in "G(jω)" and, by virtue of the continuous time notch filter, "jump" over the rotor resonance peak.

7.2.3 Rotor Balance

Any rotor, manufactured by standard machining operations and which, by virtue of its shape and mass distribution, is fundamentally balanced, requires no further balancing since any residual imbalance will not be "seen" by the control loop once the discrete notch filter of chapter 6 has been incorporated. The rotor thus rotates about it centre of mass and no imbalance vibrational forces will act upon the stator. This is applicable to any envisaged operating speed, provided the sampling frequency is high enough so that the system is stable (see chapter 6). By obviating the need to balance the rotor accurately the manufacturing cost is thereby reduced considerably.

7.2.4 Mechanical Tolerances

These tolerances are a function of the selected gap length (typically 1 mm) but are non-critical, say $^{+}/_{-}50$ μm. This is another important cost reduction factor.

7.2.5 Mechanical Vibration

As stated above, when a discrete notch filter (chapter 6) is incorporated into the feedback loop all vibrations arising from rotor imbalance are eliminated making this type of bearing very useful for applications which are sensitive to vibrations.

7.2.6 Stiffness

The stiffness of any bearing is a function of the frequency of the applied load (the term *stiffness* is defined in section 6.5). Magnetic bearings have the advantage that this stiffness characteristic may be tailored to almost any requirement via the feedback loop. For example, infinite stiffness for static loads may be combined with zero stiffness for rotational frequency loads as demonstrated in this investigation. This combination of properties is particularly attractive for high precision machine tools [34].

7.2.7 Power Consumption

For the *radial* bearing (bearing no. 1), capable of supporting a maximum load of 3,5 kg, the no-load power consumption was Ø,2 Watts at a rotational speed of 25ØØØ r/min. *Radial* bearings develop drag torques when loaded due to the unsymmetric magnetic field which is set up, causing cyclic magnetisation of the rotor. This was confirmed by the perceptable drop in speed of the above bearing when switching out the notch filter. The power required for driving the rotor was measured and found to be 5Ø Watts without the notch filter and only 25 Watts with the notch filter. The additional 25 watts is ascribed to the "electromagnetic drag" on the rotor, whereas the 25 Watts required for driving the rotor, after removal of the "drag", by means of the notch filter, would be mainly windage loss since the rotor was not run in a vacuum. The total motor losses were measured by decoupling the bearing rotor and then measuring the electrical power input at the

same speed. Additional copper losses were accounted for by measuring the loaded and no-load input current and the dc resistance of the armature. These motor losses were then subtracted from the total input power to obtain the above two loss figures.

From the above it is thus concluded that the main loads should preferably be carried by the axial bearing which does not develop drag torques so that the power consumption may be kept very low in spite of loading.

The power consumption of an *axial* magnetic bearing, which was designed by the author to support a 200 kg rotor, was estimated at 10 Watts, independent of speed. This figure could not be confirmed experimentally at the time of this writing since this bearing was not yet operational. Such a power consumption would, however, provide a rundown time of 3 weeks if the energy to drive the bearing is extracted from the flywheel which has an energy storage capacity of 18 Mega-Joules.

The experimental figures measured with the radial bearing above nevertheless indicates its superiority to that of any mechanical bearing when comparing, for instance, the rundown time constant of 3 hours which was measured for high speed mechanical bearings by the author (chapter 1).

7.2.8 Expected Life and Wear

Mechanical wear is totally absent in magnetic bearings. Material fatigue due to stresses induced by rotation would thus be the limiting factor on the life expectancy of the bearing.

7.2.9 System Reliability and Power Failures

The mean time to failure of such a system will be determined mainly by the statistical failure rate of the electronic servo loop which, when properly designed, could easily exceed that of mechanical bearings by far. Figures

of 50000 hours are realistic.

Power failures are a different matter and special precautions have to be taken. For most applications the use of back-up storage batteries is an obvious solution. In the experimental work done here two series coupled 12V, 10Ah lead acid motorbike batteries, which were trickle charged at a current of 1A from a dual laboratory power supply, served ideally as the +12V and -12V supply with automatic mains failure backup. During the course of the experimental work several power failures, without any detrimental effect on the bearing, were experienced with the bearing running at high speed, proving the worth of this arrangement. For energy storage flywheels the energy stored in the flywheel itself would provide the back-up supply. In the event of an internal system failure so-called mechanical touch down bearings [1] will prevent the rotor from selfdestruction as these latter bearings will be dimensioned to allow for at least one rotor run-down from maximum speed.

7.2.10 Lubricants and Ultra-clean Environments

The total absence of lubricants make the magnetic bearing particularly suitable for environments that should be free of traces of hydrocarbons such as high and ultra-high vacuum chambers [33].

7.2.11 Cost

The cost effectivity of a magnetic bearing increases with the size of the bearing and with its operating speed. A major portion of the costs of the electronic system remains constant when the size of the bearing changes, the only components changing being the power supply and the output stage of the power amplifier. The cost of the electronic system thus becomes smaller relative to the total system costs as the size of the bearing increases. The component cost of the total electronic system for the 3-dimensional bearing (bearing no. 2) of this project was approximately R200-00.

The improved cost effectivity which is realised at higher speeds is relative to that of mechanical bearings because of the higher degree of sophistication required by mechanical bearings at these speeds.

The costs of the mechanical components of a magnetic bearing should be relatively low, especially when mass produced, due to the less stringent tolerance and balancing requirements as explained above.

It is thus clear that magnetic bearings should be considered for applications such as flywheel energy stores, gyroscopes, high precision machine tools, centrifuges, turbomolecular pumps and many others.

7.3 Proposed Follow-up Work

Although there are many topics which could be identified for usefull follow-up work, only three will be discussed here:

7.3.1 Sensorless Feedback

The current-voltage relationships of the driving coils may be used to compute the component of this current which represents the rotor displacement. This "displacement " current may then be used to control the coil voltage via a proven compensator, thus eliminating the need for a position transducer. Alternately, the input impedance of the driving coil, which is found to be unstable, may be shunted by a suitable "stabilising impedance" and a far simpler and thus more reliable system would result. A more accurate model of the system, than that used in the abortive attempt described in section 5.5, would have to be found, however, before attempting to put this idea to practice. It may prove to be necessary to take the skin effect of the unlaminated magnetic core into consideration. As a first step, the effect of eddy currents could be eliminated by constructing an experimental bearing with ferrite cores. This system could serve to test the basic principle of sensorless feedback. Once an accurate model is found, it should be tested for observability and controlability before proceding any further. In retrospect, it may be said that the procedure whereby this concept was tested during this investigation was probably too ambitious and a more cautious, step by step approach should have been adopted.

7.3.2 Transfer Function of the Rotating Body

In an attempt to predict the behaviour of the 3-dimensional magnetic bearing at high angular velocities of the rotor a transfer function matrix for this rotating body was derived. These transfer functions were identical to that derived by Craig [29] for the dynamically tuned gyroscope. The off-diagonal elements of the matrix indicated the cross-coupling which exists between the various axes due to

gyroscopic effects. The dynamic behaviour of the system, due to these predicted cross coupling effects, did not agree with experimental results. For instance, an undamped precession of the rotor, which should have manifested itself as a resonance peak, was predicted, but could not be observed in practice with the experimental bearing. It is expected that the geometry of the rotor, which was a long cilindrical shape with its mass concentrated mainly at the two ends, did not lend itself well to demonstrating these effects because the polar moment of inertia about its rotational axis was too low. Thus the gyroscopic effects, if present, were probably masked by noise. In order to investigate this multivariable feedback control problem, a new rotor, resembling the geometry of a practical flywheel system more closely, would have to be constructed.

7.3.3 Magnetic Suspension of a Flexible Hoop

The magnetically restrained kinetic energy system referred to in section 1.2 is essentially a flexible hoop which has to be suspended magnetically. Due to its flexibility, a multiplicity of suspension magnets, with feedback loops, spaced at regular intervals around its periphery, will be required to suspend it successfully.

Since a considerable degree of cross coupling is to be expected, particularly between adjacently placed control loops, such a system poses a multivariable control problem of considerable magnitude. In investigating this problem it will probably be neccessary to view the hoop as a closed transmission or delay line with a fixed propagation delay around its circumference. This system will be prone to the development of standing waves which will have to be filtered out by the regularly spaced suspension points.

APPENDIX 3A

ESTIMATION OF EFFECTIVE IRON SHUNT RESISTANCE r_1

From fig. 3.5 the following relationship can be derived in the frequency domain:

$$E_1=(j\omega r_1 I_2)/(j\omega+r_1/L_1) \quad \text{.....(3A.1)}$$

A Bode amplitude plot of E_1 with I_2 held constant would, at low frequencies, where $\omega<r_1/L_1$, display a positive slope of 20 dB/decade. With $\omega>r_1/L_1$ the curve will flatten out to 0 dB/decade. The crossover point where

$$\omega=\omega_o=r_1/L_1 \quad \text{.....(3A.2)}$$

is determined from an experimental Bode plot.

An experimental curve for a 600 Newton radial bearing is shown in fig. 3A.1. In this case $\omega_o=2\pi\times150=942$ rad/s. In order to determine this curve the rotor was clamped at x=0 and E_1 was measured by means of a search coil placed in the slot of one of the stator poles adjacent to the air gap.

L_1 was measured to be 30 mH.
Thus $r_1=942\times30\times10^{-3}=27,72\ \Omega$.

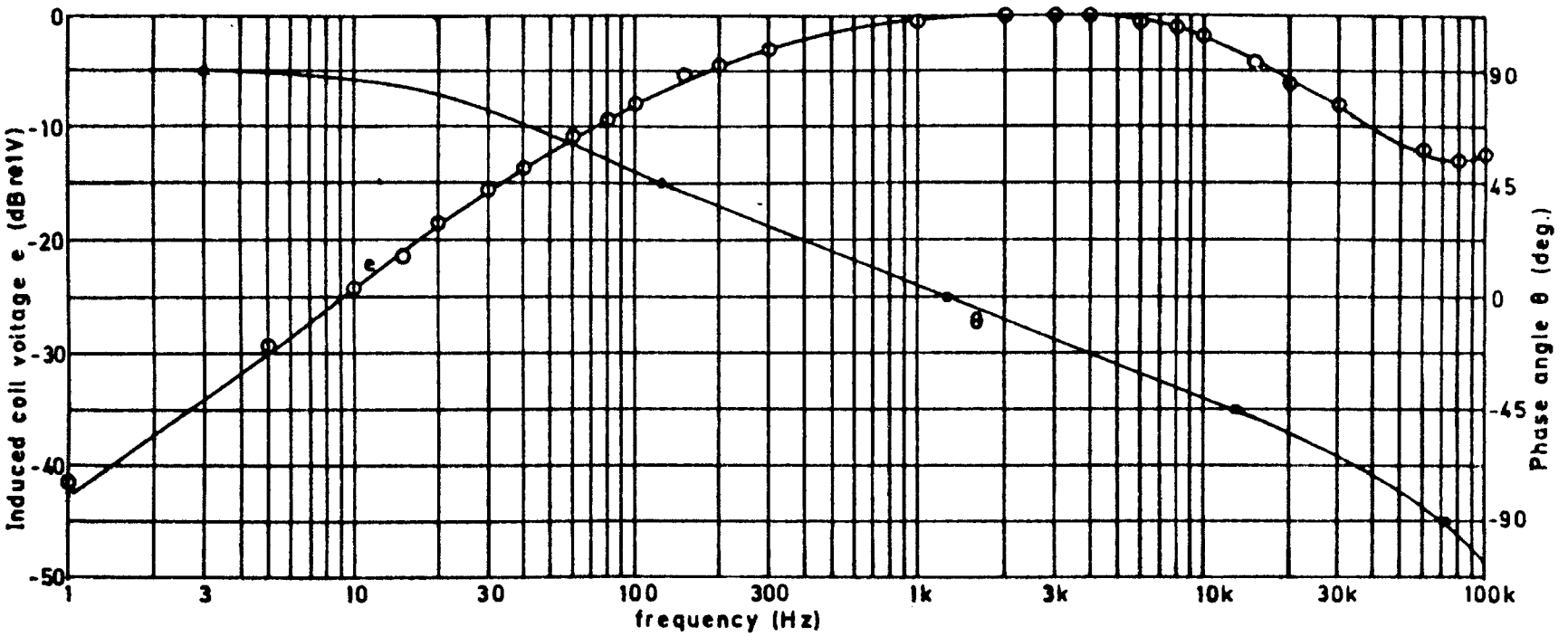

FIG. 3A.1 EXPERIMENTAL BODE PLOT of COIL VOLTAGE at CONSTANT CURRENT

APPENDIX 3B

LINEAR STATE EQUATIONS FOR THE CURRENT FED MAGNETIC BEARING

Assume that the total magnetic bearing (ie rotor as well as stator) is being accelerated at a rate of a m/s^2. The velocity of the rotor relative to the stator is v m/s.

Thus the total acceleration of the rotor a_t=a+dv/dt
The magnetic force acting on the rotor

$$f=M(a+dv/dt) \quad \text{.....(3B.1)}$$

from eq. (3.12) this becomes

$$\dot{v}=\frac{L_o d}{2M}\left[\left(\frac{I_o+i_5}{d-x}\right)^2-\left(\frac{I_o+i_3}{d-x}\right)^2\right]-a \quad \text{.....(3B.2)}$$

Assuming both current amplifiers to be operating in their linear range the following relationships from eq. (3.2) hold:

$$i_2(t)=i_4(t)=i_1(t) \quad \text{.....(3B.3)}$$

Replacing $i_2(t)$ and $i_4(t)$ according to eq. (3B.3) and e_1 according to eq.(3.7) into eq. (3.3) yields.

$$\left.\begin{aligned}\dot{i}_3&=\frac{I_o+i_3}{d+x}v-\frac{r_1(d+x)}{dL_o}i_3+\frac{r_1(d+x)}{dL_o}i_1 \quad \text{and}\\ \dot{i}_5&=-\left(\frac{I_o+i_5}{d-x}\right)v-\frac{r_1(d-x)}{dL_o}i_5-\frac{r_1(d-x)}{dL_o}i_1\end{aligned}\right| \quad \text{.....(3B.4)}$$

The relationship $\dot{x}=v$ together with equations (3B.2) and (3B.4) constitute the required set of state equations:

$$\dot{x}=v$$

$$\dot{v}=\frac{L_o d}{2M}\left[\left(\frac{I_o+i_5}{d-x}\right)^2-\left(\frac{I_o+i_3}{d+x}\right)^2\right]-a$$

$$\dot{i}_3=\left(\frac{I_o+i_3}{d+x}\right)v-\frac{r_1(d+x)}{dL_o}i_3+\frac{r_1(d+x)}{dL_o}i_1$$

$$\dot{i}_5=-\left(\frac{I_o+i_5}{d-x}\right)v-\frac{r_1(d-x)}{dL_o}i_5-\frac{r_1(d-x)}{dL_o}i_1 \qquad \text{.....(3.15)}$$

The Jacobian matrices are defined as (see refs. [38]&[39]):

$$\mathbf{A}\triangleq\begin{bmatrix} \frac{\delta\dot{x}}{\delta x} & \frac{\delta\dot{x}}{\delta v} & \frac{\delta\dot{x}}{\delta i_3} & \frac{\delta\dot{x}}{\delta i_5} \\ \frac{\delta\dot{v}}{\delta x} & \frac{\delta\dot{v}}{\delta v} & \frac{\delta\dot{v}}{\delta i_3} & \frac{\delta\dot{v}}{\delta i_5} \\ \frac{\delta\dot{i}_3}{\delta x} & \frac{\delta\dot{i}_3}{\delta v} & \frac{\delta\dot{i}_3}{\delta i_3} & \frac{\delta\dot{i}_3}{\delta i_5} \\ \frac{\delta\dot{i}_5}{\delta x} & \frac{\delta\dot{i}_5}{\delta v} & \frac{\delta\dot{i}_5}{\delta i_3} & \frac{\delta\dot{i}_5}{\delta i_5} \end{bmatrix} \quad \& \quad \mathbf{B}\triangleq\begin{bmatrix} \frac{\delta\dot{x}}{\delta a} & \frac{\delta\dot{x}}{\delta i_1} \\ \frac{\delta\dot{v}}{\delta a} & \frac{\delta\dot{v}}{\delta i_1} \\ \frac{\delta\dot{i}_3}{\delta a} & \frac{\delta\dot{i}_3}{\delta i_1} \\ \frac{\delta\dot{i}_5}{\delta a} & \frac{\delta\dot{i}_5}{\delta i_1} \end{bmatrix} \qquad \text{.....(3B.5)}$$

estimated at the nominal point where vector $\mathbf{X}_r=\emptyset$. Equation (3.16) is now obtained from equations (3B.5) and (3.15).

APPENDIX 4A

DERIVATION OF DESCRIBING FUNCTIONS FOR MAGNETIC BEARINGS

4A.1 For the Non-saturating Core

The force on the rotor due to coil 1 is (from eq. 3.1Ø)

$$f_1=\Phi_1^2(t)/(\mu_o A) \qquad (4A.1)$$

(f_1 is chosen to be in the negative x-direction).

$\Phi_1(t)$ is given by equations (4.6),(4.7) and (4.9).

The Fourier coefficients A_1 and B_1 of the fundamental component are

$$A_1=\frac{\omega}{2\pi}\int_{\emptyset}^{\frac{2\pi}{\omega}} f_1\cos\omega t\ dt \quad \text{and} \quad B_1=\frac{\omega}{2\pi}\int_{\emptyset}^{\frac{2\pi}{\omega}} f_1\sin\omega t\ dt \qquad (4A.2)$$

Thus

$$A_1=\frac{\omega}{2\pi\mu_o A}\left[\int_{\emptyset}^{\frac{\pi}{\omega}}\left\{\frac{\dot{E}}{n\omega}(1-\cos\omega t)+\Phi_o\right\}^2\cos\omega t\ dt+\right.$$

$$\int_{\frac{\pi}{\omega}}^{\frac{(\pi+\gamma)}{\omega}}\left\{\frac{2\dot{E}}{n\omega}+\Phi_o-\frac{V}{n}\left(t-\frac{\pi}{\omega}\right)\right\}^2\cos\omega t\ dt+$$

$$\left.\int_{\frac{(\pi+\gamma)}{\omega}}^{2\pi}\{\Phi_o\}^2\cos\omega t\ dt\right]\triangleq\frac{\omega}{2\pi\mu_o A}[I_1+I_2+I_3] \qquad (4A.3)$$

and

$$B_1=\frac{\omega}{2\pi\mu_o A}\left[\int_{\emptyset}^{\frac{\pi}{\omega}}\left\{\frac{\dot{E}}{n\omega}(1-\cos\omega t)+\Phi_o\right\}^2\sin\omega t\ dt+\right.$$

$$\left.\int_{\frac{\pi}{\omega}}^{\frac{\pi+\gamma}{\omega}}\left\{\frac{2\dot{E}}{n\omega}+\Phi_o-\frac{V}{n}\left(t-\frac{\pi}{\omega}\right)\right\}^2\sin\omega t\ dt+\int_{\frac{\pi+\gamma}{\omega}}^{2\pi}\{\Phi_o\}^2\sin\omega t\ dt\right]$$

$$\triangleq \frac{\omega}{2\pi\mu_o A}\,[J_1+J_2+J_3] \qquad \text{(4A.4)}$$

where I_1, I_2, I_3, J_1, J_2 and J_3 equal the various integrals in their order of appearance above and $\gamma \triangleq \frac{2\mathcal{E}}{V}$. These integrals will, for the sake of convenience, be estimated separately: By defining $e=\frac{\mathcal{E}}{n\omega}$ and $v=\frac{V}{n\omega}$ we obtain

$$I_1 = \int_{\emptyset}^{\frac{\pi}{\omega}} \{e(1-\cos\omega t)+\Phi_o\}^2 \cos\omega t\,dt = -(e^2+e\Phi_o)\frac{\pi}{\omega} \qquad \text{(4A.5)}$$

$$I_2 = \int_{\frac{\pi}{\omega}}^{\frac{(\pi+\gamma)}{\omega}} \{2e+\Phi_o - \frac{V}{n}(t-\frac{\pi}{\omega})\}^2 \cos\omega t\,dt$$

$$= \frac{1}{\omega}[-\{\Phi_o^2-2v^2\}\sin\gamma+2v\Phi_o\cos\gamma-2v(2e+\Phi_o)] \qquad \text{(4A.6)}$$

$$I_3 = \int_{\frac{(\omega+\gamma)}{\omega}}^{2\pi} \Phi_o^2\cos\omega t\,dt = \frac{\Phi_o^2}{\omega}\sin\omega t\Big|_{\frac{(\pi+\gamma)}{\omega}}^{2\pi} = \frac{\Phi_o^2}{\omega}\sin\gamma \qquad \text{(4A.7)}$$

Thus from eq. (4A.3)

$$A_1 = \frac{-e}{2\pi\mu_o A}[(e+\Phi_o)\pi+4v(1-\frac{\sin\gamma}{\gamma})+4\Phi_o(\frac{1-\cos\gamma}{\gamma})] \qquad \text{(4A.8)}$$

$$J_1 = \int_{\emptyset}^{\frac{\pi}{\omega}} \{e^2-2e^2\cos\omega t+\frac{e^2}{2}+\frac{e^2\cos 2\omega t}{2}+2e\Phi_o-2e\Phi_o\cos\omega t+\Phi_o^2\} \times \sin\omega t\,dt$$

$$= \frac{2}{\omega}\{\frac{11}{6}e^2+2e\Phi_o+\Phi_o^2\} \qquad \text{(4A.9)}$$

$$J_2 = \int_{\frac{\pi}{\omega}}^{\frac{(\pi+\gamma)}{\omega}} \{2e+\Phi_o+\pi v-v\omega t\}^2 \sin\omega t\,dt$$

$$= -\frac{1}{\omega}\left(4e(e+\Phi_o)+(\Phi_o^2-2v^2)(1-\cos\gamma)-2v\Phi_o\sin\gamma\right] \quad \ldots\ldots\ldots\ldots (4A.10)$$

$$J_3 = \int_{\frac{(\pi+\gamma)}{\omega}}^{2\pi} (\Phi_o)^2 \sin\omega t \, dt = \frac{\Phi_o^2}{\omega}\cos\omega t \Big|_{\frac{(\pi+\gamma)}{\omega}}^{2\pi} = \frac{\Phi_o^2}{\omega}(1+\cos\gamma) \quad \ldots\ldots\ldots\ldots (4A.11)$$

from equations (4A.4), (4A.9) and (4A.10)

$$B_1 = \frac{e}{2\pi\mu_o A}\left[-\frac{e}{3} + 4v\frac{(1-\cos\gamma)}{\gamma} + 4\Phi_o\frac{\sin\gamma}{\gamma}\right] \quad \ldots\ldots\ldots\ldots\ldots\ldots (4A.12)$$

B_1 represents the amplitude of the force wave which is in phase with the control voltage e_c whereas A_1 represents the amplitude of the force component which leads e_c by $\pi/2$ rad.

The total fundamental component of the force

$$C_1 = (A_1^2+B_1^2)^{\frac{1}{2}} \Big| \tan^{-1}\frac{A_1}{B_1} \quad \ldots\ldots\ldots\ldots\ldots\ldots\ldots\ldots\ldots\ldots (4A.13)$$

and the describing function, taking into account the effect of both driving coils

$$N(E,\omega) = \frac{2C_1}{E}\Big| \tan^{-1}\frac{A_1}{B_1} \Big| \quad \ldots\ldots\ldots\ldots\ldots\ldots (4A.14)$$

$$= \frac{2}{E}(B_1+jA_1)$$

4A.2 For the Saturating Core

Cyclic saturation of the core is represented by $\varphi(t)=\Phi_m$ in fig. 4.4.

In order to obtain the Fourier coefficients A_1' and B_1' four different intergrals have to be solved this time. (See previous section):

$$I_1 \triangleq \int_{\emptyset}^{\frac{\beta}{\omega}} \left\{\frac{\hat{E}}{n\omega}(1-\cos\omega t)+\Phi_o\right\}^2 \cos\omega t\, dt$$

$$I_2 \triangleq \int_{\frac{\beta}{\omega}}^{\frac{\pi}{\omega}} \Phi_m^2 \cos\omega t\, dt$$

$$I_3 \triangleq \int_{\frac{\pi}{\omega}}^{\frac{(\pi+\gamma')}{\omega}} \left(\Phi_m - \frac{V}{n}t + \frac{V\pi}{n\omega}\right)^2 \cos\omega t\, dt \qquad \text{.....(4A.15)}$$

$$I_4 \triangleq \int_{\frac{(\pi+\gamma')}{\omega}}^{2\frac{\pi}{\omega}} \Phi_o^2 \cos\omega t\, dt$$

where $\gamma'=\dfrac{\Phi_m - \Phi_o}{V}$

The angle β, where $\varphi(t)=\Phi_m$, is obtained from eq.(4.7). Thus

$$\frac{\hat{E}}{n\omega}(1-\cos\beta) + \Phi_o = \Phi_m \text{ , thus}$$

$$\beta=\cos^{-1}\left\{1-\frac{n\omega}{\hat{E}}(\Phi_m - \Phi_o)\right\} \qquad \text{.....(4A.16)}$$

$$\frac{2\hat{E}}{n\omega}+\Phi_o > \Phi_m$$

Solving equations (4A.15) we obtain:

$$I_1 = \frac{-1}{\omega}\{(e^2+e\Phi_o)\beta-(\frac{7}{4}e^2+2e\Phi_o+\Phi_o^2)\sin\beta + (\frac{e^2+e\Phi_o}{2})\sin 2\beta - \frac{e^2}{12}\sin 3\beta\}$$

$$I_2 = -\frac{\Phi_m^2}{\omega}\sin\beta$$

$$I_3 = \frac{-1}{\omega}[\{(P'-(\pi+\gamma')v)^2-2v^2\}\sin\gamma' - (2P'v-2\pi v^2-2\gamma' v^2)\cos\gamma'+2Pv-2\pi v^2]$$

where $P' \triangleq \Phi_m + \pi v$

$$I_4 = \frac{\Phi_o^2}{\omega}\sin\gamma$$

where $e=\frac{E}{n\omega}$ and $v=\frac{V}{n\omega}$ as defined previously.

Thus from eq. (4A.2)

$$A_1' = \frac{\omega}{\pi\mu_o A}\{I_1+I_2+I_3+I_4\} \quad \text{.....(4A.18)}$$

$$= \frac{-1}{\pi\mu_o A}[(e^2+e\Phi_o)\beta+2\Phi_m v-(\frac{7}{4}e^2+2e\Phi_o+\Phi_o^2+\Phi_m^2)\sin\beta + (\frac{(e^2-e\Phi_o)}{2})\sin 2\beta - \frac{e^2}{12}\sin 3\beta - 2v^2\sin\gamma' - 2\Phi_o v\cos\gamma'] \quad \text{.....(4A.19)}$$

for B':

$$J_1 \triangleq \int_{\emptyset}^{\frac{\beta}{\omega}} \{e(1-\cos\omega t)+\Phi_o\}^2 \sin\omega t \, dt$$

$$J_2 \triangleq \int_{\frac{\beta}{\omega}}^{\frac{\pi}{\omega}} \Phi_m^2 \sin\omega t \, dt$$

$$J_3 \triangleq \int_{\frac{\pi}{\omega}}^{\frac{(\pi+\gamma')}{\omega}} (\Phi_m - \frac{V}{n}t + v\pi)^2 \sin\omega t \, dt \qquad \text{.....(4A.20)}$$

$$J_4 \triangleq \int_{\frac{(\pi+\gamma')}{\omega}}^{\frac{2\pi}{\omega}} \Phi_o^2 \sin\omega t \, dt$$

from which we obtain:

$$J_1 = \frac{1}{\omega}\{\frac{e^2}{3} + e\Phi_o + \Phi_o^2 - (e+\Phi_o)^2\cos\beta + e(e+\Phi_o)\cos^2\beta - \frac{e^2}{3}\cos^3\beta\},$$

$$J_2 = \frac{\Phi_m^2}{\omega}(1+\cos\beta),$$

$$J_3 = \frac{1}{\omega}\{(\Phi_o^2-2v^2)\cos\gamma' + 2\Phi_o v\sin\gamma' - \Phi_m^2 + 2v^2\}, \qquad \text{.....(4A.21)}$$

after replacing $\gamma' = \frac{\Phi_m - \Phi_o}{v}$, and

$$J_4 = -\frac{\Phi_o^2}{\omega}(1+\cos\gamma').$$

Thus from eq. (4A.4)

$$B'_1 = \frac{1}{\pi\mu_o A}\left[\frac{e^2}{3} + e\Phi_o + 2v^2 + \{\Phi_m^2 - (e+\Phi_o)^2\}\cos\beta + e(e+\Phi_o)\cos^2\beta\right.$$

$$\left. - \frac{e^2}{3}\cos^3\beta - 2v^2\cos\gamma' + 2\Phi_o v\sin\gamma'\right] \qquad \text{.....(4A.22)}$$

APPENDIX 4B

CONTINUOUS TIME NOTCH FILTER

The active notch filter, taken from reference [44] and shown in fig. 4B.1, successfully eliminated the tendency of the rotor of the experimental bearing to resonate. This resonance of the rotor, at a frequency of 925 Hz (5182 r/s), was very pronounced before incorporation of the notch filter.

The transfer function of this filter is

$$\frac{V_2}{V_1} = \frac{G(s^2+\omega_o^2)}{s^2+Bs+\omega_o^2} \qquad \text{(4B.1)}$$

where $B = \frac{2}{R_2C}$, $\omega_o^2 = \frac{1}{R_1R_2C^2}$, $G=1$

and $\frac{1}{R_3} = \frac{1}{R_1} + \frac{1}{R_2}$

From the component values shown

$B = 5036{,}7$ r/s and $\omega_o = 5701$ r/s.

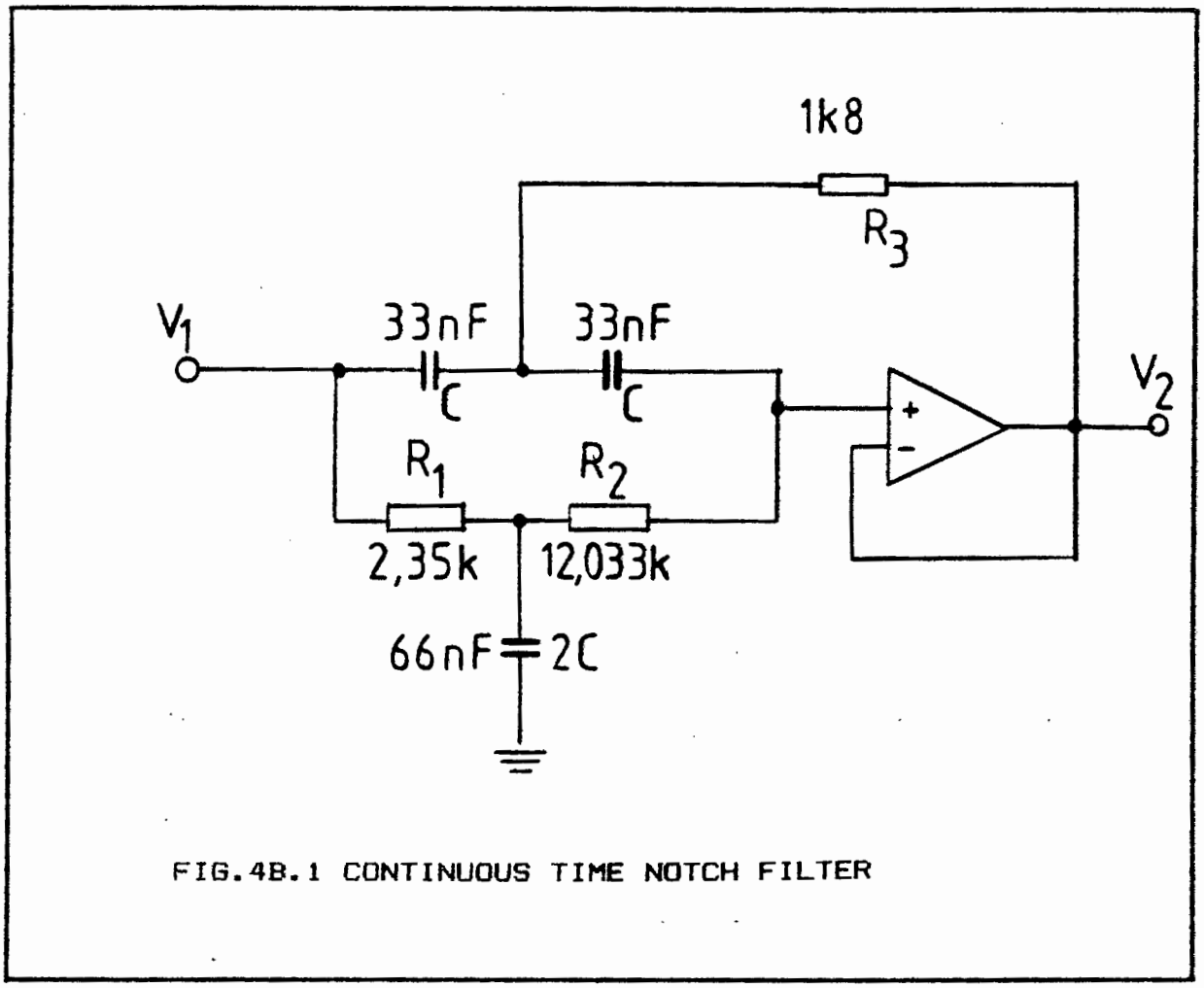

FIG.4B.1 CONTINUOUS TIME NOTCH FILTER

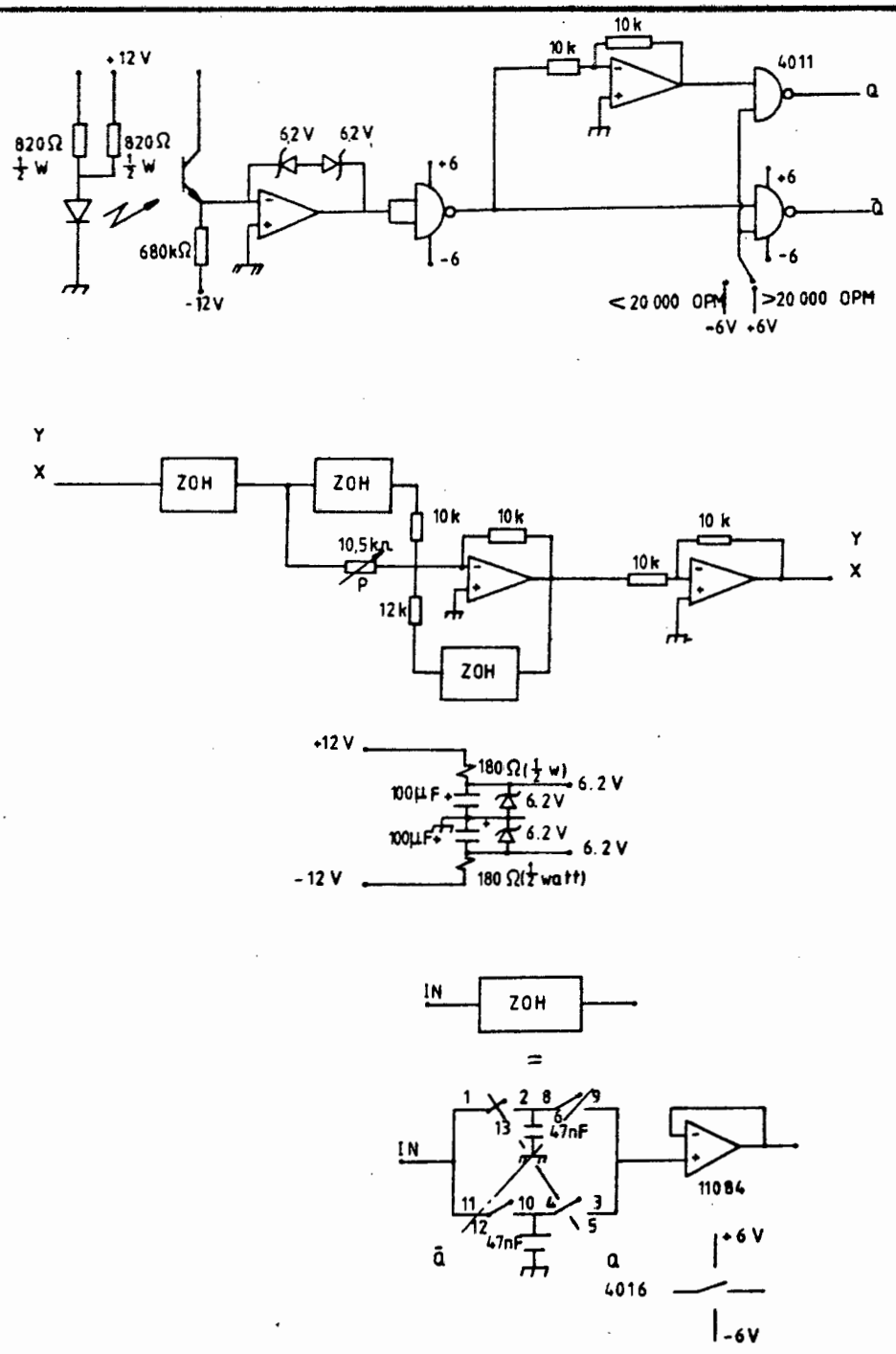

DISCRETE TIME NOTCH FILTER - CIRCIUT DIAGRAM

REFERENCES

[1] Bredenkamp GL, Energiestoring: 'n noodsaaklikheid vir die toekoms, intreerede, Randse Afrikaanse Universiteit, Augustus 1981.

[2] Biggs F, Flywheel Energy Systems, Sandia Laboratories, Albuquerque, New Mexico 87115, Report SAND 74Ø113, Nov. 1973.

[3] Bredenkamp GL, Kineties-Elektriese Energiestoor vir Elektriese Voertuie, SAIEE Elecrtic Transport Symposium, CSIR, Pretoria, 1Ø-11 April 1979.

[4] Besel G, Hau E, Flywheel Energy Accumulators for City Buses - Steel and Composite Design -, 198Ø Flywheel Technology Symposium, Scottsdale, Arizona, USA, Oct. 198Ø.

[5] Rinehart RE, A Flywheel Energy Storage Propulsion System for Intra Urban Buses, 198Ø Flyweel Technology Symposium, Scottsdale, Arizona, Oct. 198Ø.

[6] Lawson LJ, Flywheel Trolley Coach Propulsion with a High-Capacity Composite Flywheel, 198Ø Flywheel Technology Symposium, Scottsdale, Arizona, Oct. 198Ø.

[7] Decker HD, The UMTA Flywheel Trolley Coach Program - An overview, 198Ø Flywheel Technology Symposium, Scottsdale, Arizona, Oct. 198Ø.

[8] Johnson DE, German JJ, Maximum Energy Densities for Composite Flywheels, 198Ø Flywheel Technology Symposium, Scottsdale, Arizona, Oct. 198Ø.

[9] Human GP, Die Optimisering van die Rotorprofiel van 'n Stroomgevoerde Reluktansiemasjien met Elektroniese Kommutasie, M.Sc. thesis, Rand Afrikaans University, December 1983.

[1Ø] Frank AA, Flywheel Continuously Variable Transmission System for Automotive and Transit Propulsion, 1977 Flywheel

Technology Symposium, San Francisco, California, October 5-6, 1977.

[11] Towgood DA, Satchwell DL, An Advanced Vehicular Flywheel System for the Erda Electric-Powered Passenger Vehicle, 1977 Flywheel Technology Symposium, San Francisco, California, Oct. 5-6, 1977.

[12] Cornell EP, Turnbull FG, Barlow TM, Evaluation of a Hybrid Flywheel/Battery Propulsion System for Electric Vehicles, 1980 Flywheel Technology Symposium, Scottsdale, Arizona, Oct. 1980.

[14] Sabnis Ajit V, Dendy Joe B, Schmitt Frank M, A Magnetically Suspended Large Momentum Wheel, J. Spacecraft and Rockets, Vol. 12 No. 7, pp 420-427, July 1975.

[15] Rabenhorst DW, Small TR, Wilkinson WO, Final Report, Low-Cost Flywheel Demonstration Program. Report No. DOE/EC/1-5085. The Johns Hopkins University - Applied Physics Laboratory. April 1980.

[16] Usselmann E, Leybold-Heraeus GmbH & Co. Kg, 5 Köln W. Germany, Private Communication 1977.

[17] Thomson WT, Younger FC, Gordon HS, Whirl Stability of the Pendulously Supported Flywheel System, Paper no.77-APM-20, Journal of Applied Mechanics, Transactions of the ASME.1977

[18] Bredenkamp GL, A Magnetically Restrained Kinetic Energy Storage (MARKES) Ring, Solar '82 Conference, Solar Energy Society of South Africa, Pretoria, Nov. 18-19,1982.

[19] Poubeau PC, Flywheel Energy Storage Systems Operating on Magnetic Bearings, 1980 Flywheel Technology Symposium, Scottsdale, Arizona, Oct., 1980.

[20] Geary PJ, Magnetic and Electric Suspensions, SIRA Research Report R314, 1964.

[21] Laithwaite ER, Electromagnetic Levitation, Proc. IEE, 112, 12, pp2361-75(1965).

Laithwaite ER, High Speed Ground Transport. Royal Institution Discourse 1973 (2 Feb. 1973)

[22] Jayawant BV, Electromagnetic Levitation and Suspension Techniques, Edward Arnold (Publishers) Ltd.,1981.

[23] Nasar SA, Boldea I, Linear Motion Electric Machines, John Wiley & Sons, pp 174-193, 1976.

[24] Jayawant BV, Passenger Carrying Vehicles using Controlled DC and Controlled Permanent Magnets, 2nd IEE Conference on Advances in Magnetic Materials and their Applications, 1-3 September 1976.

[25] Lyman J, Virtually Zero Powered Magnetic Bearing, Report, Cambridge Thermionic Corporation, Cambrigde, Massachusetts, Nov.1974.

[26] Pretorius JHC, Posisiesensor vir 'n Magnetiese Laer, Internal Report 62-EI-79-1, Laboratory for Electrical Energy Technology, Rand Afrikaans University, Johannesburg, 1981.

[27] Gottzein E, Lange B, Magnetic Suspension Control System for the MBB High Speed Train, Automatica, Vol. 11, pp271-284, 1975.

[28] Heading J, Matrix Theory for Physicists, Longmans, Green & Co., 3rd impression, 1963.

[29] Craig RJG, Theory of Operation of an Elastically Supported, Tuned Gyroscope, IEEE Transactions on Aerospace and Electronic Systems, Vol. AES no.3, May 1972.

[30] Earnshaw S, On the Nature of Molecular Forces, Transactions of the Cambridge Philosophical Society, Vol. 7, 1842, pp 97-112.

[31] Wang JC, Marx SH, The Development of a Repulsive Magnetic Bearing, ASME, December, 1976.

[32] Poubeau PC, High Speed Flywheel Operating on "One Active Axis" Magnetic Bearings, 1977 Flywheel Technology Symposium,San Francisco, October 1977.

[33] Frank R, Usselmann E, Magnetgelagerte Turbomolekularpumpe des Typs Turbovac, Vakuum-Technik, 25 Jahrgang. Heft 5 1976.

[34] Katterloher R, Magnetlager, Der Elektriker 5/75 pp 115-116, 1975.

[35] Kaplan BZ, Analysis of a Method for Magnetic Levitation, PROC. IEE, Vol. 114, No. 11, Nov. 1967.

[36] Kaplan BZ, Regev D, Dynamic Stabilization of Tuned-Circuit Levitators, IEEE Transactions on Magnetics, Vol.Mag.-12, no.5, Sept.1976.

[37] Jayawant BV, Rae DP, New Electromagnetic Suspension and its Stabilisation, Proc. IEE, Vol.115, no.4, April 1968.

[38] Kuo BC, Automatic Control Systems, 3rd edition, Prentice-Hall Inc., 1975.

[39] Shinners SM, Modern Control System Theory and Applications, 2nd edition, Addison-Wesley Publishing Co., 1978.

[40] Pretorius JHC, Beheerstelsel vir 'n Radiale Magnetiese Laer, Transactions of the SAIEE, Vol.73, no. 5, 1982.

[41] Bredenkamp GL, Reduction of Energy Losses in Magnetic Bearings due to Imbalance Signals, Transactions of the SAIEE, Vol.73, no.2, Feb., 1982.

[42] Jayawant BV, Sinha PK, Wheeler AR, Whorlow RJ,

Willshire J, The Development of a 1 Ton Magnetically Suspended Vehicle Using Controlled DC Magnets, Proc. IEE, Vol.123, no.9, September, 1976.

[43] Pretorius JHC, 'n Drie Dimensionele Magnetiese Laer vir Rotors met Hoë Rotasiesnelhede, M.Sc. thesis, Rand Afrikaans University, December 1982.

[44] Johnson DE, Hilburn JL, Rapid Practical Designs of Active Filters, John Wiley & Sons, 1975.

[45] Frazier RH, Gilinson Jr. PJ, Oberbeck GA, Magnetic and Electric Suspensions, MIT Press, 1974.

[46] Bohn GH, The Influence of Eddy Currents on an Electromagnetic Levitation System, 2nd IEE Conference on Advances in Magnetic Materials and their Applications, London, 1-3 September, 1976.

LIST OF SYMBOLS USED

Where both the upper and lower case of a symbol are given together, the lower case will denote the time dependent function whilst the upper case will denote one of the following 1) the Laplace transform of the variable, 2) the quiescent value thereof or 3) the amplitude when the variable is a sinusoidal function

A : effective magnetic pole area (m^2)
A,a : linear acceleration (m/s^2)
A_V : Voltage amplification factor
A_1 : Fourier coefficient of force wave
a : complex constant
B : magnetic flux density (T)
B_1 : Fourier coefficient of force wave
C_1 : Fourier coefficient of force wave
C_X : capacitance (F)
D : mechanical damping coefficient (N.s/m)
d : neutral gap length (m)
d_X : elements of $\mathbb{D}$
E,e : induced voltage (V)
$\hat{E}$: amplitude of applied sinusoidal coil voltage (V)
e : normalised applied coil voltage (Volt.sec/turn.rad)
f,F : force (N)
i,I : current (A)
G( ): transfer function
H : magnetic field strength (A/m)
H( ): feedback or compensator transfer function
H(z): discrete time system transfer function
K : spring constant (N/m)
K_C : constant
k : integer (1,2,3...)
k_X : feedback coefficient
L : inductance (H)
L( ): loop gain
M : mass (kg)
m_X : mechanical transfer function singularity (rad/s)
N( ): describing function (N/V)
n : turns
P,p : time integral of induced voltage (V.s)
P_C(): characteristic polynomial

p_x,p_{xx}: transfer function pole (rad/s)
R : small signal gain (N/V)
R_c : constant (Ω)
R_x : resistance (Ω)
r : internal resistance (Ω)
s : complex frequency or Laplace variable (rad/s)
t : time (s)
u : input reference signal
V,v : linear velocity (m/s)
V : supply voltage (V)
v : normalised supply voltage (Volt.sec/turn.rad.)
W : stored energy or work (J)
X,x : linear displacement (m)
X(k): discrete time, independent variable
x^+,x^-: refers to positive and negative X-axis respectively
Y(k): discrete time, dependent variable
Z( ): compensation impedance (Ω)
z_x,z_{xx}: transfer function zero (rad/s)

$\mathbb{A}$: state transition matrix
$\mathbb{B}$: input matrix
$\mathbb{C}$: output matrix
$\mathbb{D}$: difference feedback matrix
$\mathbb{H}_o$(): feedback transfer function matrix
$\mathbb{K}$: feedback matrix
$\mathbb{R}$: input vector
$\mathbb{Y}$: ouput vector
$\mathbb{X}$: state vector

β : phase angle for unsaturated core (radians)
ψ : phase shift (radians)
Φ,φ : magnetic flux (W)
γ : freewheeling angle (rad)
λ : complex frequency constant (rad/s)
μ : magnetic permeability (H/m)
π : 3,141593
ρ : material density (kg/m^3)
σ : mechanical stress (N/m^2)
τ : auxilliary time variable (s)
θ : phase angle (radians)
ω : angular frequency (rad./s)

≙ : means "defined as"

Notes: